AN ULTRA-SENSITIVE INSTRUMENT FOR COLLISION ACTIVATED DISSOCIATION MASS SPECTROMETRY WITH HIGH MASS RESOLUTION.

G.J. LOUTER

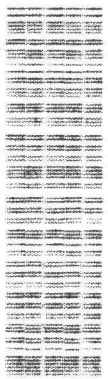

AN ULTRA-SENSITIVE INSTRUMENT FOR COLLISION ACTIVATED DISSOCIATION MASS SPECTROMETRY WITH HIGH MASS RESOLUTION.

Proefschrift

ter verkrijging van de graad van doctor in de technische wetenschappen aan de Technische Hogeschool Delft, op gezag van de Rector Magnificus Prof.Ir. B.Th.P. Veltman, voor een commissie, aangewezen door het kollege van dekanen, te verdedigen op dinsdag 23 februari 1982 te 14.00 uur

door

GERARDUS JOZEF LOUTER.

Natuurkundig Ingenieur
geboren te Alkmaar

Dit proefschrift is goedgekeurd door de promotor:

Prof.Dr. J. Kistemaker

VOORWOORD

Toen ik eind 1976 kwam solliciteren op de baan op het FOM-Instituut voor AMOLF, met als omschrijving "de bouw van een dubbeltrapsmassaspektrometer met variabele dispersie en simultane detektie", had ik er geen idee van wat dat voor instrument zou moeten zijn, of hoeveel tijd en moeite het zou kosten om het te bouwen. Nu, na zo'n 5 jaar, ben ik daar wel achter gekomen. Van het apparaat, "onze dubbeltraps", ken ik zo'n beetje elk knopje en schroefje. De bouw heeft heel wat tegenslagen gehad en heeft ongeveer 4 jaar in beslag genomen. Het heeft geleid tot een instrument dat uniek is in de wereld vanwege zijn gevoeligheid en resolutie. In die 4 jaar zijn er vele handen nodig geweest om al dat werk te klaren. Deze vele handen hebben niet alleen licht werk gemaakt: ze hebben er ook préttig werk van gemaakt. Ik zal altijd goede herinneringen bewaren aan al die mensen waarmee ik heb mogen samenwerken.

In de eerste paar maanden op het FOM-Instituut is dat Hans Tuithof geweest, die in een spoedkursus dubbeltrapsmassaspektrometrie de basis heeft gelegd voor mijn kennis op dit gebied. Samen met Henk Boerboom is hij verantwoordelijk voor het ontwerp van de dubbeltraps. Henk heeft me ingewijd in de geheimen van de ionenoptika. Met hem ook heb ik menig probleem doorgepraat en vaak ook opgelost. Henk, bedankt dat je altijd tijd voor me had. Bedankt ook voor de vele hulp bij het schrijven van dit proefschrift.

Henk van de Brink is iemand die met z'n handen maken kan wat z'n ogen zien. Zijn ervaring, kennis en geduld zijn onmisbaar geweest om de dubbeltraps draaiend te krijgen. Bovendien wist hij, met z'n zonnige karakter om ook mij, ook na moeilijke nachten, draaiend te krijgen. Henk, je bent altijd m'n steun en toeverlaat geweest, bedankt voor alles.

In de elektronika werkplaats zijn heel wat mensen bezig geweest voor de dubbeltraps. Ik denk in de eerste plaats aan Henk Dekker en Jan Terbeek, die verantwoordelijk zijn voor de grote verscheidenheid aan elektronika in het apparaat. Van hun heb ik heel wat opgestoken op het gebied van hoogspanningstechnieken. Jan maakte de dubbeltraps tot één van de best en

mooist gedokumenteerde instrumenten van dit lab. Alleen de funktie van die blauwe Wybert had iets nader omschreven kunnen worden. Met Han Platvoet en Anton Buyserd heb ik ook nauw en prettig samengewerkt. Han ontwikkelde een sturings-/stabilisatiesysteem voor de eerste magneet. Anton heeft geholpen bij het detektiesysteem en de ontwikkeling van komputerprogramma's. Paul van Deenen is mij als organisator en allesweter op het gebied van elektronika altijd tot grote steun geweest.

De werkplaats was een plaats waar ik graag kwam, niet in het minst omdat er zoveel vriendelijke mensen rondliepen. Er stond daar ook altijd wel iemand klaar om je uit de nood te helpen als iets aan het apparaat kapot ging. Ik ben altijd zeer tevreden geweest met het prima vakwerk wat daar werd geleverd. Bedankt met name Ton Neuteboom, Piet Kea, Willem Brouwer, Joop Ladru, Willem Barsingerhorn en Ruud Hoep. Het vele laswerk is altijd veilig geweest in de vakkundige handen van Cor van der Zweep. Joop van Wel heeft vele ingewikkelde en gewaagde konstrukties met glas en keramiek verwezenlijkt.

Eigenlijk is de dubbeltraps ontworpen in de tekenkamer. Daar worden de wilde ideeën van wetenschappers en ingenieurs omgezet in te realiseren ontwerpen. Evert de Haas, Paul de Jongh, Herman Ficke en Maarten Hoogervorst, bedankt voor al jullie goed funktionerende ontwerpen; ik heb heel wat van jullie geleerd. Hanna Smid, bedankt voor alle tekeningen en figuren die je voor mij hebt verzorgd.

In het vakuümlab heb ik goede herinneringen aan met name Jan Verhoeven, Gerrit Frijlink en Jeroen Piepenbroek, bij het oplossen van soms moeilijke vakuümproblemen. Jongens, nog bedankt voor de kursussen "elementaire vakuümtechniek" en "taartsnijden voor gevorderden". Van de indrukwekkende kursus van Jan Verhoeven "krachttermen voor alledag" pluk ik nog dagelijks de vruchten.

Vele mensen hebben me bij de bouw van het instrument bijgestaan met hun opbouwende kritiek en goede adviezen. Ik denk hierbij op de eerste plaats aan Professor Kistemaker tijdens de vele werkbesprekingen in de afgelopen vijf jaar. Professor Kistemaker ben ik bovendien erg erkentelijk voor zijn kritische aantekeningen bij mijn publikaties en bij dit proefschrift.

Ik vermeld hier ook Henk Meuzelaar, die met zijn ontembare energie en enthousiasme de grote drijfveer achter de dubbeltraps is geweest. Veel hulp heb ik gehad van Piet Kistemaker, die in staat is om komplexe problemen simpel weer te geven, en die, ook onder soms hachelijke omstandigheden, een prima reisgezel is. Johan Haverkamp en Jan Dallinga bedank ik voor de prettige samenwerking en voor hun hulp bij mijn eerste wankele schreven op het pad der chemie.

Frans Monterie is me zeer behulpzaam geweest, niet alleen met al mijn fotowerk, maar ook bij al die precisie-klusjes, waarbij zijn horlogemakersgeduld en -handigheid goed van pas kwamen.

Margreet Nool bedank ik voor de steun bij al mijn thuiswerk, speciaal bij het schrijven van dit proefschrift.

Last but not least noem ik Tine van der Veer, die heel wat typewerk voor mij heeft verzet, en wier vingers zo langzamerhand blauw moeten zijn van al mijn korrektiewerk in de juist zo mooi getypte tekst; en Henk Sodenkamp, die al mijn drukwerk heeft verzorgd.

The investigations described in this thesis have been published or submitted for publication, with some minor modifications.

CHAPTER 1 - G.J. Louter, A.J.H. Boerboom, P.F.M. Stalmeier, H.H. Tuithof and J. Kistemaker; Int.J.Mass Spectrom.Ion.Phys. 33 (1980) 335.

CHAPTER 2 - G.J. Louter, M.M.J. Lens and A.J.H. Boerboom; Int.J.Mass Spectrom.Ion Phys. 39 (1981) 197.

CHAPTER 3 - G.J. Louter and M.M.J. Lens; Int.J.Mass Spectrom. Ion Phys. 40 (1981) 341.

CHAPTER 4 - G.J. Louter and A.N. Buijserd, submitted to Int.J.Mass Spectrom.Ion Phys.

CHAPTER 5 - Extract from:
G.J. Louter, P.F.M. Stalmeier, A.J.H. Boerboom, J. Haverkamp and J. Kistemaker, Z.Naturforsch. 35c (1980) 6.

The work described in this thesis is part of the research program of the Foundation for Fundamental Research on Matter (FOM) with financial support from the Netherlands Organization for the Advancement of Pure Research (ZWO).

C O N T E N T S

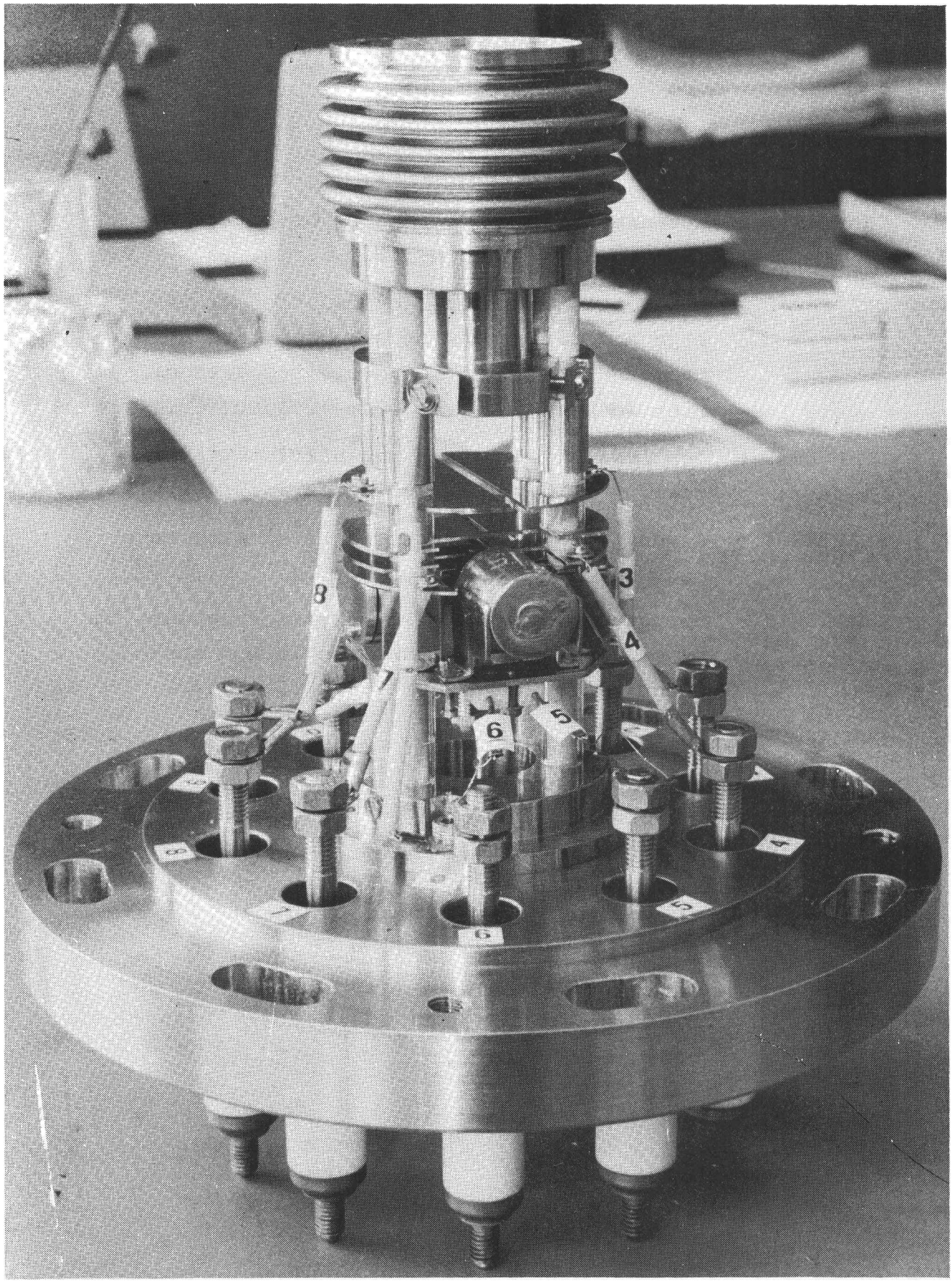

Ion source of the double stage mass spectrometer.

INTRODUCTION

There has been a long period during which fragmentation processes at another place than in the ion source, were considered a nuisance in mass spectrometry (MS). Fragment ions, arising from such processes, generally cause broad mass peaks in a mass spectrum, with apparent masses, that do not correspond to integral mass values [1]. In some instruments even, special electrodes were used to suppress the appearance of these socalled Aston bands [2].

The last decade, however, has shown a growing interest in mass and energy spectroscopy of uni-molecular and collision activated dissociation (CAD) processes outside the ion source. This finds its origin in the valuable information about ion structure and decomposition mechanisms, which are contained in the fragmentation spectra of ions [3]. This information is held in the relative abundance of fragment ions and in the shape and width of the peaks, which reflect the kinetic energy release (KER) at decomposition. In CAD-spectroscopy one can, furthermore, measure the displacement of the fragment peaks, from which follows the excitation energy, transferred at collision.

The spectroscopy of uni-molecular decomposition of metastable ions can be simply performed on conventional double focusing mass spectrometers [4,5]. Its most important properties are a well defined internal energy and lifetime of the precursor ion [3]. Furthermore, isotopic labelling can be used in combination with this method for the elucidation of decomposition mechanisms and the metastable ion structure. CAD spectroscopy, however, has some specific advantages in the ion structure elucidation compared with metastable ion spectroscopy [3]:

1) It enables us to examine also stable ions.
2) It has a much higher yield of fragment ions, favouring the investigation of weaker precursor signals.
3) There is a much larger number of measurable fragment peaks. This generally results in a more specific structure characterization.

4) The CAD spectrum is independent of the internal energy distribution of the precursor; this makes the fragment spectrum more specific. Mixture analysis of isobaric and isomeric ions is possible, by variation of the electron energy in the ion source.
5) From an ion-optical point of view, CAD enables better resolution, because the position of fragmentation can be confined within a small region by using a collision cell [6] or a molecular jet [7], resulting in a better defined object position for the spectrometer.

The most conventional and simple method of fragment spectroscopy can be performed in a double focusing mass spectrometer with a normal geometry of an electrostatic analyser (ESA) followed by a sector magnet (SM). In this case decompositions are observed which occur in the first field-free region between ion source and ESA. An ion kinetic energy (IKE) spectrum is obtained by scanning the ESA voltage and using a detector at the β slit, situated in the energy focal plane of the ESA [8]. Though simple, this method has the disadvantage that there is no mass separation in these spectra between precursor ions. Therefore, overlapping of fragment peaks may occur, especially near the energy of the main ion beam. A considerable improvement is the application of instruments with reversed geometry, where the SM preceeds the ESA. In these instruments the observed fragmentation takes place in the second field-free region, between SM and ESA. Ions of any m/z value can be preselected by the magnet. By scanning the electric sector a so-called mass analysed kinetic energy (MIKE) spectrum is obtained, using a detector, situated behind the ESA [5,9]. With the latter geometry a high energy resolution can be obtained. McReynolds [10] mentions an energy resolution of 500, in a specially designed ESA, and in Porter's paper [11] a value of even 1800 is given. However, fundamentally every method for energy characterization of the fragment ions is accompanied by a poor mass resolution in the order of 70. The cause is found in the KER which can be several eV, and which may cause a considerable peak broadening. Obviously,

structure elucidation of heavier ions with CAD can only be obtained by measurement of the CAD mass spectrum in combination with an increased mass resolution. In this case the energy information is lost and the relative abundance of the fragment ion is used for structure elucidation.

During the last 5 years there has been a fast development of techniques and even special instruments for CAD-MS. One of the earliest improvements in mass resolution was obtained by linked scanning of the electric and magnetic sector fields [12]. This method makes mass resolutions possible of several hundreds The linked scan technique can be applied in both conventional double focusing mass spectrometers and instruments with a reversed geometry. Fragmentation processes are observed, which occur in the first field-free region. The main problems of this technique are the bad reproducibility of the relative peak heights and the low sensitivity.

Both a high mass resolution of several hundreds in the fragment spectrum, as well as a very high transmission of fragment ions can be obtained with the recently developed double and triple quadrupole (Q-pole) mass spectrometers [13,14,15,16]. An important difference of these instruments compared with the sector type mass spectrometers is that fragmentation is initiated by low energy ion-molecule reactions, leading to different types of spectra compared with those obtained with high energy collisions [17,18]. Moreover, Q-pole instruments are fundamentally not suitable to perform energy measurements of the fragment ions.

One very recent development in CAD-MS is the tandem high resolution mass spectrometer of the group of McLafferty [7,19]. With a high mass resolution of the first stage of over 10,000, it is also possible to separately investigate isobaric precursor ions. By application of special ion optics, the precursor ions can be accelerated up to 32 keV, enabling them to measure high energy fragmentation spectra, and also considerably increasing the transmission of fragment ions through the collision region [7]. The second stage is used to record MIKE spectra, by scanning the ESA. It will be used to obtain high resolution CAD mass spectra by simultaneously scanning ESA and SM field (expected mass resolution about 5,000 [7]).

All spectrometers described above have in common, that they are scanning type instruments. This has some fundamental disadvantages, especially in CAD spectrometry:

1) Each precursor ion generally gives rise to only one fragment ion, which can contribute to only one fragment peak. A CAD spectrum, especially of precursors with a high m/z value, can consist of many fragment peaks. As a result, CAD spectra are generally much weaker, sometimes orders of magnitude weaker, than conventional spectra.
2) Fluctuation of the precursor ion current badly influences the reproducibility of CAD spectra in scanning instruments.
3) From short lasting phenomena like laser desorption [20], field desorption (FD) [21] and flash pyrolysis [22] no complete CAD spectra can be measured.

These problems could be fundamentally solved in the tandem mass spectrometer for CAD-MS, designed in 1975 by Tuithof and Boerboom [23]. Using the experience with simultaneous detection systems in our group [24], this instrument has been provided with an electro-optical simultaneous detector.
To increase the CAD mass resolution, we have used a method given by Tuithof [25], who suggested post-acceleration of the fragment ions, in order to reduce their relative kinetic energy spread. He showed that this post-acceleration is fundamentally more effective than increasing the energy of the precursor ions, which was suggested by Wachs [6]. An additional very important advantage of post-acceleration is the diminished angular spread of the fragment ions, which may result in a better transmission.

Application of these advanced techniques resulted in an instrument, characterized by a high CAD-mass resolution (up to 500), a high transmission of fragment ions, up to 100% for individual mass peaks, and an extremely high sensitivity. A more detailed description of the instrument and its performance is given in chapter 1.

Rather complex ion-optics were necessary to combine post-acceleration, simultaneous detection with variable dispersion, and CAD-MS. This led to the development of a special computer

simulation of the instrument, in which a first order matrix description is used for each ion-optical element. The method is discussed in chapter 2. Simulation models, as applied by us, can be very useful in the design of an instrument and to understand the functioning of complex ion optics. They may, furthermore, be applied for the automatic adjustment of an instrument. We use our model to calibrate the masses in our fragment spectra, also at changed mass dispersion.
This application is especially interesting in CAD-MS, as it is unnecessary now to use a calibrant fragment spectrum for each precursor mass that is investigated.

The extremely high sensitivity of our tandem mass spectrometer could only be obtained by application of an electro-optical simultaneous detector, which in contrast with the conventional photographic plate, makes single ion detection possible. Very recent measurements [26] showed that only 5 picogram of dioctyldimethylammonium chloride suffices to obtain a FD-CAD spectrum of m/z 270 (measuring time 80 s, mass range 100 - 270). An additional advantage of this detector, compared with photographic plates is, that the spectra are almost instantaneously available for observation (real time observation of the entire spectrum is possible) and for further processing by our central computer system. The detector is described in chapter 4.

During the last two years, the tandem mass spectrometer has been fully operational. It has been used for both bio- as well as organic-chemical applications. Two illustrations of the versatile application possibilities will be given. In collaboration with the National Institute of Public Health (RIV), CAD-MS has been done on complete myco-bacteria [27]. Together with the laboratory for organic chemistry of the University of Amsterdam, the decomposition mechanism of several organic molecules has been investigated [28,29,30]. Both projects were carried out with pyrolysis CAD-MS. Very typical applications of the instrument are the FD-CAD-MS measurements on various organic compounds [26], which were recently done in collaboration with the Institute for Physical Chemistry of the University of Bonn. This kind of experiments require both a fast measuring time and a very high sensitivity.

REFERENCES

[1] R.G. Cooks, J.H. Beynon, R.M. Caprioli and G.R. Lester, Metastable Ions, Elsevier, Amsterdam, 1973.

[2] J.H. Beynon, Mass Spectrometry and its Application to Organic Chemistry, Elsevier, Amsterdam, 1960, p.200.

[3] K. Levsen, Fundamental Aspects of Organic Mass Spectrometry, Progress in mass spectrometry, Vol.4, Verlag Chemie, Weinheim, 1978.

[4] J.L. Holmes and J.K. Terlouw, Org.Mass Spectrom. 15 (1980) 383.

[5] T. Wachs, P.F. Bente, III and F.W. McLafferty, Int.J.Mass Spectrom. Ion Phys., 9 (1972) 333.

[6] T. Wachs, C.C. van de Sande, P.F. Bente, III, P.P. Dymerski and F.W. McLafferty, Int.J.Mass Spectrom.Ion Phys. 23 (1977) 21.

[7] P.J. Todd, Thesis, Cornell University, Ithaca, N.Y., 1980.

[8] J.H. Beynon, R.M. Caprioli, W.E. Baitinger and J.W. Amy, Int.J.Mass Spectrom.Ion Phys., 3 (1969) 313.

[9] J.H. Beynon, R.M. Caprioli and T. Ast, Org.Mass Spectrom. 5 (1971) 229.

[10] J.H. McReynolds and M. Anbar, Int.J.Mass Spectrom.Ion Phys. 24 (1977) 37.

[11] C.J. Porter, R.P. Morgan and J.H. Beynon, Int.J.Mass Spectrom.Ion Phys. 28 (1978) 321.

[12] A.P. Bruins and K.R. Jennings, Int.J.Mass Spectrom.Ion Phys. 26 (1978) 395.

[13] D. Zakett, W.J. Fies and R.G. Cooks, Anal.Chim.Acta 119 (1980) 129.

[14] R.A. Yost and C.G. Enke, Anal.Chem. 51 (1979) 1250.

[15] M.W. Siegel, Anal.Chem. 52 (1980) 1790.

[16] D.F. Hunt, J. Shabanowitz and A.B. Giordani, Anal.Chem. 52 (1980) 386.

[17] S.A. McLuckey, G.L. Glish and R.G. Cooks, Int.J.Mass Spectrom.Ion Phys. 39 (1981) 219.

[18] J.A. Laramée, P.H. Hemberger, R.G. Cooks, J.Am.Chem.Soc. 101 (1979) 6460.

[19] P.J. Todd and F.W. McLafferty, Int.J.Mass Spectrom.Ion Phys. 38 (1981) 371.

[20] M.A. Posthumus, P.G. Kistemaker, H.L.C. Meuzelaar and M.C. ten Noever, Anal.Chem. 50 (1978) 985.

[21] H. R. Schulten, Int.J.Mass Spectrom.Ion Phys. 32 (1979) 97.

[22] H.L.C. Meuzelaar, P.G. Kistemaker, W. Eshuis and H.W.B. Engel, in: H.H. Johnston and S.W.B. Newsom (Eds.), Rapid Methods and Automation in Microbiology, p.225, Learned Information, Oxford, U.K., 1977.

[23] H.H. Tuithof, Thesis, TH-Delft, 1977.

[24] H.H. Tuithof, A.J.H. Boerboom and H.L.C. Meuzelaar, Int.J.Mass Spectrom. Ion Phys. 17 (1975) 299.

[25] H.H. Tuithof, Int.J.Mass Spectrom.Ion Phys. 23 (1977) 147.

[26] R. Weber, K. Levsen, G.J. Louter, to be published.

[27] G.J. Louter, P.F.M. Stalmeier, A.J.H. Boerboom, J. Haverkamp and J. Kistemaker, Z.Naturforschung 35c (1980) 6.

[28] J.W. Dallinga, N.M.M. Nibbering, A.J.H. Boerboom and G.J. Louter, to be published.

[29] J.J. Zwinselman, C.G. van den Heuvel and N.M.M. Nibbering, in A. Quale (Ed.), Advances in Mass Spectrometry, Heyden, London, 1979, 8A, p.808.

[30] J.W. Dallinga, N.M.M. Nibbering and G.J. Louter, Org.Mass Spectrom. 16 (1981) 183.

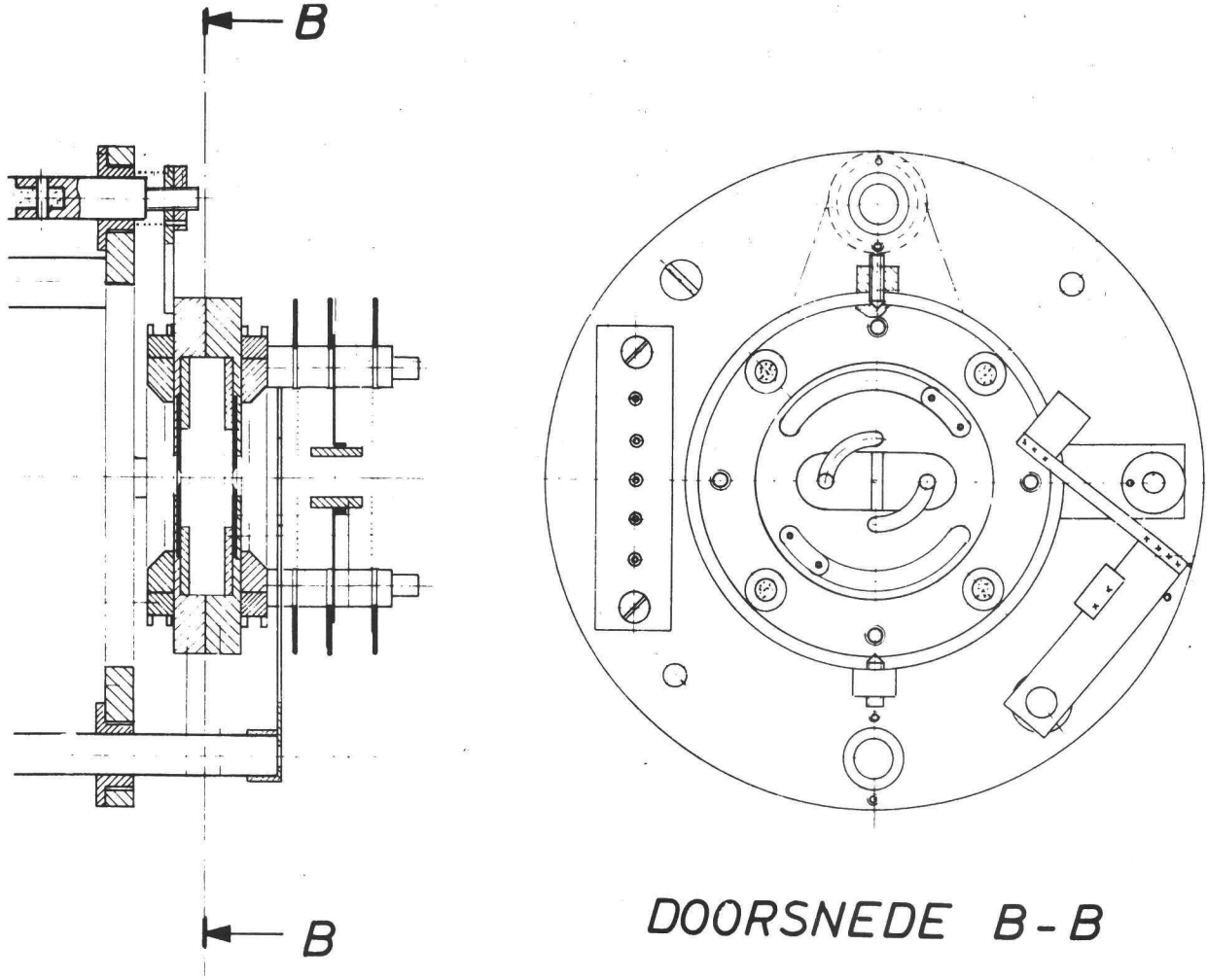

Blue print of the collision cell with adjustable entry and exit slit.

[23] H.H. Tuithof, Thesis, TH-Delft, 1977.

[24] H.H. Tuithof, A.J.H. Boerboom and H.L.C. Meuzelaar, Int.J.Mass Spectrom. Ion Phys. 17 (1975) 299.

[25] H.H. Tuithof, Int.J.Mass Spectrom.Ion Phys. 23 (1977) 147.

[26] R. Weber, K. Levsen, G.J. Louter, to be published.

[27] G.J. Louter, P.F.M. Stalmeier, A.J.H. Boerboom, J. Haverkamp and J. Kistemaker, Z.Naturforschung 35c (1980) 6.

[28] J.W. Dallinga, N.M.M. Nibbering, A.J.H. Boerboom and G.J. Louter, to be published.

[29] J.J. Zwinselman, C.G. van den Heuvel and N.M.M. Nibbering, in A. Quale (Ed.), Advances in Mass Spectrometry, Heyden, London, 1979, 8A, p.808.

[30] J.W. Dallinga, N.M.M. Nibbering and G.J. Louter, Org.Mass Spectrom. 16 (1981) 183.

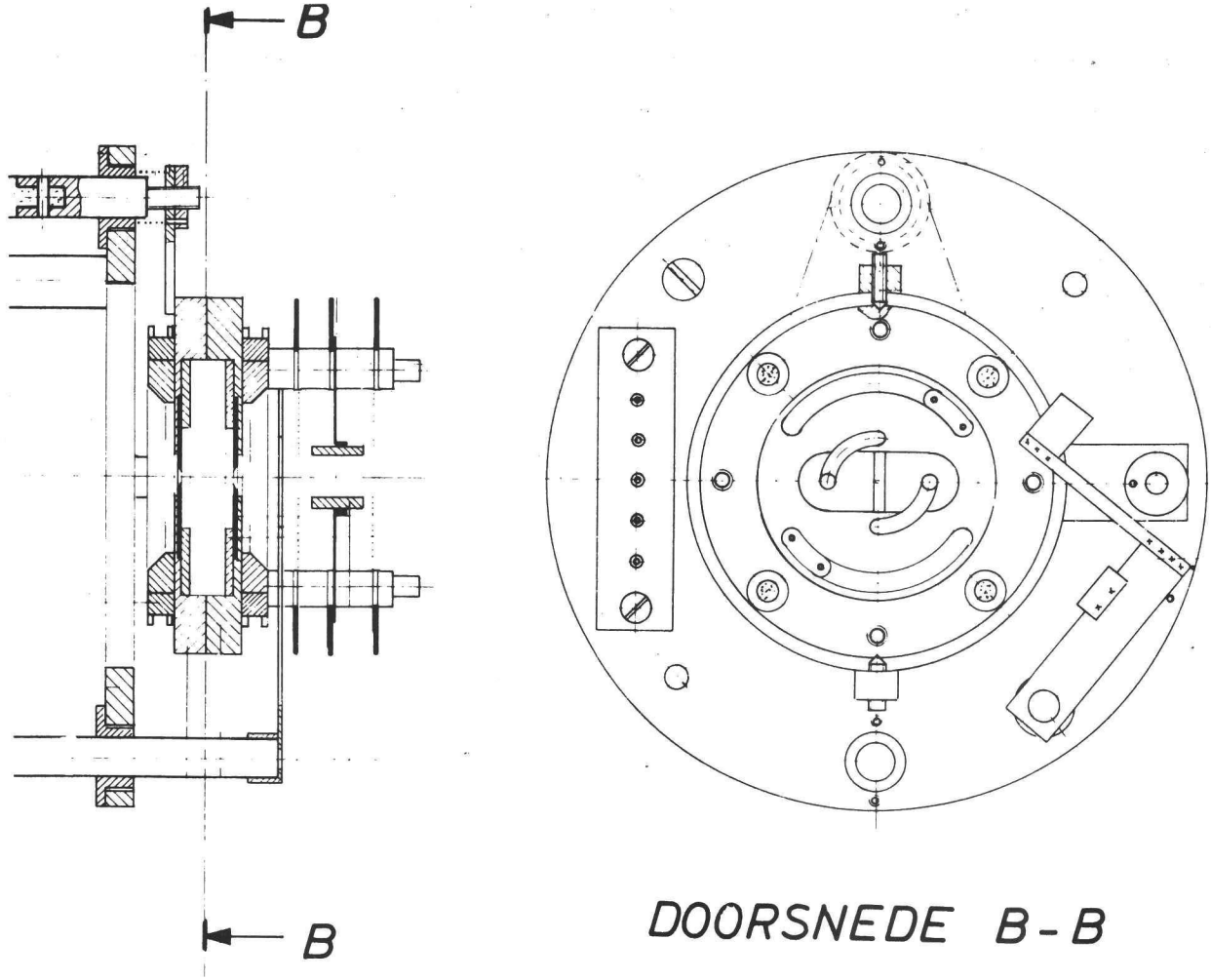

Blue print of the collision cell with adjustable entry and exit slit.

C H A P T E R 1

A TANDEM MASS SPECTROMETER FOR COLLISION-INDUCED DISSOCIATION

ABSTRACT

A tandem mass spectrometer is described for studies of collision-induced dissociation. This instrument is especially suited for investigations on organic molecules, e.g. biochemical substances, for m/z values up to 1000.

The first stage is formed by a conventional EI source and a sector magnet, and has a mass resolution of about 600. The first stage is provided with a collision gas cell at the site of the detector slit.

In the second stage the fragment ions are post-accelerated in order to reduce the relative energy-spread and to increase the resolution and transmission. The fragment spectrum is analyzed by a second magnet (R = 750 mm, deflection angle = 15^{o}) and simultaneously recorded. Quadrupoles are added in order to vary the dispersion and to aid focussing.

The ratio between the highest and lowest masses in a simultaneously detected spectrum may vary from 4 : 1 to 1.06 : 1. The resolution can be as high as 600, and the transmission from the collision cell to the CEMA ranges from 60 to 100%; the detection sensitivity can be as high as 1 ion per 10 s.

This very high sensitivity with simultaneous detection offers the possibility of measuring short-lasting phenomena, such as desorption induced by a laser pulse and flash pyrolysis.

INTRODUCTION

Structural analysis of organic ions by means of collision-induced dissociation (CID) is a new technique in mass spectrometry. Experiments have been set up with a double-focussing mass spectrometer, usually provided with a collision gas cell. This cell is situated either in the first or second field-free region of a double-focussing mass spectrometer, depending on the field sequence [1,2].

This method has been shown to provide a new dimension in the structural analysis of organic compounds, but there are still several experimental imperfections. In the first place, the fragmentation spectrum is scanned, so there is a substantial loss of ions. This means that long measuring-times are necessary, with the result that especially short-lasting phenomena such as field desorption and flash pyrolysis can hardly be investigated. Secondly, the kinetic energy release on fragmentation involves a spread of energies and angles for the dissociation products, resulting in badly-resolved spectra. the possibility of performing CID mass spectrometry with considerable mass resolution is provided by the so-called linked scan methods [3] in double-focussing mass spectrometers.

We designed a new double-stage mass spectrometer based on these considerations (fig. 1) [4]. The first stage consists of a conventional magnetic sector-type mass spectrometer; this part of our instrument does not differ essentially from similar instruments. In the second stage, however, post-acceleration is applied to reduce considerably the relative energy spread and angular spread of ions of equal mass, after the dissociation [5]. This results in a corresponding improvement in resolution and in the transmission of the fragment ions.

A magnetic field is applied for mass analysis of the fragment-ion beam. Continuing our approach of simultaneous detection [6], we incorporated quadrupole lenses for variation of the dispersion. The ions are detected with a CEMA (channeltron electron multiplier array), provided with a phosphor screen. The photons generated in the phosphor are guided through fibre optics and imaged by an optical lens onto a photodiode array.

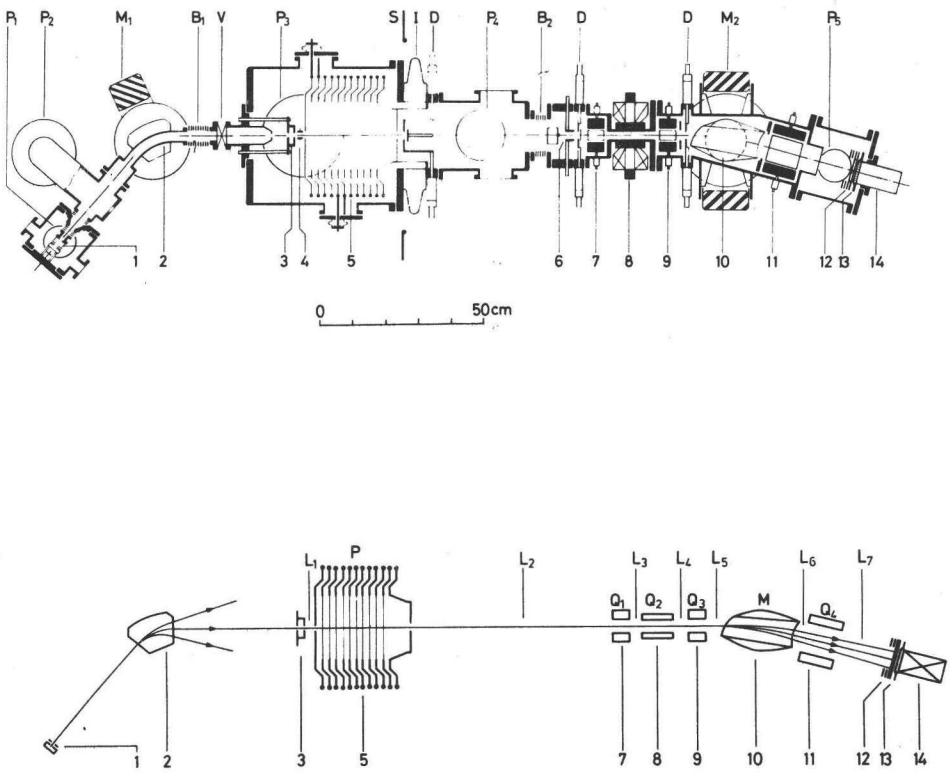

FIGURE 1

Above: top view of the apparatus. Below: simplified diagram, showing the main ion-optical functions. 1, ion source, 2, selection magnet; 3, collision gas cell; 4,6, deflection plates; 5, post-acceleration slits; 7,9,11, electrostatic quadrupoles; 8, magnetic quadrupole; 10, analysing magnet; 12, CEMA; 13, phosphor screen; 14, fibre-optic slab; P1, 2,3,4,5, oil diffusion pumps; M1,2, sector-magnet yokes, B1,2, bellows; V, valve; S, high-voltage shield; I, high-voltage insulator; D, adjustable diaphragms.

APPARATUS

The first stage

Preselection of the ions to be investigated is performed by a conventional mass spectrometer. Ions are produced in an electron-impact source and accelerated by a source potential of 500 - 10,000 V. The main orbit has a radius of 150 mm in the analysing magnet, and a deflection angle of 50°. The magnetic field strength can be varied up to 1.5 T, and is monitored and stabilized by a Hall probe. In the near future the EI source will be provided with a fully automated Curie-point pyrolysis inlet system.

The collision gas cell

The collision cell is mounted at the site of the detector slit of the first stage. It has a length of 10 mm, and the widths of the entry and exit slits are both independently adjustable up to 2.00 mm. The width of the entry slit is made variable in order to cope with the conflicting demands of high resolution as well as high transmission in the first stage, and low consumption of the target gas; similarly, the variability in the width of the exit slit enables a compromise to be found between target-gas and loss of ions due to angular spread of the beam of fragment ions. Acceptance of all fragment ions is of paramount importance for sensitivity and for the quantitative interpretation of the fragmentation processes.

The collision cell can be rotated as a unit around an axis perpendicular to the median plane in order to align the entry and exit slits, and around the main beam direction to make the slits parallel to the ion-beam height. The whole collision cell is electrically insulated, and its potential can be varied between +2 and -2 kV in order to distinguish between ions formed inside the collision cell and those formed outside. A Faraday cage is mounted directly after the collision cell. This can be deliberately placed in or out of the ion beam. This cage construction permits independent control of the first stage.

The post-acceleration stage

The post-acceleration stage, consisting of twelve equidistant electrodes, is placed after the collision cell. The slits are very wide (200 mm) in the median plane in order to prevent uncontrolled focussing action. The slits are 20 mm high in the perpendicular direction, which gives rise to focussing action. By applying an appropriate potential distribution over the twelve electrodes, the ion beam can be confined to maximize transmission through the pole-gap for the desired mass range. However, the optimum potential distribution depends to a great extent on the ratio between post- and pre-acceleration voltages, as well as on the fragmentation ratio and the width of the transmitted mass-range. This complicated material will be the subject of a subsequent investigation.

The insulator

The introduction of post-acceleration means that part of the apparatus must be well insulated electrically from the rest of the instrument as well as from earth. Either the first stage (source, selection magnet and collision chamber) should be raised to +30 kV, or the second stage (quadrupoles, analysing magnet and detector) should be lowered to -30 kV. The latter set-up gives a more easily accessible source, so that many kinds of ionization techniques can be easily applied, and so enhances the versatility of the instrument. The former possibility, however, facilitates adjustment and detection, and so could possibly improve resolution and sensitivity. Operation under both alternatives is incorporated in our instrument.

The analysing magnet

After the post-acceleration stage the ions pass a field-free region and subsequently a quadrupole triplet, a dispersing magnet, and a fourth quadrupole. The function of the quadrupole triplet will be described in combination with the function of the last quadrupole after the magnet.

A magnetic field is applied for mass analysis of the fragment-ion beam. A magnetic analyser is superior to an electrostatic analyser for two reasons:

(1) a magnetic field permits a broad spectrum to pass and to be detected simultaneously, thus increasing the sensitivity by several orders of magnitude;

(2) post-acceleration not only reduces the relative energy-spread of ions of equal mass, but also reduces the ratios of the energies of different masses.

This results in reduced dispersion. In an electrostatic analyser the dispersion tends to zero with increasing post-acceleration. In a magnetic analyser it tends to the value in a conventional mass spectrometer*).

We designed the magnet to fulfil the following requirements:

(1) simultaneous passage of a mass-range 4 : 1 of fragment ions for operation both with and without post-acceleration;

(2) mass resolution of several hundreds;

(3) width of the mass spectrum at the site of the detector after passing the final quadrupole to be 75 mm;

(4) focal plane moderately flat and perpendicular to the main beam;

(5) possibility of detection of mass 400 amu with an energy of 40 keV on the main orbit;

(6) wide pole-gap to obtain high transmission.

It is difficult to meet all these requirements simultaneously, since some are partly contradictory, but the following design was chosen: main radius of curvature 750 mm, deflection

*) The difference in mass resolution between a CID and a conventional mass spectrum should be noted. In the latter case all ions have essentially equal energy, and the mass resolution is given by $\Delta m/m = 2\Delta p/p$: whereas in the first case all ions have almost equal velocities, and the "CID" mass resolution is now $\Delta m/m = \Delta p/p$. If a magnetic analyser is applied, the use of post-acceleration results in an intermediate value. For an electrostatic analyser, the resolution is $\Delta m/m = \Delta E/E$. This expression tends to zero with increasing post-acceleration.

angle 15^{o}, gap-width 15 mm, and curved and oblique entry and exit planes. The maximum field strength is 0.9 T. A detailed description will be given in a subsequent paper.

Because of the large mass-range to be transmitted (4 : 1), the ratio of the radii of curvature of the highest and lowest of the simultaneously transported masses may also be 4 : 1 (no post-acceleration). In order to avoid too large a divergence between the orbits of these extreme masses, the angle of deflection should be small. As a result, however, the magnetic field has only a small focal strength and additional focussing is needed. This is one of the reasons for the presence of the quadrupoles.

The quadrupoles

The apparatus contains three quadrupoles (Q_1, Q_2, Q_3) in front of the analysing magnet and one (Q_4) after the magnet: Q_1, Q_2 and Q_4 are electric quadrupoles, Q_2 is magnetic. Each quadrupole serves a certain purpose, but most of the functions can only be considered simultaneously.

The function most easily understood is the variation of the dispersion by means of Q_4 [7]. An ion describing the central path through a multiple does not experience any force, so a multipole can not produce dispersion. It can, however, modify an existing dispersion. In our instrument the ion beam is dispersed by the analysing magnet, and the quadrupole Q_4 after the magnet multiplies the dispersion by a factor greater or smaller than unity. In addition, this quadrupole has a respective defocussing or focussing effect on the several ion beams.

The quadrupoles Q_1, Q_2, Q_3, in front of the magnet can compensate for this focal action, and together with Q_4 they form a zooming system, able to keep the focal plane at the right position when the dispersion is varied.

The magnetic quadrupole Q_2 has the purpose of rotating the focal plane. The exit plane is curved in order to straighten the focal plane. However, this measure is insufficient to correct for the very oblique angle between the main orbit and

the focal plane, as well as for the strong curvature of this plane. The additional rotatory effect of Q_2 is needed to obtain the right direction for the plane and sufficient depth of focus to cope with the remaining curvature. Both Q_1 and Q_3 in combination with Q_4 can be used to zoom the spectrum and to vary the dispersion. Q_1, however, is mainly used to improve transmission. If Q_1 is applied in the defocussing mode in the median plane, the beam height is confined, and a larger part of the ion beam is allowed to pass the narrow pole-gap of the analysing magnet. The final focussing onto the plane of the detector is then done by Q_3.

In practice, however, all four quadrupoles together with the magnet jointly determine the position and angle of the focal plane and the dispersion and line-width of the spectrum.

The detector

The ions are finally detected on a 75-mm double CEMA*) with 25-μm pore-size, followed by a phosphor screen. The signal is guided out of the vacuum envelope by a fibre-optic slab**). This system is very similar to that described by Tuithof et al. [6].

The present measurements were performed by imaging the 75-mm-broad line-spectrum onto a 12-mm vidicon with 500 channels, using a camera objective f = 50 mm and f/D = 1.4. Recently this photo-optical system has been replaced by a combination of a camera objective f = 85 mm and f/D = 1.4 and a 25-mm long and 0.43-mm high photodiode array***) with 1024 channels, to obtain higher spatial resolution and higher sensitivity.

The detector unit is also equipped with a conventional TV camera coupled with a monitor. In this way the lineshape can be directly observed at the rear end of the fibre-optic slab.

*) Channeltron Electron Multiplier Array, Galileo Electro-Optics Corp.; type 3075-P 20.

**) Jenaer Glaswerke, Schott und Gen., type S105.

***) Princeton Applied Research Corp., detector model 1410, controller model 1218.

The vacuum system

The various HV pumps are listed in Table 1 with unbaffled pumping speeds. The forevacuum is provided by two booster pumps of 330 and 660 l min^{-1} respectively.

TABLE 1

HV pumps and unbaffled pumping rates

Pump	Position	Pumping rate	Coolant	Working pressure[a] (torr)
P1	Source	600 l s^{-1}	Water	10^{-6}
P2	Flight tube	280	Liquid N_2	6×10^{-7}
P3	Collision cell	3500	Water	$7 \times 10^{-7} - 5 \times 10^{-5}$
P4	Flight tube	1200	Liquid N_2	6×10^{-7}
P5	CEMA	280	Liquid N_2	6×10^{-7}

[a]These pressures were measured by an ion gauge positioned directly above the baffle.

Electronics

Except for the vacuum system and for the complete photodetection system, all power supplies used in the tandem MS are electrically insulated from ground. All supplies are raised to the same potential as the frame to which they are connected.

Each supply acts as an amplifier, as its output is proportional to an adjustable low voltage at the input power supply. Two hardware controlling units, one for each stage, take care of the necessary functional relations between the several ion-optical operations. The source potential and magnetic field in the first stage are controlled by computer (PDP 11/70). The connection between the computer and the inputs of the power supplies consists of a CAMAC system, light guides (for electrical insulation) and digital-analogue converters.

The construction of the electronic system is such that the main ion-optical functions can be connected to the computer.

PERFORMANCE

First stage

The performance of the first stage was determined with conventional methods. Neon gas was introduced into the ion source, and the ion current was measured on the Faraday cage just behind the collision chamber. With a trap current of 200 μA and a gas consumption of 7.2×10^{-4} torr l s^{-1}, we obtained a current of 1.8×10^{-5} A $torr^{-1}$ on the collector. With a defining slit width of 0.23 mm for the source, we obtained a resolution of 600, measured by the 10%-valley criterion.

Second stage

Two steps can be distinguished in the transmission of the second stage: the transmission through the collision cell, and that from the cell to the CEMA.

The transmission of a collision cell depends largely on the widths of the entry and exit slits, the ratio between parent-ion energy and dissociation energy, and the ratio of the masses of precursor and daughter ions.

An important feature of our instrument is the large acceptance angle for the fragment-ion beam, due to the post-acceleration. The transmission onto the CEMA depends again on many parameters, i.e. the magnitude of the post-acceleration voltage and the adjustments of the quadrupoles. We will give only some typical results.

We chose N_2^+ as a precursor ion because of its large kinetic energy release. The entry slit of the collision cell was set at 0.23 mm, equal to the width of the source slit, the exit slit at 0.54 mm. The source potential was 4000 V and the post-acceleration 20 kV. The instrument was set to accept both N_2^+ and N^+ simultaneously on the CEMA.

Without a target gas in the collision cell, the current directly after the post-acceleration stage, as well as on the front side of the CEMA, was 1.1×10^{-11} A, equal to the current as measured directly behind the collision cell. The background pressure in the apparatus during this experiment was 7×10^{-7} torr,

so essentially no dissociation of the N_2^+ ions occurred and the beam consisted only of N_2^+. We may therefore assume a transmission of 100% for undissociated ions.

Next we introduced Ne as a target gas in the collision cell. We measured the pressure by an ion gauge situated above the diffusion pump, and the pressure in the cell was estimated to be about 4000 times higher. The reading of the gauge was multiplied by a factor of 4.35 to correct for the ionization cross section of Ne.

At a pressure of 1.9×10^{-1} torr in the collision cell, the total transmission of the second stage, including the cell, was about 50%. At this pressure, the ion current for mass 28 decreased to about 25% of its value, measured without collision gas. Measurements with other collision gases would explain whether this loss is due to scattering or to electron capture from the target gas.

EXPERIMENTAL

For alignment and optimization of the instrument we used a conventional TV camera, connected to a monitor to observe the spectrum at the rear end of the fibre-optic slab.

A simple example of a CID spectrum was obtained from isobutene (C_4H_8, M.S. = 56). This spectrum shows all possible fragments: m/z 12 - 15 (with 16 as an isotope peak), 24 - 29 (with 30 as an isotope), 36 - 41 (isotope 42) and 48 - 56 (no isotope peak).

It is fascinating to scan the primary spectrum from m/z = 56 down to 12, while seeing the successive CID spectra flashing on and off. Each time a complete spectrum flashes on, in subsequent spectra the highest peak disappears; the remaining peaks, of course, vary strongly in intensity. On passing m/z = 32 (from background O_2), only 32 and 16 flash on.

Figure 2a shows the simultaneously recorded spectrum for mass 24 - 56, as directly photographed from the rear end of the fibre-optic slab. Figure 2b shows the performance of the ion-optical zooming system on the C_3 group. The curvature of the

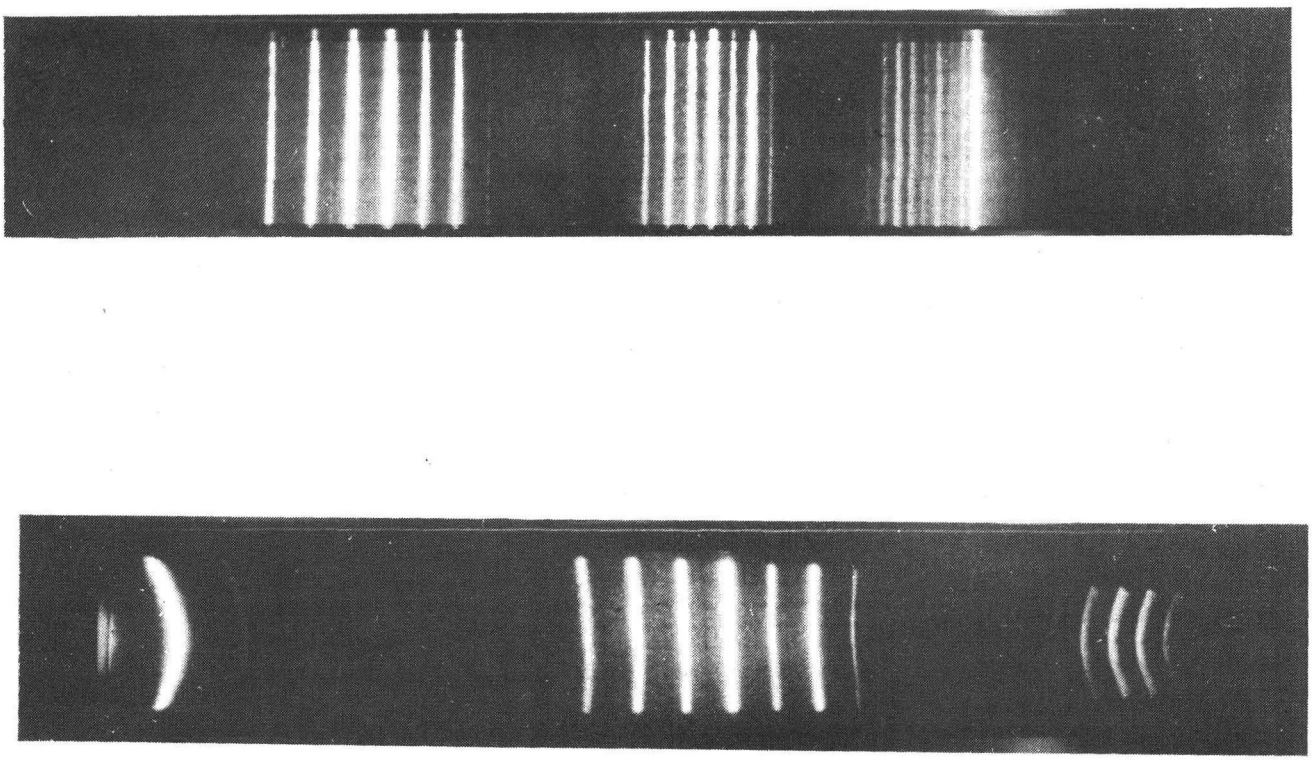

FIGURE 2

The isobutene spectrum obtained directly from the fibre-optic slab. Precursor ion, m/z = 56; source potential, 6,400 V; post-acceleration, 30,000 V. (a) mass ratio 4 : 1, no use of the fourth (electrostatic) quadrupole; (b) mass ratio 1.8 : 1, obtained by zooming effect of the fourth quadrupole.

lines for the C_2 and C_4 groups is caused by third-order aberrations in the quadrupole lens Q_4. Quantitative measurements were made, however, using the vidicon as a photo-detector system.

The mass resolution of the second stage is demonstrated in fig. 3, using benzonitrile (C_6H_5CN, M.W. = 103) as a test substance. It should be realized that the resolution of CID

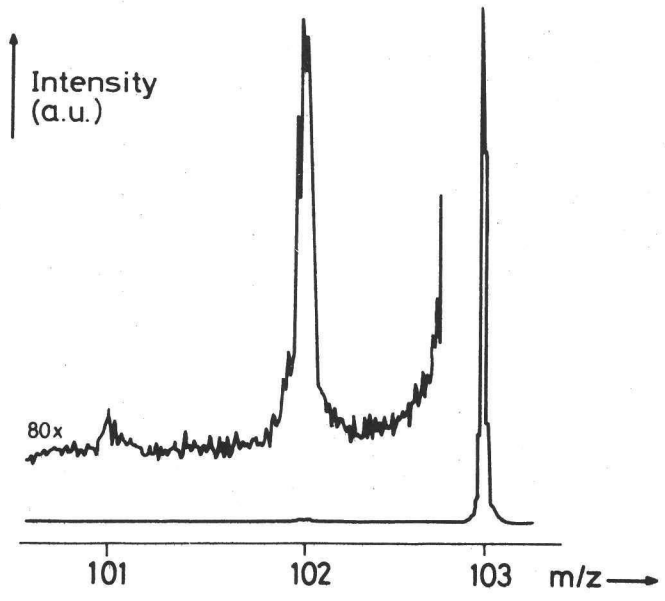

FIGURE 3

Ion-optical close-up of precursor M and the fragments M - 1 and M - 2 of mass 103 from benzonitrile. Total measuring time, 12 s; flux of ions of mass 103 emerging from collision cell, 2000 ions s^{-1}: peak m/z = 102 has been formed by 20 ions s^{-1}; source potential, 8,600 V; post-acceleration, 2,500 V. Ne was used as the collision gas. The CID mass resolution for peak 103 is better than 1,000.

spectra cannot be given by a simple figure. The peak-width is largely dependent on the kinetic energy release on fragmentation. From fig. 3 it follows that the CID mass resolution of fragments without dissociation energy would be better than 1000, judging from the width of the precursor ion peak 103. For the fragment-ion peak 102, the mass resolution is about 500 at a post-acceleration of 2500 V.

In the furture, the CID resolution will be increased considerably by using a photodiode array with twice the number of channels, and by increasing the applied voltage on Q_4. Peak 101 in fig. 3 clearly demonstrates the sensitivity of the second stage, including the detection system. This peak is formed in 12 s by about 12 ions, distributed over 8 channels of the vidicon.

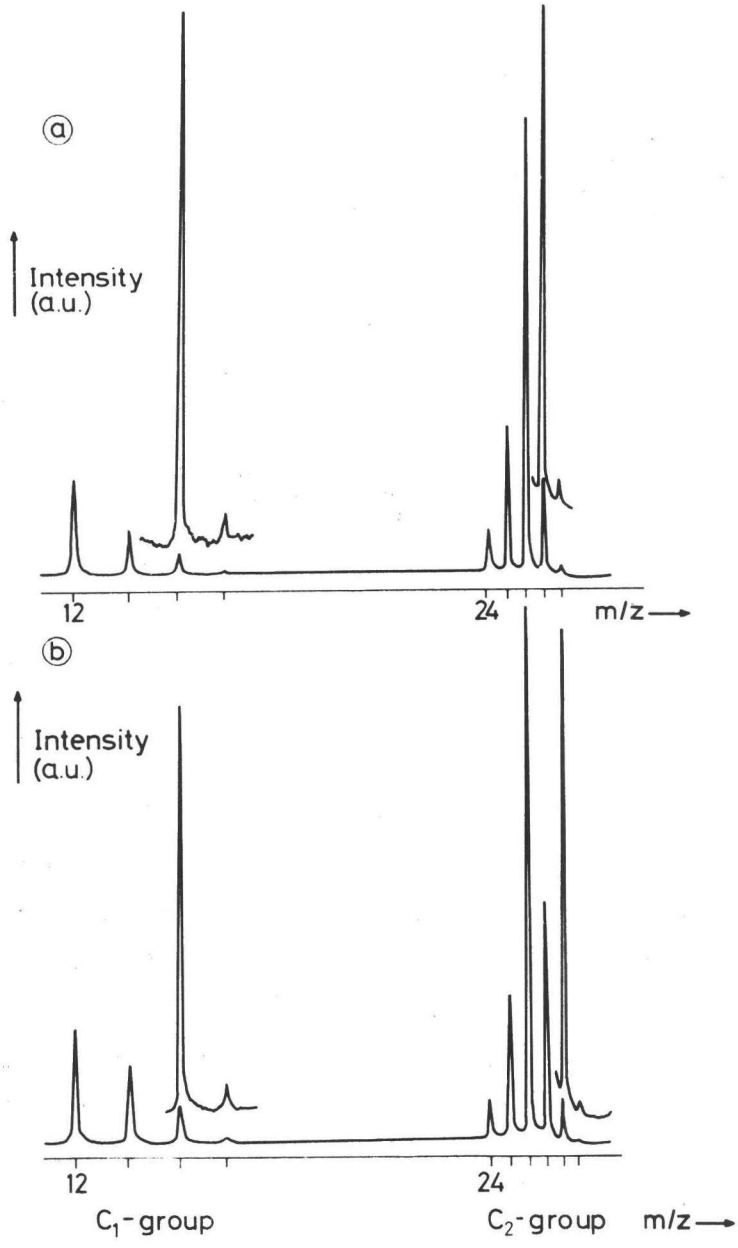

FIGURE 4

CID spectra of the C_1 and C_2 groups of benzonitrile. (a) precursor-ion mass 103 (containing less than 0.1% C_6H_4CN with one isotope); (b) precursor-ion mass 104 (containing one isotope ^{13}C, ^{15}N or ^{2}D). Source potential, 4,000 V; post-acceleration, 30,000 V; total ion current (mass 12 - 104): for (a), 7.2×10^{-15} A; for (b), 8.0×10^{-15} A; measuring time, 6.7 s for each spectrum. The overall resolution is about 70. Note that the C_n-group contains all fragments with n carbon atoms and all with (n - 1) carbon atoms and 1 nitrogen atom.

E R R A T A

Titelblad, 6^{e} regel van onder:

"...kollege..." moet zijn "...college...".

Pagina 23, 7^{e} regel van onder:

"...C_3 groups..." moet zijn "...C_3-C_6 groups...".

Pagina 85, 13^{e} regel van boven:

"...the dark ion count rate density of..." moet zijn "...the dark current density, and amounts...".

Amsterdam, 23 februari 1982

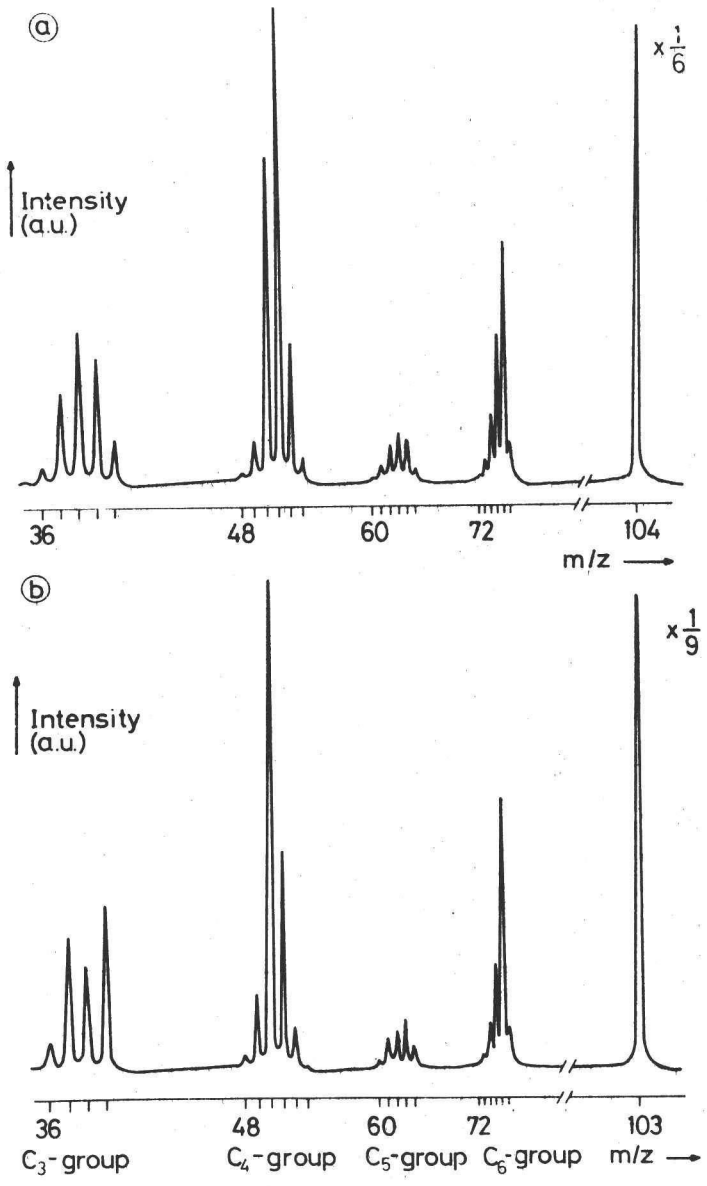

FIGURE 5

CID spectra of the C_3 groups for the precursor ions of benzonitrile. The measuring conditions were the same as in fig. 4. Due to the limitations of the vidicon, we did not simultaneously detect the full mass-range of 4 : 1. Measuring times of the $C_3 - C_6$ groups were 6.7 s for each spectrum. For the parent ions measuring times were also 6.7 s, but here the total ion currents were reduced to 1.2×10^{-15} A in (a) and to 9.1×10^{-16} A in (b).

Finally, figs. 4 and 5 show the full CID spectra of the parent-ion 103 and its isotope 104. The variation of the dispersion can be seen by comparing the simultaneously recorded mass-ranges in fig. 2a and fig. 3. In fig. 2a, the ratio of the highest and lowest masses is about 4 : 1, in fig. 4, the full width of the channelplate would permit a ratio of 1.06 : 1 to be simultaneously recorded.

The effect of post-acceleration is shown in fig. 6. For several years the effect of kinetic energy release on resolution has been a subject of discussion [2]. Important improvements were obtained by McLafferty [8], who increased the source potential from 4 to 8 kV. Tuifhof [5] has shown that greater improvement in resolution can be expected by accelerating the fragment ions after the dissociation (post-acceleration). A direct comparison between the two kinds of acceleration is made in fig. 6. The measurements are compared with the calculations introduced in Tuifhof's paper.

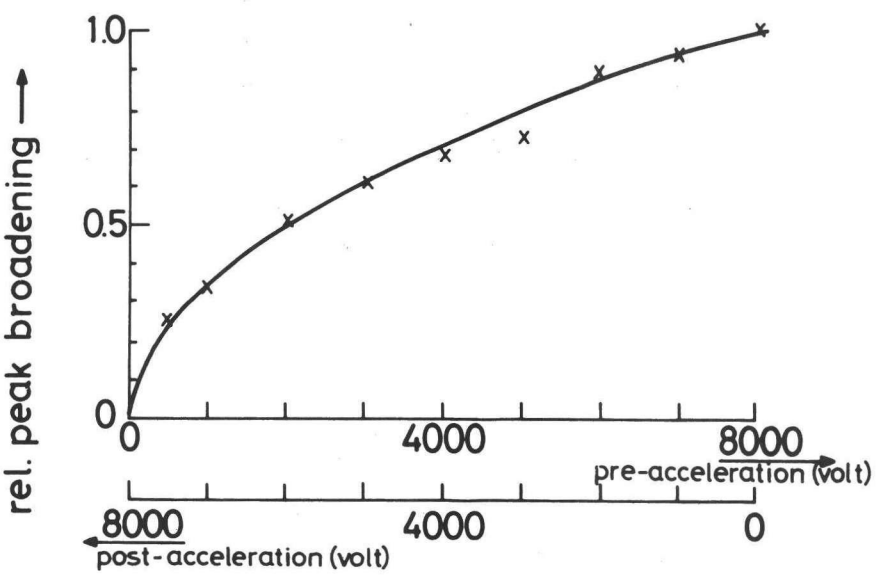

FIGURE 6

Peak-broadening of N^+ from N_2^+ due to the kinetic energy release as a function of post-acceleration. The sum of pre- and post-acceleration was kept constant at 8,000 V. Energy of the ionizing electrons was 50 eV. Helium was used as the collision gas. (×), measurements; (——), calculated peak-broadening.

The experiments performed using N_2^+ as a precursor ion because of its high kinetic energy release on fragmentation. We measured the extra peak-broadening caused by this effect. The effectiveness of post-acceleration is clearly demonstrated.

CONCLUSION

Our first measurements indicate that the combination of simultaneous detection and post-acceleration applied in the new instrument presented for CID mass spectrometry enables measurements with high sensitivity and considerable resolution to be made. This makes the instrument highly suited for the investigation of short-lasting phenomena (microseconds), such as flash pyrolysis [9] and laser pulse-desorption [10].

REFERENCES

[1] K.R. Jennings, Int.J.Mass Spectrom.Ion Phys. 1 (1968) 227; F.W. McLafferty, P.F. Bente, III, R. Kornfeld, Shih-Chuan Tsai and I. Howe, J.Am.Chem.Soc. 95 (1973) 2120; F.W. McLafferty, R. Kornfeld, W.F. Haddon, K. Levsen, I. Sakai, P.F. Bente, III, Shih-Chuan Tsai and H.D.R. Schuddemage, J.Am.Chem.Soc. 95 (1973) 3886; K. Levsen and H. Schwarz, Angew.Chem. 88 (1976) 589.

[2] R.G. Cooks, J.H. Beynon, R.M. Caprioli and G.R. Lester, Metastable Ions, Elsevier, Amsterdam, 1973.

[3] A.P. Bruins, K.R. Jennings and S. Evans, Int.J.Mass Spectrom.Ion Phys. 26 (1978) 395.

[4] H.H. Tuithof, A.J.H. Boerboom, P.G. Kistemaker and H.L.C. Meuzelaar, in: N.R. Daly (Ed.), Advances in Mass Spectrometry, Heyden, London, 1977, p.838.

[5] H.H. Tuithof, Int.J.Mass Spectrom.Ion Phys. 23 (1977) 147.

[6] H.H. Tuithof, A.J.H. Boerboom and H.L.C. Meuzelaar, Int.J.Mass Spectrom.Ion Phys. 17 (1975) 299.

[7] H.H. Tuithof and A.J.H. Boerboom, Int.J.Mass Spectrom.Ion Phys. 20 (1976) 107.

[8] T. Wachs, C.C. van de Sande, P.F. Bente, III, P.P. Dymerski and F.W. McLafferty, Int.J.Mass Spectrom.Ion Phys. 23 (1977) 21.

[9] H.L.C. Meuzelaar, J. Haverkamp and F.D. Hileman, Curie-Point Mass Spectrometry of Biomaterials; Compendium and Atlas, Elsevier, Amsterdan, 1980.

[10] P.G. Kistemaker, A.J.H. Boerboom and H.L.C. Meuzelaar, in: D. Price and J.F.J. Todd (Eds.), Dynamic Mass Spectrometry, Vol.4, Heyden, London, 1975, Chap.9;
A.J.H. Boerboom, P.G. Kistemaker, M.A. Posthumus and H.L.C. Meuzelaar, in: D. Price and J.F.J. Todd (Eds.), Dynamic Mass Spectrometry, Vol.5, Heyden, London, 1978, Chap.9.

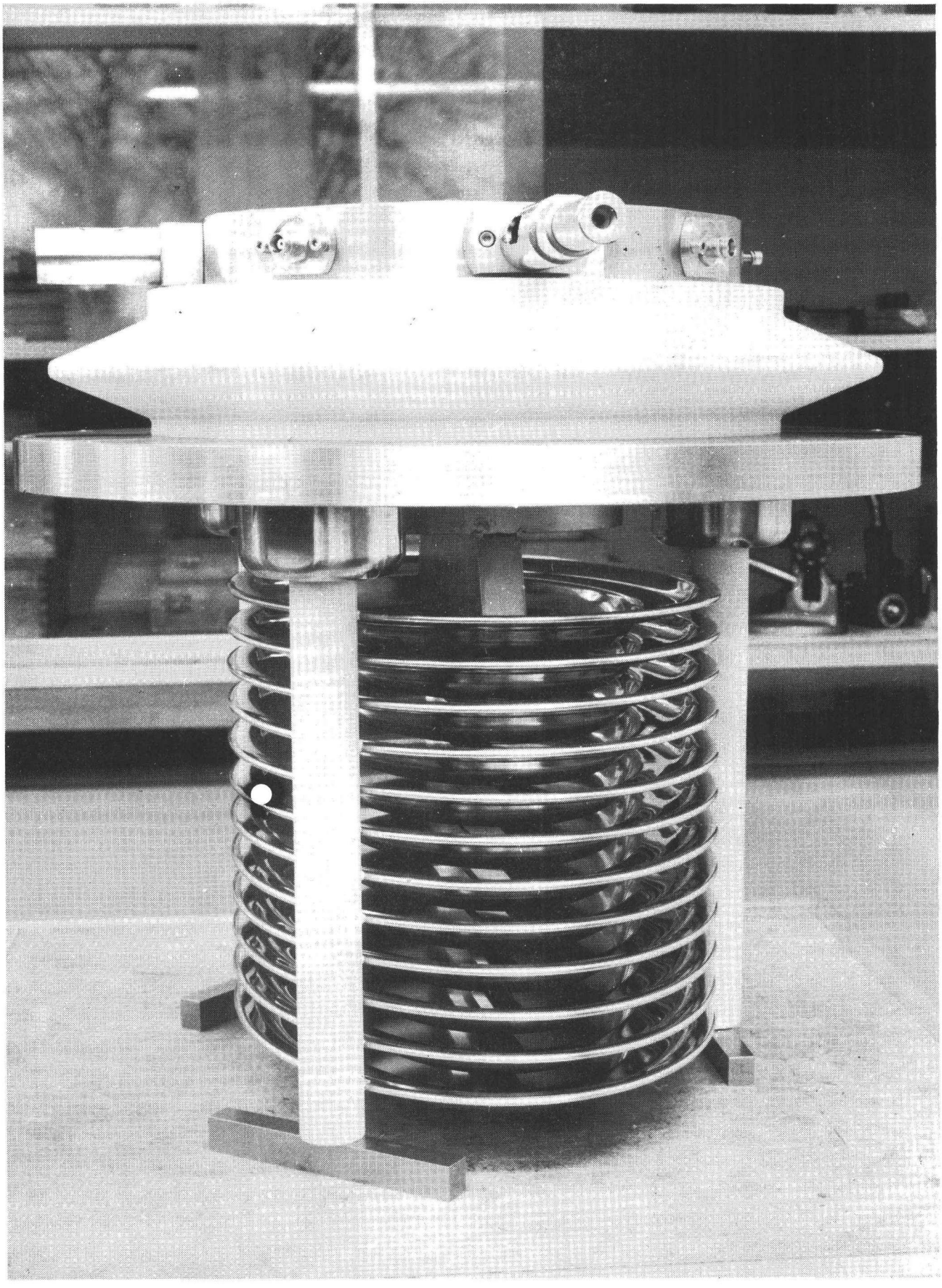

Twelve slotted stainless steel "horeca dishes" are used as electrodes of the post-acceleration section of the double stage mass spectrometer.

C H A P T E R 2

APPLICATION OF MATRIX CALCULATION I: DESIGN AND ADJUSTMENT OF A TANDEM MASS SPECTROMETER FOR COLLISION-ACTIVATED DISSOCIATION (CAD)

ABSTRACT

A matrix representation of the ion optics of the analyzing stage has been used in a computer model of a tandem mass spectrometer with simultaneous detection for CAD. The matrix algorithm of this model is discussed here as an elegant way of describing the ion optics in a first-order approximation. The accuracy of the calculations is illustrated by comparing calculated and measured adjustments of the instrument under normal experimental conditions. The ion-optical possibilities with respect to transmission, mass resolution and range of simultaneously detectable masses are discussed. The calculated influence of several ion optical parameters on the shape and position of the mass focal plane is discussed.

The experimental values of mass range, mass resolution and ion transmission agree very well with the calculations. Moreover, the computer model appears to be a useful tool for giving clear insight into the operation of the rather complex ion optics of the instrument. The calculations have been further developed towards higher accuracy, making possible automatic focusing of the mass focal plane onto the detector. The computer program has also been used for the development of an automatic mass-scaling procedure for the fragment mass-spectrum. This subject will be discussed in a subsequent article.

The generalized and relatively simple representation of the ion optics used in our computer model of the mass spectrometer has proved to be an important aid in the design and further development of the instrument.

INTRODUCTION

The last decade has shown a rapid growth of collision-activated dissociation (CAD) mass spectrometry for the analysis of ion structures, the elucidation of fragmentation mechanisms [1] and the analysis of complex mixtures [2]. The initial problems of low mass-resolution of the fragment spectra and of poor transmission of the fragment ions, both due to the kinetic energy released on fragmentation [3], have been gradually solved. The mass resolution can be increased by applying linked-scan techniques [4]. The transmission of fragment ions is enhanced by confining the collisions to a small region by using a collision cell [5] or a jet of collision gas [6]. Additional ion-lenses have been incorporated to reach higher sensitivities in the detection of fragment ions [6,7]. Tandem and triple quadrupole mass spectrometers [8] provide very elegant ways of combining high transmission with unit mass resolution up to m/z 1000. The CAD spectra obtained with these instruments are, in contrast to the case for high-energy instruments, caused by low-energy collisions (below 100 eV).

In the tandem mass spectrometer for CAD which has been designed and constructed in our Institute, we have succeeded in combining transmission (up to nearly 100%) and high mass-resolution (up to 1000). Reports of the achievements of this instrument have been published previously [9]. Moreover, an extra dimension has been introduced by the application of a simultaneous detection system with a channeltron electron-multiplier array (CEMA). On the one hand, simultaneous detection of a mass spectrum can increase the sensitivity by several orders of magnitude: therefore the instrument is extremely well fitted to combine, for example, field desorption (FD) and CAD. On the other hand, this technique is very well suited for the analysis of short-lasting phenomena, as for example, flash-pyrolysis [10] and laser-pulse desorption [11].

In the design of the second stage of the tandem mass spectrometer we used a mathematical simulation of the instrument on a PDP 11/70 computer. In this model we applied the so-called "transfer-matrix" representation of the ion optical

devices [12]. In earlier work [13] this method has already been shown successful in the design of a sector-magnet spectrometer with simultaneous detection and variable dispersion. The computer simulation could also be very successfully applied for the automatic tuning of the instrument.

ION OPTICAL TRANSFER MATRICES

Introduction

In the case of the tandem mass spectrometer, which comprises a considerable number of ion optical devices, it is convenient to describe the ion optics by using the so-called "transfer matrix" representation [12,14,15]. A transfer matrix A relates the position and slope of an ion ray at some plane perpendicular to the ion optical axis at $z = z_1$, to its position and slope in a similar plane at $z = z_2$. In fig. 1 this situation is depicted for the simple case of an ion beam in a field-free region of length l. At $z = z_1$ the position of the ray, x_1, and its slope, x_1', are given by the vector X_1:

$$X_1 = \begin{pmatrix} x_1 \\ x_1' \end{pmatrix} \qquad (1)$$

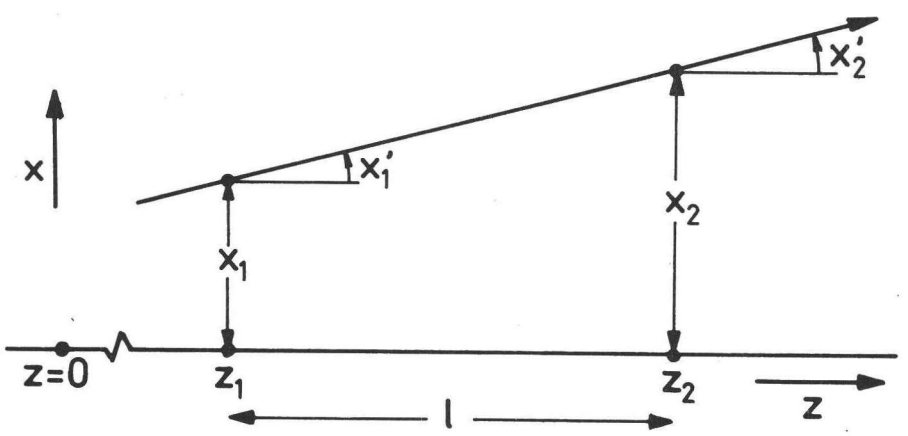

FIGURE 1

The trajectory of an ion orbit in a field-free space. At every value of z the trajectory is described by its position x_i and its slope x_i' with respect to the z-axis.

where

$$x_1' = \left(\frac{dx}{dz}\right)_{z=z_1} \tag{2}$$

The relation between X_1 and the vector X_2 at $z = z_2$ is, for this case of a field-free region,

$$X_2 = \begin{pmatrix} 1 & (z_2 - z_1) \\ 0 & 1 \end{pmatrix} . X_1 = A . X_1 \tag{3}$$

The transformation in fig. 1 is considered in the xz-plane, which, in the nomenclature used here, coincides with the median plane of the mass spectrometer. We define the y-direction perpendicular to the xz-plane. In the yz-plane, Y_1 is given by

$$Y_1 = \begin{pmatrix} y_1 \\ y_1' \end{pmatrix} \tag{4}$$

The transfer matrix from $z = z_1$ to $z = z_2$ within the yz-plane will be denoted with an asterisk, i.e.

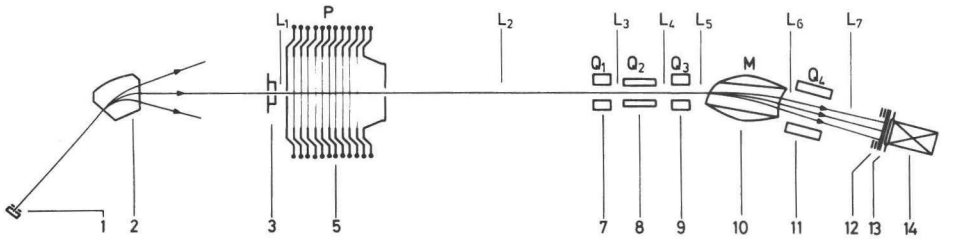

FIGURE 2

Simplified top view of the instrument, showing the main ion optical functions and indicating the various transfer matrices mentioned in the text. 1, ion source; 2, selection magnet; 3, collision cell; 5, post-acceleration section (electrodes A to L from left to right); 7,9,11, electrostatic quadrupole lenses; 8, magnetic quadrupole lens; 10, analyzing magnet; 12, channeltron electron multiplier array (CEMA); 13, phosphor screen; 14, fibre-optics slab.

$$Y_2 = A^* \cdot Y_1 \qquad (5)$$

A simplified diagram of the mass spectrometer is given in fig. 2. This figure gives a survey of the transfer matrices used for our ion optical calculations. Our aim is to calculate the vector $X^{(CH)}$ on the detector from the vector $X^{(CC)}$ at the exit slit of the collision cell. The relation is given by

$$X^{(CH)} = L_7 \cdot Q_4 \cdot L_6 \cdot M \cdot L_5 \cdot Q_3 \cdot L_4 \cdot Q_2 \cdot L_3 \cdot Q_1 \cdot L_2 \cdot P \cdot L_1 \cdot X^{(CC)} \qquad (6)$$

Field-free regions

Several field-free regions are incorporated in the tandem mass spectrometer. In fig. 2 these regions are indicated by L_i, with i numbered 1 - 7. All "drift-length matrices" are of the type given by eq. (3), so if the drift length is l_i we can write

$$L_i = \begin{pmatrix} 1 & l_i \\ 0 & 1 \end{pmatrix} \qquad (7)$$

Post-acceleration section

One of the most important features of the tandem mass spectrometer is the acceleration of the fragment ions originating from collisions in the collision cell. The kinetic energy released on collision causes a momentum spread. Compared with an equal acceleration of the precursor ions, post-acceleration results in a larger relative reduction of this spread. The difference between post- and pre-acceleration increased with decreasing ratio of the masses of the fragments and the precursor ion.

Generally, the electrodes bounding an accelerating field have an inconvenient focusing action. When a precursor ion of mass m_p decomposes according to

$$m_p^+ \rightarrow m_{f1}^+ + m_{f2} \qquad (8)$$

the energy E_{f1} of the fragment of mass m_{f1} is given by

$$E_{f1} = (m_{f1}/m_p)\ E_p \qquad (9)$$

where E_p is the energy of the precursor ion. The energy of the fragment ions, therefore, is mass-dependent and so is the focusing action of the electrodes of the post-acceleration section.

In order to avoid this focal action in the median plane, slit-shaped accelerating electrodes (20 × 200 mm) were introduced, the lengths of the slits being situated parallel to the xz-plane (median plane). When slit-shaped electrodes are used, the focusing action perpendicular to the median plane is twice as great as from electrodes with circular apertures. Though this does not affect the imaging properties of the second stage in the median plane, the total transmission may be substantially reduced, for strong lens action is often correlated with high angular magnification. In order to reduce the influence of the lens action of the post-acceleration system as a whole, we used a combination of positive and negative lenses, consisting of 12 slit-shaped and equidistant electrodes (inter-electrode distance, 20 mm). These electrodes are indicated by the letters A - L (left - right in fig. 2).

Before defining potentials in the double-stage mass spectrometer, we emphasize here that all potentials mentioned in this article are ion optical potentials and are related to the precursor ion m_p^+.

The first two electrodes, A and B, are kept at an ion optical potential V_p, the accelerating voltage in the source of the precursor ion and of the housing of the first stage. Of the remaining ten electrodes, the five electrodes D, F, H, J and L are independently adjustable. The others are kept at the average potential of their neighbouring electrodes. Electrode L has a potential V_{PA}, which is also the potential of the housing of the second stage. The post-acceleration voltage

$V_{PA} - V_P$ represents the total extra energy obtained in the post-acceleration section.

The five electric fields between electrodes B and L can be described by five matrices. The general form of a transfer matrix for an axial electric field is

$$A^{ax}_{1,2} = \begin{pmatrix} 1 & 2d\sqrt{E_1}/(\sqrt{E_1} + \sqrt{E_2}) \\ 0 & \sqrt{E_1/E_2} \end{pmatrix} \tag{10}$$

where E_1 is the ion energy at the beginning and E_2 the energy at the end of the field, and d is the field length. For the transfer matrix A_{BD} between the electrodes B and D, with respective ion optical potentials V_B and V_D, we write

$$A_{BD} = \begin{pmatrix} 1 & 2d\left(1 + \left(\frac{m_{f1}V_p + m_p(V_D - V_p)}{m_{f1}V_p + m_p(V_B - V_p)}\right)^{\frac{1}{2}}\right)^{-1} \\ 0 & \left(\frac{m_{f1}V_p + m_p(V_B - V_p)}{m_{f1}V_p + m_p(V_D - V_p)}\right)^{\frac{1}{2}} \end{pmatrix} \tag{11}$$

The field-free region between A and B is considered as part of the drift-length matrix L_1. The effect of the complete post-acceleration section in the median plane is given by the matrix product

$$P = A_{JL} \cdot A_{HJ} \cdot A_{FH} \cdot A_{DF} \cdot A_{BD} \tag{12}$$

Perpendicular to the median plane also the focusing action of the slits has to be taken into account. The general transfer matrix for a slit electrode is given by

$$A^{slit}_{1,2} = \begin{pmatrix} 1 & 0 \\ -(F_2 - F_1)/2V & 1 \end{pmatrix} \tag{13}$$

where F_1 and F_2 are respectively the electric field strengths in front of and behind the slit, and V is the ion optical potential of the fragment ions. This matrix must be considered

for each electrode separating regions with different electrical field strengths.

For the "lens matrix" F_D^* of electrode D we can write

$$F_D^* = \begin{pmatrix} 1 & 0 \\ \dfrac{2V_D - V_B - V_F}{2d[(m_{f1}/m_p)V_P + (V_D - V_p)]} & 1 \end{pmatrix} \qquad (14)$$

Now we can write the transfer matrix of the post-acceleration section perpendicular to the median plane, as

$$P^* = F_L^* \cdot A_{JL}^* \cdot F_J^* \cdot A_{HJ}^* \cdot F_H^* \cdot A_{FH}^* \cdot F_F^* \cdot A_{DF}^* \cdot F_D^* \cdot A_{BD}^* \cdot F_B^* \qquad (15)$$

where the accelerating matrices in eq. (15) are of course the same as in eq. (12).

The above relation (eq. (15)) was actually used by Tuithof [17] in the design of a post-accelerating section. The purpose of the present calculations is to determine an optimum potential-distribution over the electrodes for the transmission of fragment ion beams through a circular aperture of diameter 30 mm, situated at the end of the second field-free region.

TABLE 1

Calculated voltage distributions of the post-acceleration section at two values of the pre-acceleration potential, for optimum transmission in the y-direction of a fragment-ion beam through a round aperture (30 mm diameter) at 700 mm distance from the post-acceleration section.

V_S^*	Ion optical potentials (kV)					
	V_A	V_D	V_F	V_H	V_I	V_{PA}
0	4	8	10.5	14	16.5	34
0	10	16	20	26	22.5	40

* Source potential

As the focusing action of the slit lenses is energy-dependent, the beam height at the aperture is dependent on the ratio of the masses of fragment and precursor ions, the source potential, and the post-accelerating potential. In Table 1, two calculated optimum adjustments of the electrode potentials as found by Tuithof [17] are given. For these calculations the estimated maximum exit angle out of the collision cell is 0.1 rad.

Analyzing magnet

For the analysis of the masses of the fragment ions we use a sector magnet. This is preferable to an energy analyzer because a large range of masses can be simultaneously transmitted through a sector magnet. Moreover, Louter et al. [9] have demonstrated that the mass resolution of CAD spectra increases when a sector magnet is used rather than an energy analyzer.

The magnet used in our instrument has a deflection angle ϕ_o of 15^o, and the radius R_o of the orbit described by the main ion beam (ions of mass m_{fo}) is 750 mm. These values were chosen as the result of considerations with respect to the performance required of the tandem mass spectrometer, as discussed previously [9]. With this small deflection angle the focusing action of the magnet itself is small. Therefore, extra focusing by quadrupole lenses is incorporated. However, in contrast with a magnet, which possesses a focal plane determined by its mechanical dimensions, the focusing action of a quadrupole lens depends on the energy or momentum of the ions. Therefore the shape of the focal plane for the combination of a quadrupole with a magnet changes with the ion mass and with the values of V_p, V_{PA} and m_p. Therefore, we tried initially to optimize the shape of the sector magnet with respect to the shape and position of the focal plane [17]. The parameters varied were the entry angle β_I, the exit angle β_E of the main ion beam, and the radius of curvature R_E of the exit plane (fig. 3). The values of R_o and ϕ_o were fixed parameters in the optimization procedure; their values were chosen on the basis of considerations

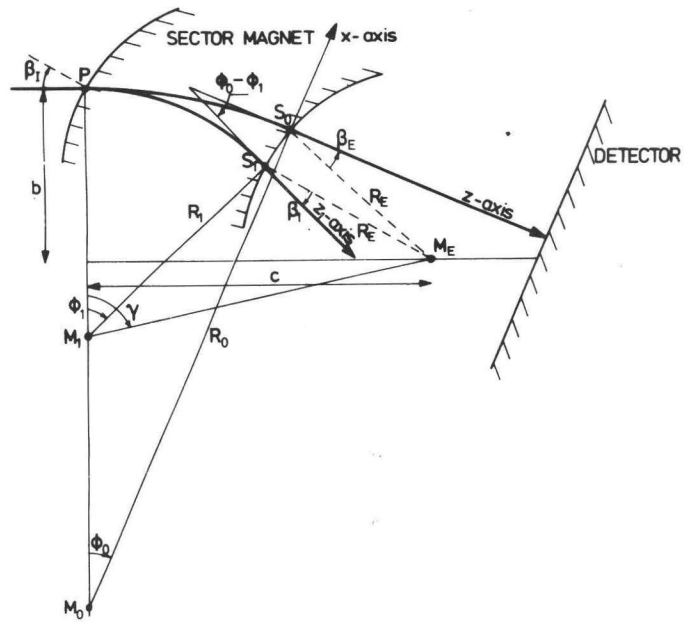

FIGURE 3

Trajectories of fragment ions of mass m_{fo} and m_{f1} through the analyzing magnet. The main radius of curvature R_o is 750 mm, at a deflection angle ϕ_o of 15^o. In the final design, the parameters were $\beta_I = 30^o$, $\beta_E = 0^o$ and $R_E = 100$ mm.

with respect to the range of simultaneously detectable masses (a mass ratio of 1 : 4 has been achieved), the highest transmittable mass at an energy of 34 keV (~ 650 u, for $R_o = 750$ mm), and the maximum obtainable magnetic field strength at a pole-shoe gap of 15 mm (~ 0.9 tesla [9]).

For the transfer matrix M of the analyzing magnet we can write

$$M = \begin{pmatrix} \dfrac{\cos(\phi_1 + \beta_I)}{\cos \beta_I} & R_1 \sin \phi_1 \\ \dfrac{-\sin(\phi_1 + \beta_1 + \beta_I)}{R_1 \cos \beta_1 \cos \beta_I} & \dfrac{\cos(\phi_1 + \beta_1)}{\cos \beta_1} \end{pmatrix} \qquad (16)$$

where R_1 is the radius of the orbit described by fragment ions of mass m_{f1}. For R_1 we can write

$$R_1 = R_o\{[m_{f1}V_p + m_p(V_{PA} - V_p)]/[m_{fo}V_p + m_p(V_{PA} - V_p)]\}^{\frac{1}{2}} \qquad (17)$$

The mass-dependent deflection angle ϕ_1 is a more complicated function of the parameters of the sector magnet. It can be written as

$$\phi_1 = \theta + \arccos\{(R_E^2 - 2R_1^2 - b^2 - c^2 + 2bR_1)/2R_1(b^2 + c^2 - 2bR_1 + 1)^{\frac{1}{2}}\} \qquad (18)$$

In this expression the parameters b and c can be derived from fig. 3 by using trigonometric relations. The angle θ is related to the angle γ in fig. 3 and can be found by solving

$$\theta = \gamma - 180^o = \arctan\{c/(R_1 - b)\} \qquad (19)$$

The exit angle β_1 of fragments of mass m_{f1} can be written as

$$\beta_1 = 90^o + \phi_1 - \theta + \arcsin\{(R_1/R_E)\sin(\phi_1 - \theta)\} \qquad (20)$$

As we have seen above, the position vectors used in the mathematical representation of the ion trajectories refer to a coordinate frame. Up to the analyzing magnet this frame is defined unambiguously. Behind the magnet, however, the z-axis is "dispersed", depending on the momentum of the fragment ions. In fig. 3 the z-axis and the z_1-axis are two examples of this "dispersion" of the original z-axis. With respect to the ion optics behind the magnet we define a new xz-frame as depicted in fig. 3. The new z-axis coincides with the reference axis for fragment ions describing the main orbit.

The position of the trajectory of ions of mass m_{f1} behind the magnet is calculated according to the following procedure. Firstly, the position vector $X^{(EM)}$ of the trajectory at the exit plane of the magnet is determined by solving (compare with eq. (6)) the relation

$$X^{(EM)} = M \cdot L_5 \cdot Q_3 \cdot L_4 \cdot Q_2 \cdot L_3 \cdot Q_1 \cdot L_2 \cdot P \cdot L_1 \cdot X^{(CC)} \qquad (21)$$

as $X^{(EM)}$ refers to the z_1-axis, the coordinates $(S_1)_x$ and $(S_1)_z$ must also be calculated, according to

$$(S_1)_x = R_1 \cos(\phi_1 - \phi_o) - (R_1 - R_o) \cos \phi_o - R_o \tag{22}$$

$$(S_1)_z = R_1 \sin(\phi_1 - \phi_o) + (R_1 - R_o) \sin \phi_o \tag{23}$$

For the exit direction S_1' with respect to the z-axis we can write

$$S_1' = \frac{dS_1}{dz} = \phi_o - \phi_1 \tag{24}$$

Quadrupole lenses

As the focusing action of the sector magnet in the median plane is too small to form a real image behind the analyzing magnet, we use additional focusing devices to obtain an image plane at the site of the detector, at a distance of ~ 295 mm from the magnet exit plane. Apart from focusing action in the median plane, however, some focusing perpendicular to the median plane is also desirable. Such focusing permits optimization of the transmission through the second stage and especially through the gap of the magnet.

Quadrupole lenses generally have different lens strengths in two perpendicular directions. This is one of the reasons for their use in our instrument. In our calculations we use the paraxial approximation with a matrix formalism as described by Banford [22]. The transfer matrix in one plane can generally be given by

$$Q_i = \begin{pmatrix} \cos(k_i l_{Qi}) & k_i^{-1} \sin(k_i l_{Qi}) \\ -k_i \sin(k_i l_{Qi}) & \cos(k_i l_{Qi}) \end{pmatrix} \tag{25}$$

with $i = 1,2,3$ or 4 and where l_{Qi} is the effective quadrupole length. Here k_i is the so-called lens strength parameter, which is connected with the lens strength of Q_i. In the direction perpendiculat to that considered in eq. (25) it is given by

$$k_i^* = k_i \sqrt{-1} \tag{26}$$

Substitution of eq. (26) into (25) results in an expression for Q_i^* containing hyperbolic functions. This corresponds to a diverging lens action when k_i has a real value.

For the three electrostatic quadrupole lenses in our system the parameters k_i can be solved from

$$k_i^2 = (1/a_i^2)(V_{Qi} - V_{PA})/V_{fj} \tag{27}$$

where V_{Qi} is the ion optical potential of the rods of Q_i in the median plane, a_i is the radius of the inscribed circle of the corresponding lens, and V_{fj} is the ion optical potential of fragment ions of mass m_{fj}.

As $(V_{Qi} - V_{PA})$ can have both a positive and a negative value, it follows from eq. (27) that k_i can be either real or strictly imaginary. In the latter case the quadrupole is a diverging ion-lens in the median plane. From eq. (26) it then follows that a focusing lens-action is present perpendicular to the median plane when k_i is imaginary and thus k_i real. For V_{fj} we can write

$$V_{fj} = E_{fj}/e = (m_{fj}/m_p)V_p + V_{PA} - V_p \tag{28}$$

in which e is the elementary charge. From eq. (28) it follows that V_{fj} and thereby k_i is mass-dependent.

The parameter k_2 of the magnetic quadrupole lens is found by solving

$$k_2^2 = (\mu_o nI/a_2^2)(2e/m_{fj}V_{fj})^{\frac{1}{2}} \tag{29}$$

where μ_o is the magnetic permeability in vacuum, nI is the number of ampère turns (magnetic potential on the pole-shoe surface), and m_{fj} is the mass of the fragment ions under consideration.

Determination of k_i and l_{Qi}

It is possible to calculate - to a first approximation - the focusing action of the quadrupole lenses in our system

using eqs. (25) - (29). The agreement between calculated and experimentally found values of k_i for these relations appears to be better than 10%, within a certain range of lens strenghts [13]. For the design of the tandem mass spectrometer this accuracy has been sufficient. Greater accuracy, however, is necessary when the calculations are used for the adjustment of the instrument, as the resolution of the fragment mass spectrum is closely related to the accurate focusing of the ion beams.

To obtain higher accuracy it is necessary to take the fringe fields of the quadrupoles into account. In our instrument this is especially important because the quadrupoles are rather short compared with their bore radii. Moreover, all electric quadrupoles are short-circuited at both ends by stainless-steel apertures. This causes an additional disturbance of the electric field of the quadrupoles. Short quadrupole lenses generally give rise to values of k_i which are smaller than those calculated using eq. (27) [15].

In our system k_i and l_{Qi} have been derived experimentally for the electrostatic quadrupoles. This was done by measuring V_{Qi} at several adjustments of the other two electrostatic quadrupole lenses while keeping a sharp mass peak in the middle of the detector plane. A best fit of the experimental and calculated values of V_{Qi} could be obtained by applying a correction factor for k_i. For Q_1 and Q_3, which have similar dimensions, the same correction factor of 0.963 was found. For Q_4 a correction factor of 0.929 gave the best fit. Both corrections, indeed, result in a decrease of the lens strength as compared with the results given by Hawkes [15]. The adjustment of the magnetic quadrupole lens is not done quantitatively. No comparison between calculations and experiments was made. For the effective lens length l_{Qi} of Q_i we found the relation:

$$l_{Qi} = l_{Ri} + d_i \qquad (30)$$

with $i = 1,3$ or 4, where l_{Ri} is the length of the rods of Q_i, and d_i is the distance between the rods and apertures. Some of the results are demonstrated below.

Variation of the dispersion with Q_4

Behind the analyzing magnet is mounted an electrostatic quadrupole lens. A cross section of this quadrupole is shown in fig. 4. The distance a_4 in the median plane is chosen as 50 mm, which makes possible the simultaneous transmission of a mass range with a maximum mass ratio 1 : 4. Because the space in the y-direction is limited by the coils of the sector magnet the distance a_4^* is only 30 mm. The lens consists of 4 rods and 4 plates between the rods for fixing the zero potential. The rods have radii that approximately correspond to the equipotentials of a symmetric quadrupole field, and have the corresponding potentials.

The matrix formalism of Q_4 does not differ in principle from that given in eqs. (25) and (26). However, we have to consider the (de-)focusing action of this quadrupole in two respects.

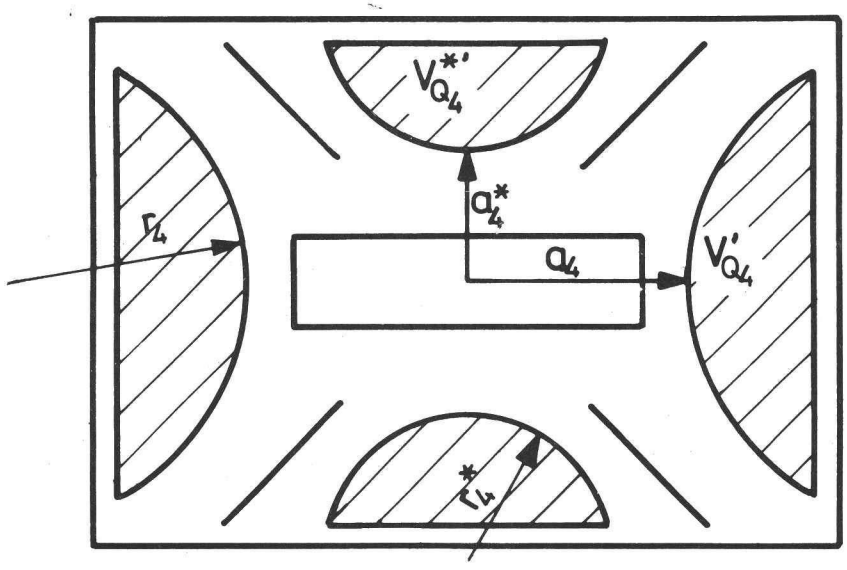

FIGURE 4

Cross section of Q_4. Owing to mechanical consideration the outside shape of this quadrupole lens is rectangular. The quadrupole rods have the appropriate radii of the equipotentials of symmetrical quadrupole lens: $r_4^* = 0.36\ r_4$, with corresponding potentials: $V^{*\prime}_{Q4} = 0.36\ V'_{Q4}$ (see eq. (37)). The four plates between the rods are built in to improve of zero potential fixation.

In the first place we are interested in the dispersion variation caused by the last quadrupole, for which only the main trajectories (reference z_i-axes) are considered. A simplified sketch of ion trajectories behind the analyzing magnet is depicted in fig. 5. Two situations are considered, viz. with Q_4 not in operation, and with Q_4 applied in the converging mode. In the first situation the intersections of the main trajectories of ions of mass m_{fo}, m_{f1} and m_{f2} with the detector plane are given by A, B and C respectively. When Q_4 is applied in the converging mode in the median plane, as demonstrated in fig. 5, the main trajectories are deflected towards the z-axis, giving the new intersections A', B' and C'. Because the intersection of a trajectory with the detector indicates the position of the mass peak, it follows from fig. 5 that the mass range on the detector has been increased.

In the second place it can be deduced from fig. 5 that a focusing action is present along each main trajectory itself. The original image positions F_o, F_1 and F_2 are focused alomg the z-, z_1- and z_2-axes towards the magnet. Both focusing actions can be determined from the matrix relation

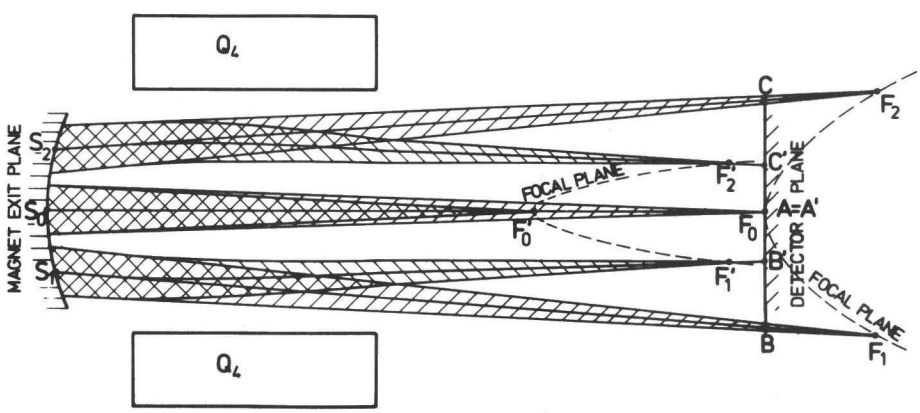

FIGURE 5

The double lens-action of Q_4. In this case, where Q_4 is operated in the focusing mode, the focal plane (indicated with primes) is moved towards the magnet and the dispersion is decreased.

$$X^{(CH)} = L_7 \cdot Q_4 \cdot L_6' \cdot \begin{bmatrix} (S_1)_x \\ S_1' \end{bmatrix} + W \cdot M \cdot X^{(IM)} \qquad (31)$$

in which $X^{(CH)}$ is the position vector on the channelplate detector and $X^{(IM)}$ is the position vector of an ion ray at the entry plane of the analyzing magnet. W is given by

$$W = \begin{pmatrix} 1/\cos(\phi_o - \phi_1) & 0 \\ 0 & 1 \end{pmatrix} \qquad (32)$$

Together with the vector $((S_1)_x, S_1')$ it performs the coordinate transformation behind the magnet to the frame of the main mass. Both vectors are measured with respect to the z-axis. L_6' is the driftlength matrix between the magnet and Q_4. The prime indicates that it has been corrected for the curvature of the magnet exit plane. For l_6' we can write

$$l_6' = l_6 - (S_1)_z \qquad (33)$$

Imaging

For one specific fragment-mass the relation between a position vector at the entry plane of the analyzing magnet and a vector at the detector can be given by eq. (31). Two results can be obtained from this equation.

(1) The position of the fragment mass peak on the detector plane. This can be found by calculating the intersection of the main trajectory for each fragment mass with the detector plane.

(2) The focus F_i of a beam of ions of mass m_{fi} can be calculated in the following way. The product matrix PM of all matrices from the collision cell up to and including Q_4 is calculated. Up to the image F_i a drift length matrix L_7' is defined. We can now write

$$A = L_7' \cdot PM \qquad (34)$$

The position of the focus is independent of the direction of the ion beam at the object. We can therefore obtain the drift length l_7' to the focus F_i by solving

$$A(1,2) = 0 \tag{35}$$

The image plane can be calculated by solving eq. (35) for several fragment masses.

The adjustment of an arbitrary quadrupole to obtain a sharp focus of an arbitrary fragment mass on the detector plane is obtained as follows. The product matrices B and C of all matrices respective in front of and behind the quadrupole Q_i in question are determined. From the matrix

$$D = C \cdot Q_i \cdot B \tag{36}$$

we may put

$$D(1,2) = 0 \tag{37}$$

resulting in a trigonometric relation in the parameter k_i, which is solved by iteration.

RESULTS

The algorithms described in the previous sections were implemented in an interactive FORTRAN computer program, executed on a PDP11/70 computer system. Initially matrix calculations were used for designing the tandem mass spectrometer, as has been demonstrated, for example, for the potential distribution of the post-acceleration section.

The matrix calculation method has been further developed towards higher accuracy. On the one hand such a development will lead to the optimization of the calculation method, which will be advantageous for designing future instruments. On the other hand the question can be answered whether the accuracy of the algorithm, with respect to the sharpness of the mass peaks, is sufficient to make possible automatic adjustment. Automation is necessary to enable fast measurements of CAD spectra of many compounds to be performed at various instrumental adjustments.

Imaging using three electrostatic quadrupole lenses Q_1 and Q_3

With two (or more) quadrupole lenses it is possible to create a lens system with independently adjustable lens strengths in the x- and y-directions. In this way it is possible to combine a sharp image on the detector (with respect to the x-direction) with optimum transmission through the pole-shoe gap of the analyzing magnet. In the measurements discussed below, the potential distribution over the electrodes of the post-acceleration section is assumed constant.

For practical reasons the fragment ions are made to experience a constant accelerating force between the first and the last electrode of the post-acceleration section. As the housing of the second stage was kept at ground potential during the experiments described, the voltages of the quadrupoles are measured with respect to ground potential. So we define

$$V'_{Qi} = V_{Qi} - V_{PA} \tag{38}$$

with i = 1, 3 or 4.

The parameter that was frequently used in our first experiments was the post-acceleration voltage V'_{PA}, defined as

$$V'_{PA} = V_{PA} - V_p \tag{39}$$

The actual amount of energy obtained by fragment ions during post-acceleration is thus eV'_{PA}.

In a first series of measurements we determined the relation between V'_{Q3} and the total energy of a beam of ^{20}Ne ions when a sharp mass peak was present at the centre of the detector. The initial energy of the ions (eV_p) was kept constant at 2 keV. In Fig. 6, V'_{Q3} is plotted against the total ion energy after post-acceleration. The measurements were performed at several adjustments of Q_1, which was operated in the defocusing mode. In the figure the solid lines represent the calculated values. For $V_{Q1} = 0$ V two lines are depicted from which the small focusing effect of the post-acceleration in the median plane can be seen. The dotted line gives the calculated values of V'_{Q3},

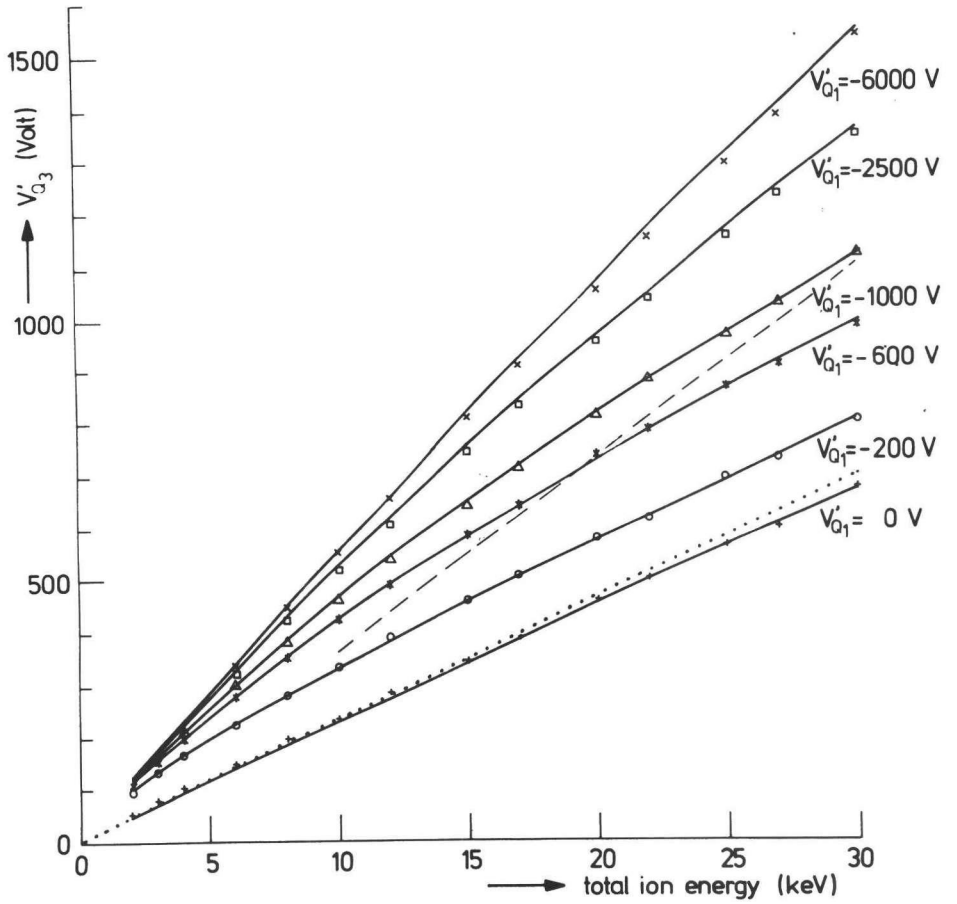

FIGURE 6

Adjustment of V'_{Q3} as a function of the total ion energy of a ^{20}Ne ion beam, to obtain a sharp mass peak at the centre of the detector, for a fixed pre-acceleration energy of 2 keV. The relation is given for several values of V'_{Q1}, which is here used in the defocusing mode in the median plane. The solid lines represent the results obtained with our matrix algorithm, the measurements are indicated by the symbols.

when the total energy consists exclusively of pre-acceleration energy and no focusing occurs in the post-acceleration section. The dashed line in fig. 6 represents the adjustments for which the maximum transmission was obtained. The increase of transmission is a result of the focusing effect in the y-direction which occurs when Q_1 is used in the defocusing mode in the median plane. This defocusing action of Q_1 in the median plane results in a decrease in the linear magnification of the object slit on the detector, as shown in Table 2. When the linear

TABLE 2

Calculated linear and angular magnifications, imaging the collision-cell exit slit on the detector plane (calculations for a ^{20}Ne ion beam with a pre-acceleration energy of 2 keV).

V'_{PA} (kV)	Magnification					
	$V'_{Q1} = 0$ V		$V'_{Q1} = -600$ V		$V'_{Q1} = -2500$ V	
	lin.	ang.	lin.	ang.	lin.	ang.
8	0.43	1.01	0.17	2.53	0.05	8.73
15	0.41	0.81	0.22	1.52	0.08	4.11
25	0.39	0.67	0.25	1.04	0.11	2.31

magnification decreases, better resolution can be obtained, as the peak width also decreases. From Table 2, however, it can also be deduced that the *angular* magnification increases. This results in an increase in the dimensions of the ion beam and thus in an increase of the peak width as a result of aberration and diminished depth of focus. During the measurements it was observed that the narrowest peaks are obtained when $V'_{Q1} \geq -600$ V.

The relation and the peak width are also considerably influenced by the post-acceleration voltage V'_{PA}. Tuithof [16] demonstrated how both the relative energy and the angular spread occurring at fragmentation are decreased by post-acceleration of the fragment ions. Under experimental conditions, therefore, V'_{PA} is generally chosen larger than 10 kV.

Within the range of practical values for V'_{Q1} and V'_{PA}, as described above, there is very good agreement between the measured and calculated values for V'_{Q3}, as demonstrated in fig. 6. The small deviations correspond to an average relative difference in peak width of only 3% between the calculated and measured adjustments of Q_3.

Q_3 and Q_4

The electrostatic quadrupole lens Q_4 situated behind the analyzing magnet is able to vary the dispersion caused by the magnet. The dispersion can be increased by applying a negative potential to the quadrupole rods in the median plane. If a positive potential is applied, the dispersion decreases. The possibility of dispersion variation is introduced into the system because of the limited spatial resolution of the detection system. The loss of resolution in the detection system forms a considerable contribution to the ultimate peak width. When, however, a smaller mass range is simultaneously detected, this resolution becomes less important, as the peak separation increases. Increase of the dispersion, therefore, generally results in high mass resolution. Because of the smaller mass range that is simultaneously detected, however, increased dispersion is accompanied by loss of ions of non-recorded masses. On the other hand it is possible to acquire a higher sensitivity at the cost of mass resolution by using Q_4 in the focusing mode.

It was demonstrated above that the dispersion variation caused by Q_4 is accompanied by translation of the mass focal plane (fig. 4). Therefore, Q_4 is always used in combination with Q_3. The relation between the adjustments of these two, simultaneously used quadrupole lenses is depicted in fig. 7, which shows the lens parameter k_3 of Q_3 measured and calculated as a function of k_4. The condition for the adjustments was to obtain a sharp mass peak at the centre of the detector plane. The results are derived for a beam of ^{20}Ne ions having a pre-acceleration energy of 2 keV. To cover a wider range of measurements the actual parameter varied is the post-acceleration energy. The related variation of k_4 can be deduced from eq. (27). It should be noted that a small focusing action is present, caused by the post-acceleration section. It increases with the post-acceleration energy.

The compensation by Q_3 for the translation of the image plane caused by Q_4 can be clearly seen from fig. 7. At increasing defocusing action of Q_4 ($V'_{Q4} = -6500$ V), an increasing focusing action of Q_3 is apparent. Focusing by Q_4 ($V'_{Q4} = 6500$ V)

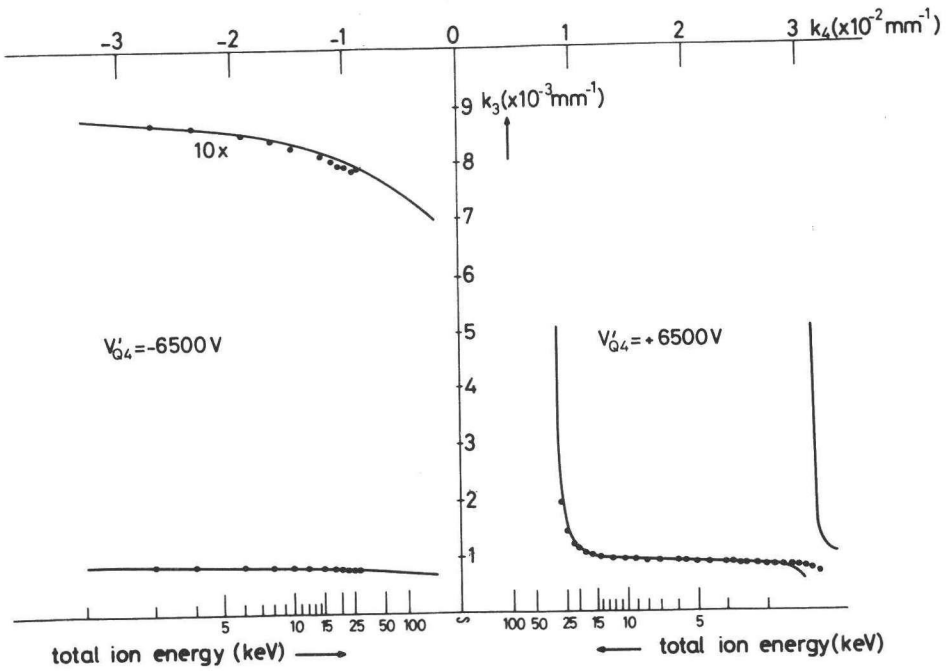

FIGURE 7

Relation between the adjustments of Q_4 and Q_3 to obtain a sharp mass peak at the centre of the detector, for a ^{20}Ne ion beam with a fixed pre-acceleration energy of 2 keV. For $V'_{Q4} = -6500$ V, Q_4 is used in the defocusing mode, which results in an increase of the dispersion. For $V'_{Q4} = +6500$ V, the dispersion decreases.

is accompanied by a smaller focusing action of Q_3. When $k_4 \gtrsim 80 \times 10^{-4}$ mm^{-1}, periodicity of k_4 occurs. This can be explained by the oscillatory motion of the ions inside Q_4. For strong focusing action an additional focus is present inside the last quadrupole lens, apart from the focus on the detector. In fig. 7 this part of the diagram shows only calculated results. However, the periodicity is also observed experimentally, though no quantitative results are available. The quadrupole adjustments in this part of the diagram are characterized by extremely low intensities (diverging action of Q_4 in the y-direction) and very critical adjustments.

With respect to the accuracy of the calculations compared with the experimental results, only a restricted range of adjustments of the doublet $Q_3 - Q_4$ is of practical significance. Also here, the post-acceleration energy is generally chosen larger than 8 keV.

When Q_4 is operated in the diverging mode the peak broadening due to adjustment of Q_3, according to the calculated results, varies from ~ 10% at a total energy of 8 keV to ~ 2% at 25 keV. For positive values of k_4 the peak broadening is smaller than 1% for all measurements in fig. 7, within the practical range of adjustments.

The image plane and simultaneous detection

After the fragment ions have been mass-analyzed by the sector magnet they are finally detected by a flat channelplate (CEMA). The detector is positioned perpendicular to the z-axis behind the analyzing magnet (see fig. 3). In this way maximum gain of the detector can be obtained and also the maximum range of simultaneously detectable masses at a channelplate diameter of 75 mm.

The position and shape of the mass focal plane with respect to the flat detector plane are highly important for obtaining optimum mass resolution over the complete mass range that is simultaneously detected. Generally speaking, a sector magnet gives rise to an image plane which is both curved and oblique with regard to the optical axis. This is also the case in our tandem mass spectrometer, as is demonstrated in fig. 8, where the image planes calculated by our computer model of the instrument are shown. The calculations were performed for several adjustments of the instrument and for variations of several parameters. Together with the focal planes we calculated the linear and angular magnifications of the images. They are respectively equal to A(1,1) and A(2,2), where A is the product transfer matrix defined in eq. (34). These two values are of importance with respect to the image width and the depth of focus, and thus for the ultimate peak width on the detector.

The behaviour of the mass focal plane can be conveniently explored using the computer model. One of the most important tools for the manipulation of this plane is the magnetic quadrupole lens. Operation of Q_2 in the diverging mode produces a counter-clockwise rotation of the image plane (fig. 8(a)).

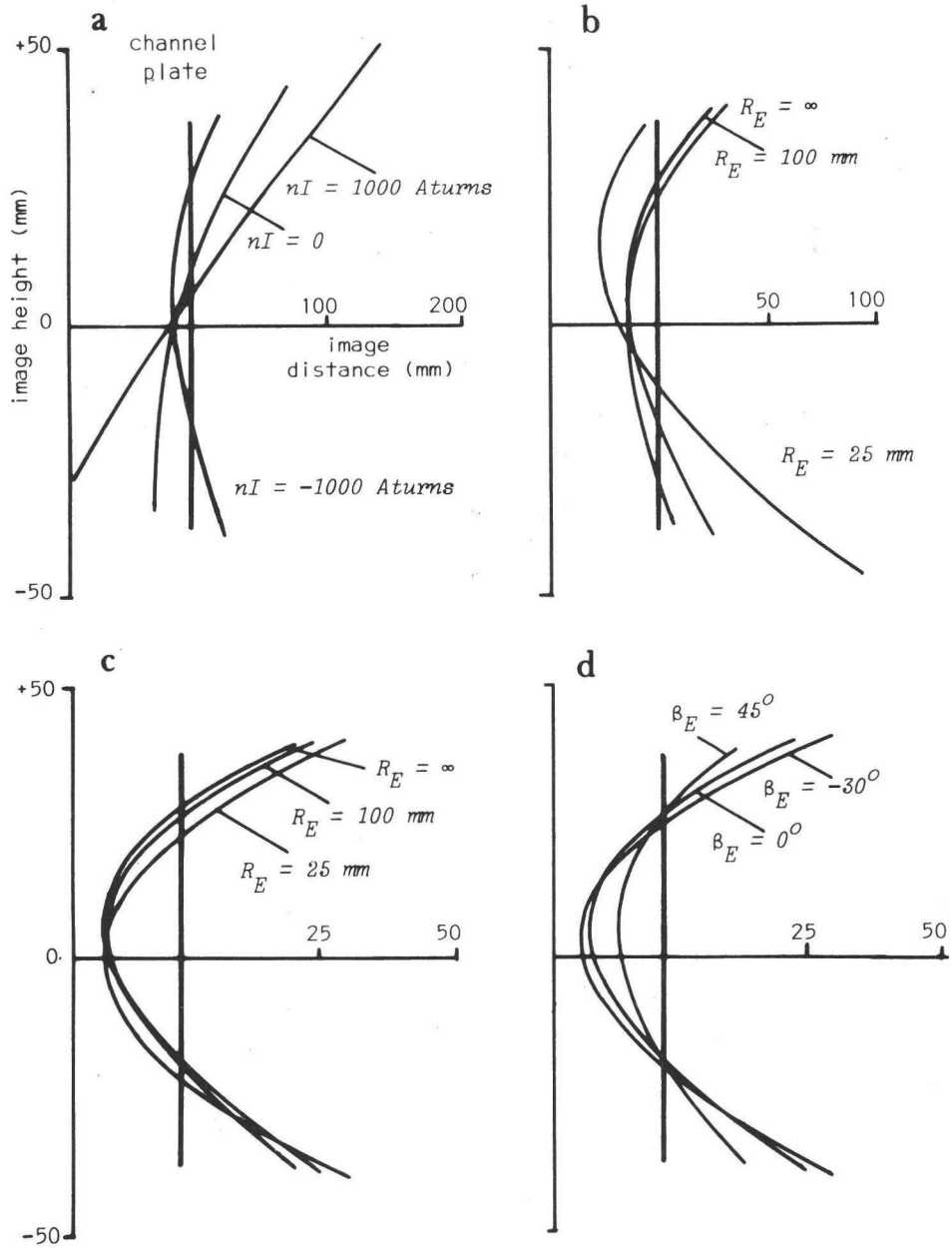

FIGURE 8

Calculated shape and position of the mass focal plane of the tandem mass spectrometer at various values of several parameters of the instrument. For the calculations we used $m_p = 120$, $V_p = 4$ kV and $m_{f0} = 59$. Default values are $V'_{PA} = 15$ kV, $V'_{Q1} = 0$ V, $V'_{Q4} = 0$ V, $R_E = 100$ mm and $\beta_E = 0^o$. Abscissae, image distance with respect to the front side of the channelplate; ordinates; image height with respect to the main ion optical axis.

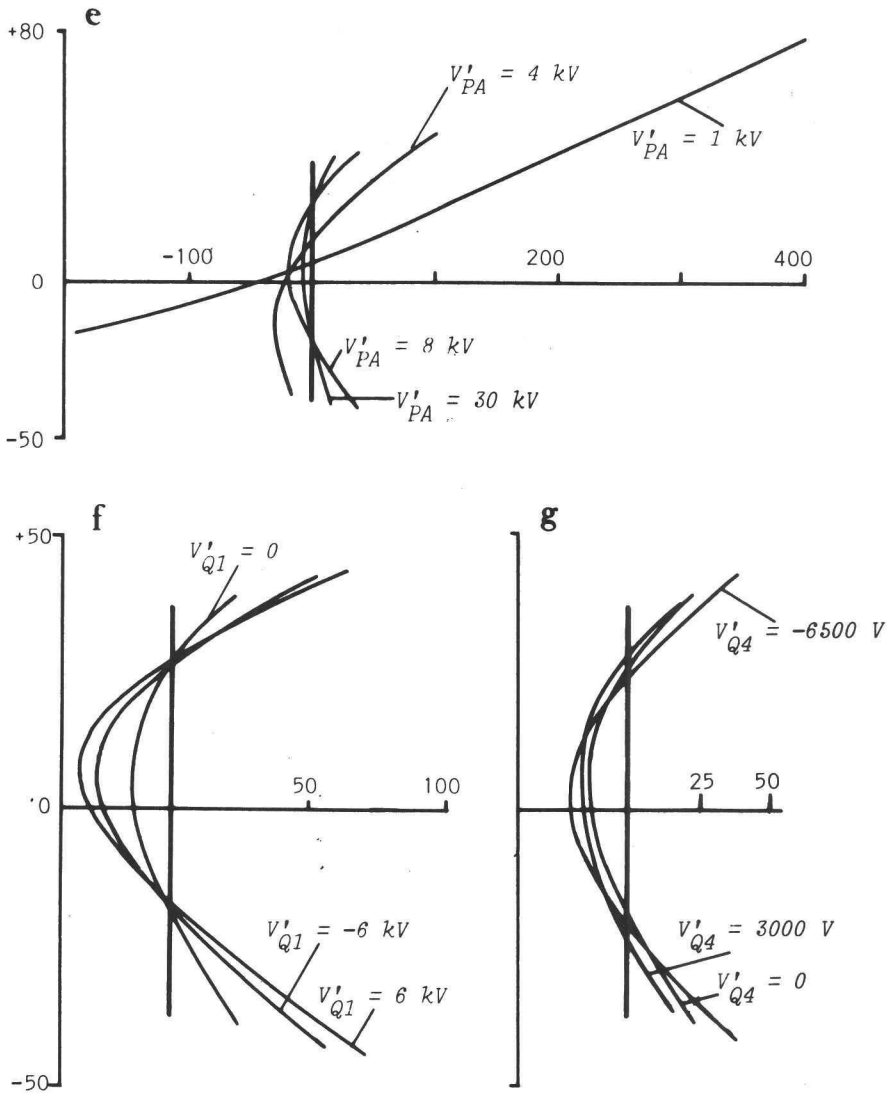

FIGURE 8 (continued)

The best rotational position, for the default conditions used in fig. 8(a), is reached at nI = -1000 ampère turns.

The rotation of the focal plane originating from the curvature of the exit plane of the magnet is demonstrated in fig. 8(b). The three image planes shown in this figure are calculated at the same adjustment of Q_2, i.e. nI = -1000 ampère turns. A curved exit plane of the analyzing magnet can considerably reduce the lens strength of Q_2 necessary for optimal rotation. This is clearly demonstrated in fig. 8(c). For a flat exit plane, we calculate for Q_2 that nI = -1365 ampère turns. For a radius of curvature R_E of the exit plane of 25 mm, we calculate nI = -127 ampère turns. From fig. 8(c) we also conclude that the curvature of the image plane is only slightly influenced by R_E.

In fig. 8(d) it is demonstrated that a flatter image plane can be obtained by increasing the exit angle β_E. This is, however, accompanied by a clockwise rotation of the plane. At $\beta_E = -30^o$ and $\beta_E = +45^o$, we calculate respectively nI = -550 ampère turns and nI = -1215 ampère turns.

The post-acceleration voltage V'_{PA} considerably flattens the image plane (see fig. 8(e)). It also causes a counter-clockwise rotation of the focal plane. At V'_{PA} = 30 kV and 4 kV, we calculate, for the situation in fig. 8(e), nI = -353 ampère turns and nI = -5000 ampère turns, respectively. At small values of V'_{PA} it is no longer possible to rotate the focal plane into a good position by using Q_2. In fig. 8(e) this is the case for V'_{PA} = 1 kV. At this low post-acceleration energy the fragment ions can be considered to have nearly identical velocities. In that situation the electrostatic quadrupole Q_3 has a mass dependence which is comparable with that of Q_2. So Q_3 cannot be used in that case for the back-translation of the focal plane without causing a large clockwise rotation.

When Q_1 or Q_4 are used, the angular and linear magnifications are two important factors concerning the curvature of the image plane. When these two lenses are not in operation the angular and linear magnifications are respectively -0.9 and -0.4 at the default adjustment used in fig. 8. When Q_1 is used (fig. 8(f)), we first of all see an increase of the curvature of the focal plane. In connection with this, the angular

magnification increases to -15.9, resulting in a considerable loss of depth of focus. The linear magnification becomes -0.02. For Q_4 we also observe a small additional bending of the focal plane when this lens is used in the defocusing mode (see fig. 8(g)). The angular and linear magnifications at $V'_{Q4} = -6500$ V are respectively -0.3 and -1.2. The flattening of the image plane when Q_4 is used in the focusing mode is accompanied by a marked increase of angular magnification to -7.4 and a decrease of the linear magnification to 0.05.

From the previous remarks it will be clear that the mass resolution of the fragment spectrum is highly influenced by the operation of both Q_1 and Q_4. When Q_1 is used to increase the ion transmission in the direction perpendicular to the median plane, the resulting decrease in resolution must also be considered. The same argument holds for Q_4 when it is operated to change the mass dispersion. This demonstrates the complexity of the optimization procedure for the four quadrupoles, and that each adjustment of the instrument is in fact a compromise.

REFERENCES

[1] K. Levsen, Progress in Mass Spectrometry, Vol.4, Verlag Chemie Weinheim, New York, 1978, pg. 138 and 199.

[2] R.G. Cooks, Int.Lab., (Jan./Feb.1979) pg. 79.

[3] R.G. Cooks, J.H. Beynon, R.M. Caprioli and G.R. Lester, Metastable Ions, Elsevier, Amsterdam, 1973.

[4] A.P. Bruins, K.R. Jennings and S. Evans, Int.J.Mass Spectrom.Ion Phys., 26 (1978) 395.

[5] T. Wachs, C.C. van de Sande, P.F. Bente III, P.P. Dymerski and F.W. McLafferty, Int.J.Mass Spectrom.Ion Phys., 23 (1977) 21.

[6] P.J. Todd, Thesis, Cornell University, Ithaca, N.Y. 1980.

[7] R.P. Morgan, J.H. Beynon, R.H. Bateman and B.N. Green, Int.J.Mass Spectrom.Ion Phys., 28 (1978) 171.

[8] R.A. Yost, C.G. Enke, Anal.Chem., 51 (1979) 1251 A.

[9] G.J. Louter, A.J.H. Boerboom, P.F.M. Stalmeier, H.H. Tuithof and J. Kistemaker, Int.J.Mass Spectrom.Ion Phys., 33 (1980) 335.

[10] H.L.C. Meuzelaar, J. Haverkamp and F.D. Hileman, Curie-Point Mass Spectrometry of Biomaterials: Compendium and Atlas, Elsevier, Amsterdam, 1980.

[11] P.G. Kistemaker, A.J.H. Boerboom and H.L.C. Meuzelaar, in D. Price and J.F.J. Todd (Eds.), Dynamic Mass Spectrometry, Vol.4, London, 1975, Chap.9; A.J.H. Boerboom, P.G. Kistemaker, M.A. Posthumus and H.L.C. Meuzelaar, in D. Price and J.F.J. Todd (Eds.), Dynamic Mass Spectrometry, Vol.5, Heyden, London, 1978, Chap.9.

[12] A.P. Banford, The Transport of Charged Particle Beams, E. and F.N. Spon Ltd., London, 1966.

[13] H.H. Tuithof and A.J.H. Boerboom, Int.J.Mass Spectrom.Ion Phys., 20 (1976) 107.

[14] A.J.H. Boerboom, Adv.Mass Spectrom., 5 (1971) 269.

[15] P.W. Hawkes, Adv.Electron.Electron Phys., Suppl. 7, (1970)

[16] H.H. Tuithof, Int.J.Mass Spectrom.Ion Phys., 23 (1977) 147.

[17] H.H. Tuithof, Thesis, TH-Delft, Holland, 1977.

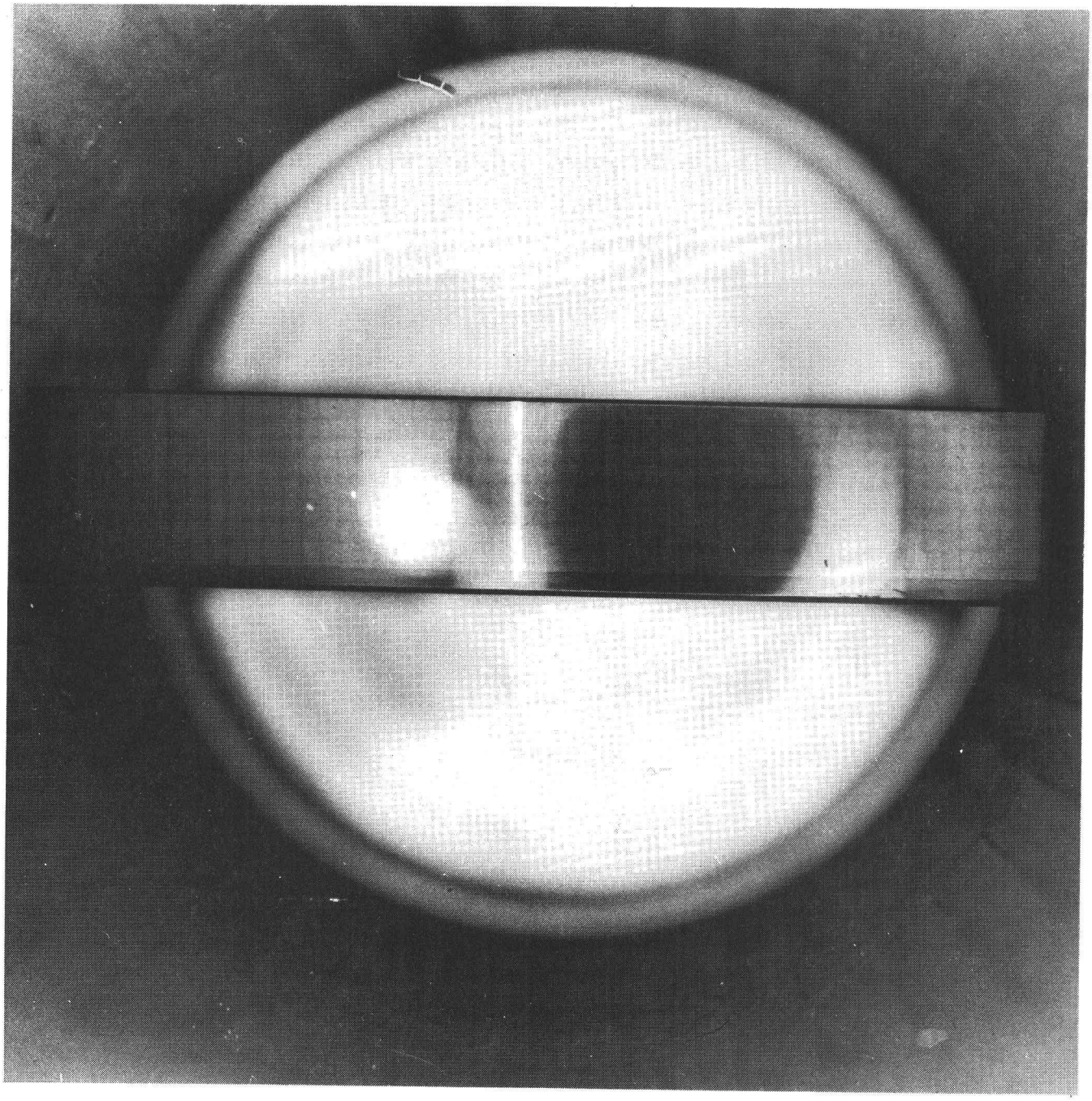

Photograph of one mass peak as it can actually be observed on the fibre optics at the rear end of the instrument.

C H A P T E R 3

APPLICATION OF MATRIX CALCULATION II: MASS SCALING OF CAD-FRAGMENT SPECTRA

ABSTRACT

Two calibration methods of fragment mass spectra, derived with CAD in a tandem MS, are discussed here. The instrument has a variable dispersion and is equipped with an electro-optical, simultaneous detection system. Without dispersion variation the masses of the fragment ions can be calculated by applying merely one calibration function. This function relates, at any value of the magnetic field of the mass analyzer, the momentum of a fragment to its position on the detector.

The dispersion can be changed by means of an electrostatic quadrupole lens, behind the sector magnet, which acts upon the energy of the fragment ions. A calculation method is introduced here, which opens the possibility of nominal mass scaling without needing a calibrant, even when the instrument is operated with varied dispersion. The method is based upon the representation of the ion-optical devices of the instrument by transfer matrices. Both mass scaling procedures discussed here can be used for nominal mass assignment up to about m/z 1000.

Attention has been given to the influence of the kinetic energy lost upon collision on the shift of peaks in the CAD-mass spectrum.

INTRODUCTION

One of the first requirements of every mass spectrometer is to obtain a calibration of the masses. In the determination of a nominal mass scale in most cases a variable is used, which is directly correlated with the mass. In a scanning magnetic sector mass spectrometer this can be the voltage of a Hall probe, in a quadrupole mass spectrometer the rod DC-voltage is used as a measure for the mass. In both cases the mass scale is calibrated against a well known starting peak of a calibrant. In an instrument with a photo-plate detection system the position of a mass peak on the detector is the variable correlated with the mass. When the relation between mass and correlated variable is less simply described, complete calibration spectra can be used. Unknown masses are then found by extrapolation from or interpolation between calibrant peaks.

The second stage of our tandem mass spectrometer for Collision Activated Dissociation (CAD) experiments is a sector magnet type instrument with an electro-optical simultaneous

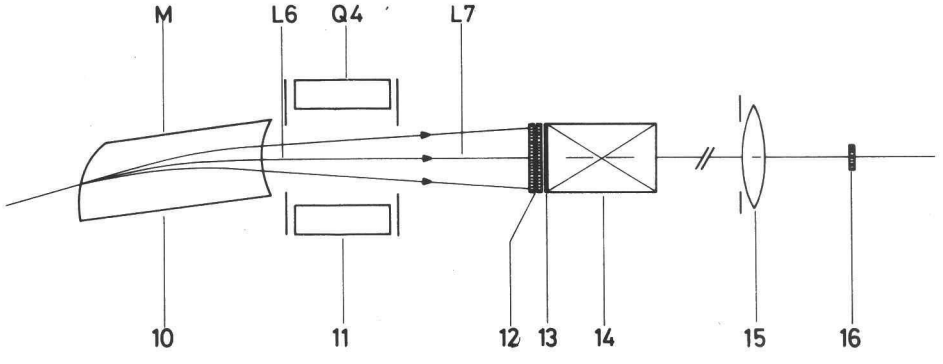

FIGURE 1

Simplified top view of the mass analyzing part of the second stage of the tandem MS. Above the instrument are indicated the names of the transfer matrices, used in this paper.
10 - Analyzing magnet; 11 - electrostatic quadrupole lens; 12 - chevron channel electron multiplier combination (channel-plates); 13 - phosphor coating with aluminium top layer; 14 - fibre optics slab; 15 - aspherical camera objective; f/D = 1.2, f = 85; 16 - 1024 channel photo-diode array.

detection system. It has been described by Louter et al. [1-4]. In figure 1 that part of the second stage is depicted where the mass dispersion and the detection take place. Behind the sector magnet an electrostatic quadrupole lens Q_4 is situated, which is used to increase or decrease the dispersion produced by the magnet.

Concerning the mass calibration of the second stage, the position of fragment peaks on the detector is the variable correlated with their masses. Moreover, every position $x_i^{(D)}$ on the detector is uniquely related to the corresponding radius of curvature R_{fi} of the trajectory of an arbitrary fragment ion with mass m_{fi} through the magnet, if Q_4 is not in operation.

$$R_{fi} = f(x_i^{(D)}) \qquad (1)$$

Once the function f in (1) is known, the momentum p_{fi}, and thus the mass m_{fi}, corresponding to a position $x_i^{(D)}$ can be calculated by solving

$$p_{fi} = R_{fi} \cdot B \cdot e \qquad (2)$$

where B is the magnetic field of the analyzing magnet. f can be calibrated by using the spectrum of a calibrant as e.g. perfluorokerosene (PFK).

Though this method has proven to produce sufficiently accurate mass scales for the second stage, it cannot be applied when Q_4 is used. As an electrostatic quadrupole lens acts upon the energy of the fragments, the position $x_i^{(D)}$ is also determined by the energy, which itself is a function of the mass of the fragments. There no longer exists one unique functional relation like (1). For each precursor ion a special function f has to be calibrated.

To avoid the problem of needing a library of CAD-fragment spectra of many precursor ion masses, we developed a computer program for the mass scaling. This method is based upon the representation of the ion-optical devices by transfer matrices.

In [4] it has already been demonstrated that such a representation can be a strong tool in the design and automatic tuning of a mass spectrometer. In this paper the more general applicability of the approach is further demonstrated. The method is used here for the calculation of accurate mass scales of CAD-spectra. The same nomenclature for variables and parameters as in [4] will be used here. To [4] will be referred as I.

METHOD

The way in which the optics of an instrument can be represented in one plane by simple 2-dimensional transfer matrices, and the ion trajectories by position vectors, has already been discussed in I. It is demonstrated there that the position vector $X_i^{(CH)}$ of a fragment mass m_{fi} on the channelplate detector (see fig. 1) can be related to the vector $X^{(CC)}$ at the position of the exit slit of the collision cell according to

$$X_i^{(CH)} = L_7 \cdot Q_4 \cdot L_6' \cdot \{S_i + W \cdot M \cdot T \cdot X^{(CC)}\} \qquad (3)$$

where T is the product matrix of all transfer matrices from the entry plane of the magnet up to the collision cell and S_i is the position vector at the magnet exit plane, of the main trajectory of mass m_{fi}. For mass scaling purposes we are only interested in the top of the mass peak. So consider those ions which leave the collision cell along the ion-optical axis. Then (3) reduces to

$$X_i^{(CH)} = L_7 \cdot Q_4 \cdot L_6' \cdot S_i \qquad (4)$$

From I, (1) and (4) we can find the position $x_i^{(CH)}$ on the channelplate, which corresponds to the position $x_i^{(D)}$ on the photodiode array. The construction of the electro-optical detection system has been depicted in figure 1. More detailed information is given by Boerboom et al. [5].

The relation between $x_i^{(D)}$ and $x_i^{(CH)}$ is given by

$$x_i^{(D)} = x_m^{(D)} + Kx_i^{(CH)} \qquad (5)$$

where $x_i^{(CH)} = 0$ corresponds to the intersection of the ion-optical axis with the channelplate. $x_i^{(D)}$ and $x_m^{(D)}$ are both expressed in channel numbers of the photodiode array. K is related to the linear magnification of the light-optical system.

Relations (4) and (5) are the basic equations, used for the mass assignment of the fragment spectra in our instrument.

RESULTS

The polynomial approach

The function f in relation (1) has been determined for our instrument to provide for a CAD-mass calibration when Q_4 is inoperative. For this purpose we have recorded the CAD-spectrum of mass m/z 655 from PFK. We used 51 reference peaks, regularly distributed in the fragment mass range from m/z 155 to m/z 605. A continuous approximation of f was then obtained by a least square fit of a fifth order polynomial through the momenta, corresponding to these reference peaks With this polynomial approach we achieve a mass assignment accuracy better than $|10^{-3}|$ (relative mass deviation). This value corresponds to the usual experimental error caused by the peak position assignment, which appears to be the most important limitation on the mass assignment accuracy.

The transfer matrix approach

When CAD-spectra are recorded with a changed mass dispersion, the polynomial method cannot be used for mass scaling. Therefore, we developed another mass calibration method, based upon the transfer matrix representation of our tandem mass

spectrometer, discussed in I. It was pointed out there that the theoretical values of the parameters, used to describe the ion-optical properties of a device, may differ from the values derived experimentally. Deviations may, for example, be caused by misalignment of the instrument or by fringing field effects. Also for the mass scaling calculation it is necessary to optimize some of the parameters, in order to obtain sufficient accuracy of the mass assignment.

By measuring and calculating the mass scale, when Q_4 is not in operation, we have determined the empirical value of the sector angle ϕ_o of the magnet to be 15.37^o (actual value 15^o). With this best value of ϕ_o there still remains a slight deviation between the measured and calculated masses. In figure 2 this deviation is given by the solid line. Plotted is the mean difference between the measured and the calculated mass positions (expressed in channels) versus the position of the mass on the detector. Similar deviations are found when

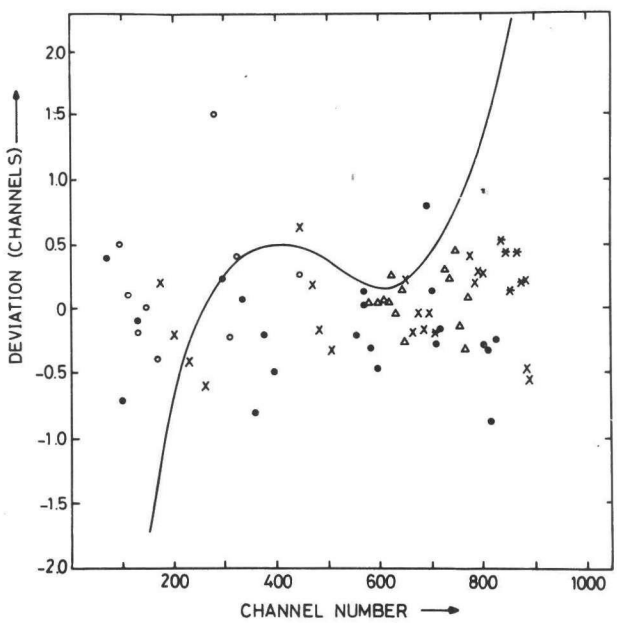

FIGURE 2

Deviation in the mass assignment, expressed as number of channels, when the transfer matrix method is used. Plotted is the difference between the calculated and the measured positions of a mass. The calibrant is benzonitrile m/z 103, $V_P = 3$ kV, $V'_{PA} = 15$ kV. Q_4 is not operated.
When the proportionality factor K in relation (5) is assumed constant, the average value of the deviations would be given by the solid curve.

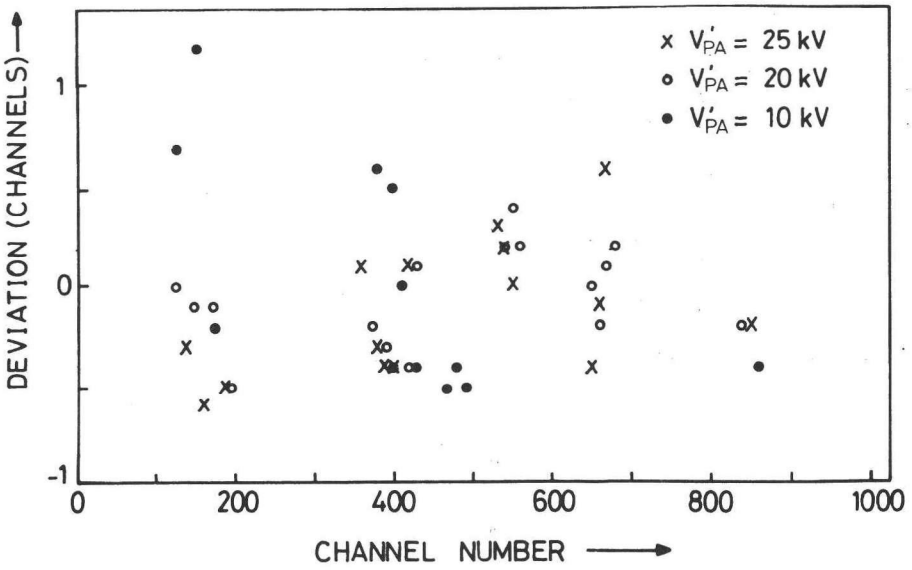

FIGURE 3

Mass assignment deviation when the transfer matrix method is applied, at several values of the post-acceleration voltage V'_{PA}. All experimental conditions are as mentioned in figure 2.

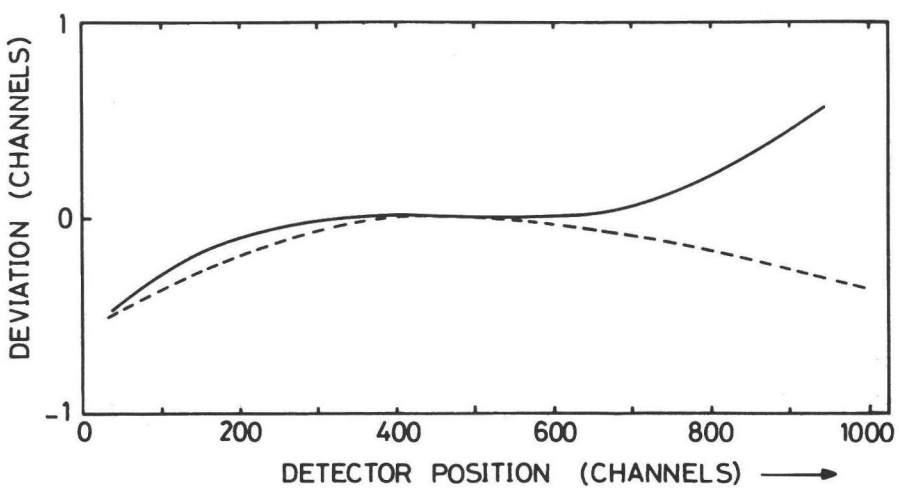

FIGURE 4

Dashed line: difference between the mass positions calculated with and without fringing field correction of the magnet $V_P/V'_{PA} = 0.2$. Solid line: difference between the mass position assignments calculated using the field number k_4 of Q_4 and with the more accurate value k_{c4}. $V'_{Q4} = -6.5$ kV, $V_P = 3$ kV, $V'_{PA} = 20$ kV and the precursor mass is m/z 103.

Q_4 is operated, suggesting that the deviations are due to distortion of the mass spectrum by the camera objective. This distortion has been corrected for by calibrating the proportionality factor K in relation (5) as a function of the channel number. The symbols in figure 2 correspond to the mass assignment errors, determined in 5 CAD-spectra, using the calibrated value of K. These spectra have been recorded at $V_P = 3$ kV and $V'_{PA} = 15$ kV. The mass range, expressed as the ratio of the maximum and minimum masses which are simultaneously detected, is 3.8.

In figure 3 the mass assignment errors of 3 CAD-spectra have been plotted, recorded at a post-acceleration voltage V'_{PA} of 10 kV, 20 kV and 25 kV respectively, and at a source potential V_P of 3 kV. The mass range varies from 3.6 at 10 kV through 3.9 at 20 kV to 4.0 at 25 kV post-acceleration voltage. Both figures 2 and 3 demonstrate that the transfer matrix method results in a mass assignment error which is comparable with that of the polynomial method, and which lies very well within the experimental error of about $\pm$ 0.5 channel.

Some attention has been given to the influence of fringing fields of the magnet upon the accuracy of the mass scaling calculations. For this purpose we applied a fringing field model as proposed by Nier and as described in detail by Kerwin [6]. The deviation between the mass scale calculations with and without fringing field correction (but with adapted values for R_o, R_E and ϕ_o) is demonstrated in figure 4. In this figure the dashed line is the calculated difference between the mass assignment without and with correction. Though from figure 4 it follows that a small difference occurs, we could find no significant improvement in the mass assignment calculated with fringing field correction.

Mass scaling with changed dispersion

Under normal experimental conditions and without operation of Q_4, the mass resolution of the second stage can be up to about 100 (10% valley) at a mass range of 4. This mass resolution, however, is mainly limited by the spatial resolution

of the detection system and by the limited number of channels (photodiodes) available for a simultaneously detected spectrum. Q_4 is used to increase the mass resolution by increasing the dispersion. This higher mass resolution is accompanied by a smaller mass range, and so by a loss of signal. On the other hand the mass range can be increased, at the cost of the mass resolution, by decreasing the dispersion. In table 1 three examples for different dispersions are given. Apart from the mass range also the minimal and maximal relative mass distances per channel, determining the mass resolution, are given.

TABLE 1

V'_{Q4} (kV)	k_{c4} (mm^{-1})	mass range	relative mass distance per channel	
			min.	max.
+1.0	$+4.2 \times 10^{-3}$	5.7	1.4×10^{-3}	2.6×10^{-3}
-3.0	-7.2×10^{-3}	2.4	8.0×10^{-4}	1.2×10^{-3}
-6.5	-1.1×10^{-2}	1.8	5.8×10^{-4}	7.8×10^{-4}

TABLE 1

Relative mass distance corresponding to one channel of the detector and the ratio of highest and lowest simultaneously detected masses, when the dispersion is varied. k_{c4} is given for the precursor m/z 103. Precursor energy: 3 keV; post-acceleration energy 20 keV.

The lens strength parameter k_4 of Q_4, as defined in I, is a measure of the lens strength of the quadrupole. Because of the cross-section of the ion beam leaving the analyzing magnet, we have used here an expression for k_4 different from that given in I (27). This corrected value k_{c4} is given by the relation

$$k_{c4}^2 = \frac{k_4^2 \ (1 + x'^2_{Q4})}{1 - x_{Q4}^2 k_4^2} \qquad (6)$$

where x_{Q4} and x'_{Q4} are respectively the position and slope of the corresponding ion ray, at the entrance plane of Q_4. Relation (6) is a consequence of applying the exact solution of the equation of motion in an electric quadrupole field, as has been described in more detail by Boerboom et al. [7]. In figure 4 we demonstrate the calculated deviation between a mass scale obtained with k_{c4} and a scale obtained with k_4 (solid line), at $k_{c4} = -1.2 \times 10^{-2}$ mm^{-1}.

In figure 5 the mass assignment accuracy is demonstrated, for the case where the mass scale is calculated for various

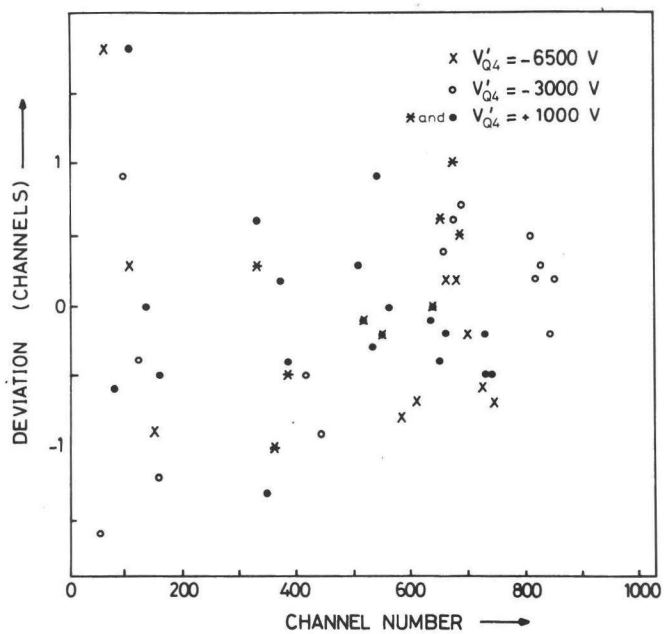

FIGURE 5

Accuracy of the transfer matrix method when Q_4 is applied. The calibrant is benzonitrile m/z 103, $V_P = 3$ kV, $V'_{PA} = 20$ kV.

dispersions. Under the same experimental conditions as mentioned in table 1 we have determined the mass assignment error for four CAD-spectra. Plotted are the differences between corresponding measured and calculated mass positions. The error is given in numbers of channels, the corresponding relative mass assignment error can be deduced from the relative mass distances per channel given in table 1. The mean mass assignment error has been minimized by variation of the parameters k_{c4} and ℓ_{Q4}, where

ℓ_{Q4} is the effective lens length. The best values for k_{c4} and ℓ_{Q4} with respect to mass scaling correspond with the values found in I on the basis of the focusing action of Q_4 on one mass (the adjustment of one sharp mass peak on the detector).

Obviously the spread in the measurements in figure 5 is larger than when Q_4 is inoperative. In the case of increased dispersion, however, it should be noted that peakbroadening occurs, which increases the error in the position assignment of a peak. This broadening is mainly due to the Kinetic Energy Release (KER) at fragmentation. In this figure at $V'_{Q4} = -6.5$ kV a KER of 0.1 eV causes a maximum broadening of about 2 channels.

Kinetic energy loss and mass assignment

On collision part of the translational energy E_p of the precursor ion is converted into internal energy Q. If the mass of the target molecule is small compared with that of the precursor ion, the relative energy shift of a fragment ion is given by [8]

$$\frac{\Delta E_f}{E_f} = \frac{Q}{E_p} \qquad (7)$$

The energy loss results in a shift of the peak towards lower masses. Generally this effect will be small, as, under our experimental conditions, the most probable energy transfer at collision will be of the order of 1 eV. However, some fragmentation reactions show values of Q which amount up to 20 eV [9,10]. Also in our measurements we have found energy losses of the same order of magnitude for fragments m/z 181 and m/z 281 of the precursor m/z 381 of PFK. Such high values of Q can cause considerable peak shifts, especially of high fragment masses, and so handicap the interpretation of unknown CAD-spectra.

By application of both a high post-acceleration and a momentum analyzer, peak shifts are much smaller in our tandem instrument than in conventional mass spectrometers for high energy CAD. Under normal experimental conditions the relative mass shift

of a peak, due to energy loss of 10 eV, is smaller than 2×10^{-4}. For conventional instruments this value is about one order of magnitude larger. The tandem mass spectrometer combines high mass assignment accuracy and high mass resolution [1] in high energy CAD-spectra. This unique combination makes the instrument very suitable for the analysis of (mixtures of) compounds, also with higher molecular weights and large kinetic energy losses on collision.

REFERENCES

[1] G.J. Louter, A.J.H. Boerboom, P.F.M. Stalmeier, H.H. Tuidhof and J. Kistemaker, Int.J.Mass Spectrom.Ion Phys., 33 (1980) 335.

[2] G.J. Louter, P.F.M. Stalmeier, A.J.H. Boerboom, J. Haverkamp and J. Kistemaker, Z.Naturforschung 35c (1980) 6.

[3] G.J. Louter and A.J.H. Boerboom, in A. Quayle (Ed.), Advances in Mass Spectrometry, Heyden, London, Vol.8, 1980, p.1851.

[4] G.J. Louter, M.M.J. Lens and A.J.H. Boerboom, Int.J.Mass Spectrom. Ion Phys., 39 (1981) 197.

[5] A.J.H. Boerboom, G.J. Louter and J. Haverkamp, in D. Price and J.F.J. Todd (Eds.), Dynamic Mass Spectrometry, Heyden, London, Vol.6, in press.

[6] L. Kerwin, in C.A. McDowell (Ed.), Mass Spectrometry, McGraw-Hill Book Company, Inc., USA (1963), p.104.

[7] A.J.H. Boerboom, H. Matsuda and T. Matsuo, Int.J.Mass Spectrom.Ion Phys., 22 (1976) 273.

[8] R.G. Cooks, J.H. Beynon, R.M. Caprioli and G.R. Lester, Metastable Ions, Elsevier, Amsterdam, 1973.

[9] G. Puzo and J.C. Prome, in A. Quayle (Ed.), Advances in Mass Spectrometry, Heyden, London, Vol.8, 1980, p.1003.

[10] M.S. Kim and F.W. McLafferty, J.Am.Chem.Soc. 100 (1978) 3279.

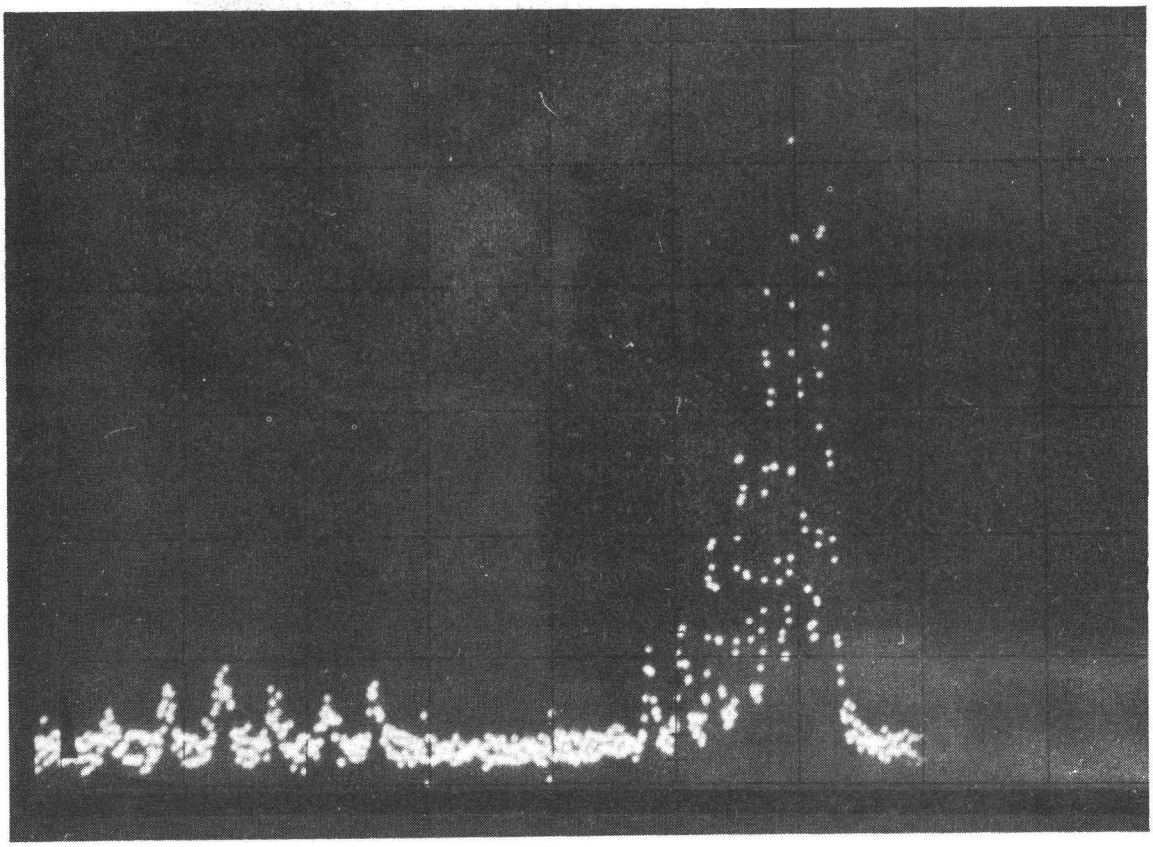

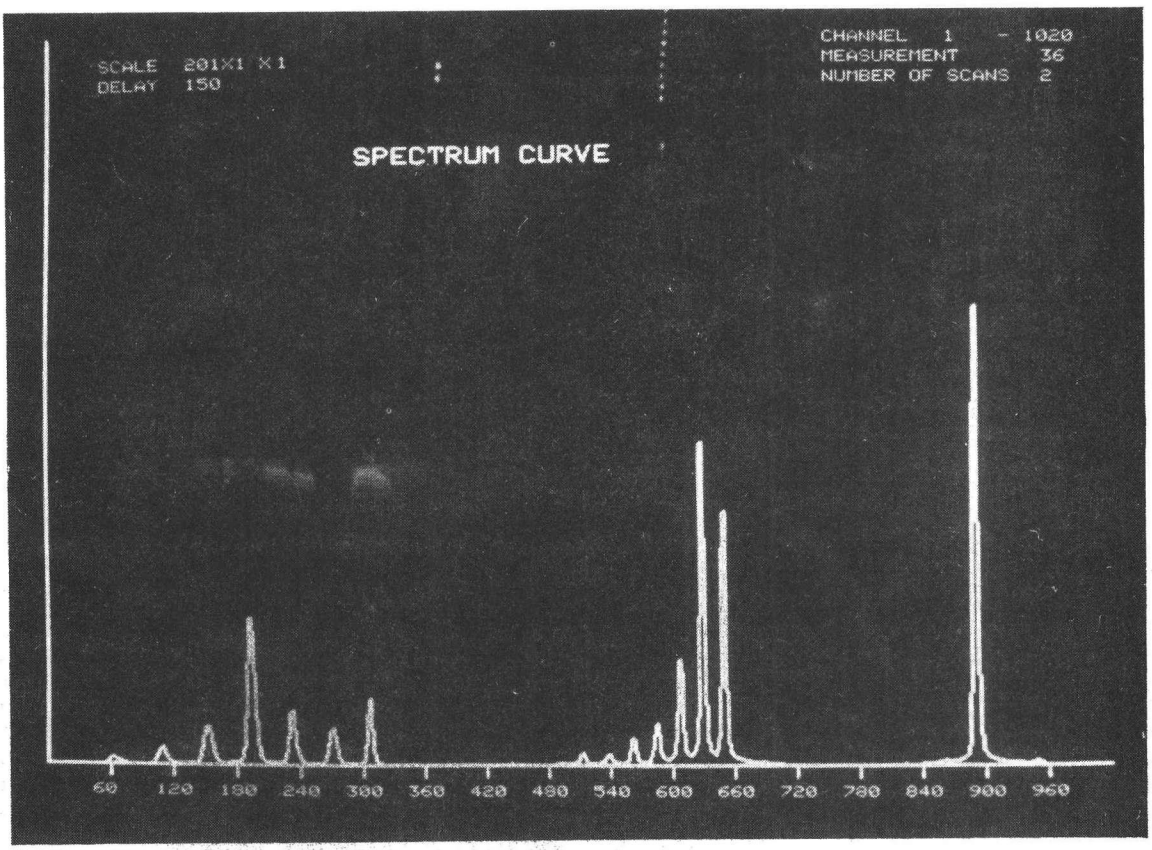

Photographs of a fragment spectrum as it can be observed real time on the monitor scope (above) and as it is plotted on the graphic display unit, after background correction and sensitivity correction (below).

C H A P T E R 4

A VERY SENSITIVE ELECTRO-OPTICAL SIMULTANEOUS ION DETECTION SYSTEM

ABSTRACT

A fully operational, electro-optical system for simultaneous detection is discussed. This system is applied for the simultaneous detection of fragment mass spectra, obtained by collision activated dissociation experiments. The detector itself consists of two chevron channelplates, phosphor screen, fibre optics, camera objective and photodiode array. It forms part of an extensive information system, which controls the photodiode array and performs data processing as for example background subtraction and correction of the spectrum for spatial sensitivity variations of the detector.

The detection system is characterized by a very low noise rate with an average value of about one dark ion per 250 s for each mass peak in the spectrum. The dynamic range of peak heights in a simultaneously detected spectrum can be up to 2.3×10^4 at a signal to noise ratio of 1. The reproducibility of peak area measurements is better than 20% over the entire length of the detector.

In this paper several characteristics of the detection system and the data processing will be discussed. Attention will be given to variations of the spatial sensitivity and to loss of spatial resolution, which both may occur in this type of systems.

I. INTRODUCTION

Simultaneous detection of mass spectra has some fundamental advantages over scanning detection, which is generally used in Mass Spectrometry (MS). In scanning instruments the limited observation time for each mass peak in a spectrum causes a sensitivity loss of several orders of magnitude. Also the observation time of the sample as a whole is more limited in these instruments, as fluctuations in the source conditions, e.g. sample pressure, may result in irreproducible mass spectra. Moreover, because of the limited scan velocity fast phenomena like flash pyrolysis [1] and laser pulse desorption [2] cannot be investigated with this type of instruments.

The main characteristics of the conventional simultaneous detector, the ion sensitive photographic plate, are small dynamic range (about 30), good spatial resolution, low sensitivity (more than 1000 ions are required for a measurable time) and a time consuming read-out procedure of the spectra. Electronic detection systems, used in scanning MS, are characterized by a much higher sensitivity (single ion counting) and dynamic range. Moreover, the spectrum, after the read-out procedure, is almost instantaneously available for interpretation and further data processing.

During the last decade an evolution is apparent of a new generation simultaneous detection devices [3,4,5]. These Electro-Optical Ion Detectors (EOID) are a combination of a Channeltron Electron Multiplier Array (CEMA or channelplate) [6], a phosphor screen and some sort of camera system. These detection systems combine the simultaneous ion detection and the advantages of electronic detection systems. In the following several characteristics of an operational EOID-system are discussed. Especially attention is given to the data processing, necessary to make full use of the profits of such a system.

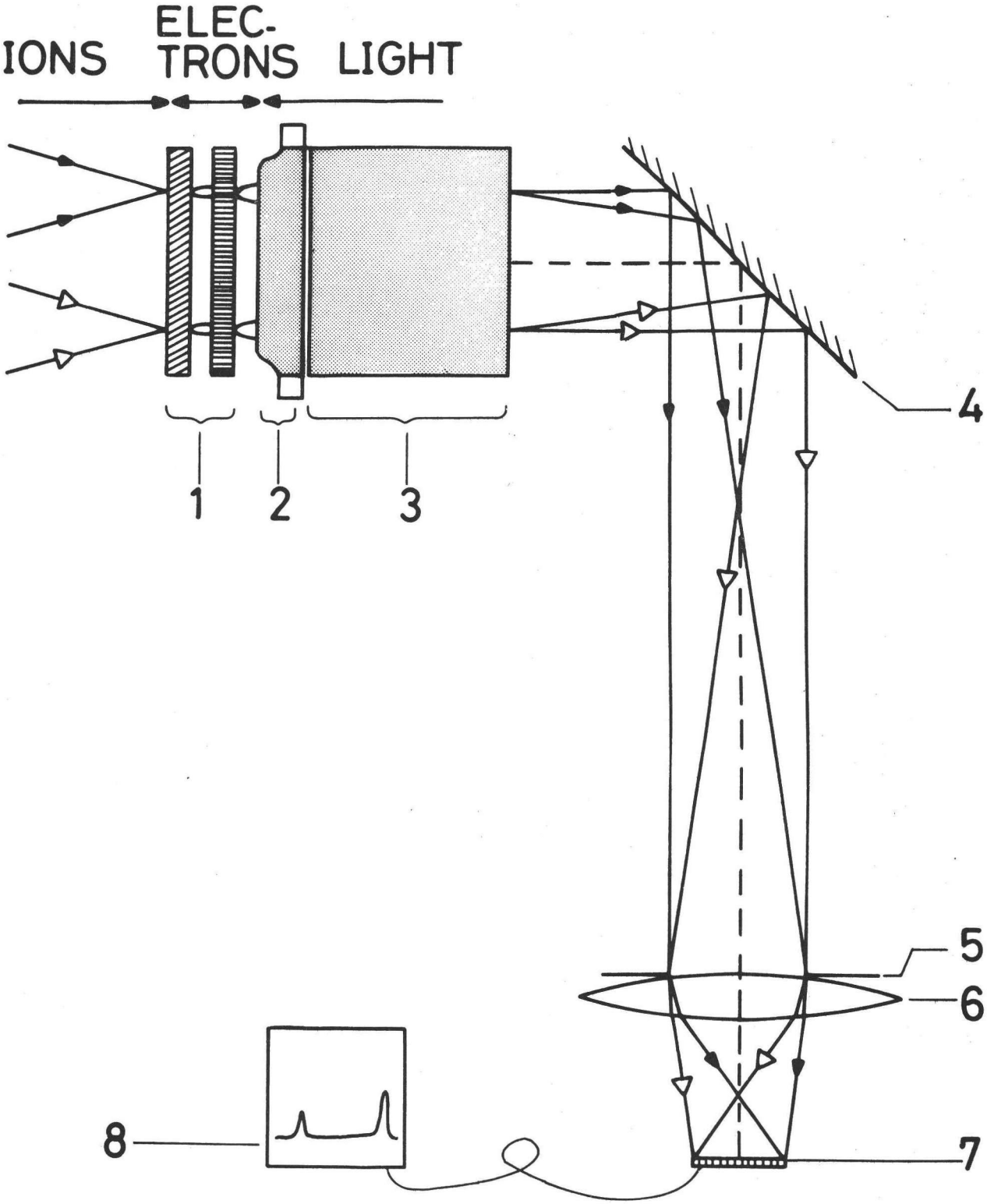

FIGURE 1

Schematic plan of the electro-optical system for simultaneous ion detection.

1) Chevron CEMA; 2) fibre optics slab with phosphor layer; 3) fibre optics; 4) mirror; 5) diaphragm; 6) aspherical lens; 7) photodiode array; 8) monitor scoop.

II. DETECTION AND DATA PROCESSING SYSTEM

II.1. The electro-optical ion detection system

The construction of the electro-optical detection system applied in our tandem MS is demonstrated in fig. 1. The first stage of the detector consists of a CEMA, in which the ions are converted into electrons with a gain up to 10^7. By the small dimensions of the channels (pore size 25 μm, center spacing 32 μm), each one acting as a channeltron, the spatial information, present in the CAD-fragment spectrum, is conserved to a large extend. The CEMA acts as a simultaneous amplifier; each channel amplifies independently of the other channels. The principle of simultaneous detection is maintained by applying an optical registration method: the electrons leaving the CEMA are accelerated up to 5 keV towards a phospor screen, directly coated upon a fibre optics slab. Chevron CEMA, phosphor screen and fibre optics have been obtained commercially as one set (type 3075-P20, Gallileo Electro-Optics Co., Massachusetts, USA).

Another fibre optics slab is used to guide the mass spectra out of the vacuum system. There, the optical registration of the spectra is performed by a self-scanned photodiode array. This array consists of 1024 pixels (photodiodes), each with a length of 25 μm and an aperture of 430 μm, and positioned with a repetition distance of 25 μm (overlap is less than 7%). A detailed description of self-scanned photodiode arrays is given by White et al. [7].

The dimensions of a CAD-spectrum, actually present on the fibre optics, are 75 mm × 15 mm, and are determined by ion-optical considerations, described by Louter et al. [8]. To adapt the length of the spectrum to that of the array, a reduced image of the spectrum is projected upon the array (linear magnification 0.3). For this purpose an aspherical camera objective (CANON FD 1.2/55 mm SSC AL) is applied (fig. 1). A drawback of this construction is that only 10% of the height of the mass lines actually contributes to the measurement. This is due to the relatively small aperture of our

photodiode array. Furthermore, even at maximum lens opening only 5°/oo of the signal is transmitted through the camera objective.

For simultaneous optical detection we use a self-scanned photodiode array, because of its good characteristics with respect to accuracy, spatial resolution and dynamic range, as will become apparent in section III. The optical detector module consists of a commercially available detector unit model 1410 and controller unit model 1218 (Princeton Applied Research, Princeton, New Jersey, USA).

The detection procedure is as follows. Each measurement starts with three preset frame scans to charge all photodiodes. Exposed to light, each diode discharges, the discharge being proportional to the total amount of light falling on a diode. After a programmable integration (or delay) time, the amount of discharge is measured in a so-called "read-out" scan, during which each diode is recharged again. The resulting analogue information from each diode is processed (Buss et al. [9]) and converted into 14 bits of measurement data, which is directly accessible as parallel TTL output of the controller unit. One bit corresponds to about 1000 electron-hole pairs generated in the photodiode. Each frame scan lasts about 16.4 ms, making each pixel inactive during a few microseconds. The delay time between subsequent frame scans is m times the frame scan time, where m is an integer.

II.2. System control and data processing

The application of the described EOID system has resulted in the development of an extensive information system, of which the main data streams are shown in fig. 2. The central element in this system is a PDP 11/70 computer (IAS time sharing operating system), by which we have comprehensive storage, plot and print facilities at our disposal. Local inspection and plotting of the mass spectra is possible by means of an intelligent graphic display unit. Communication between instrument and computer proceeds via a CAMAC serial

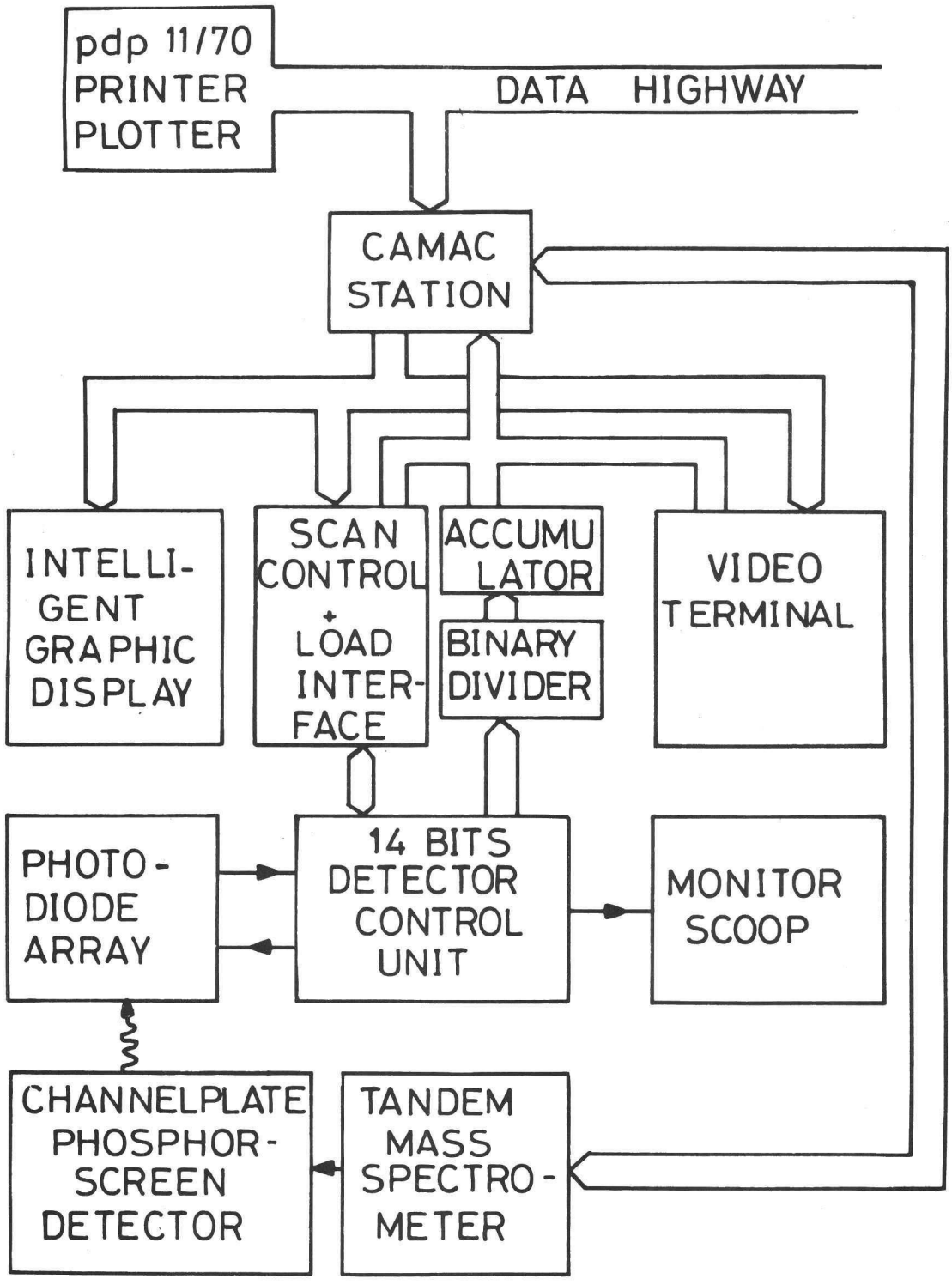

FIGURE 2

Data handling system.

highway system. Between CAMAC and the controller unit of the optical detector a home-made interface unit is applied for programming a scanning mode of the photodiode array. This can be done by loading a 4 K scanmemory present in the controller unit. A buffer memory of 1024 channels of 15 bits each, is applied for the accumulation of a programmable number of spectra. This memory has been provided with a programmable binary divider, to reduce the average peak height of the spectra leaving the control unit, opening the possibility of increasing the measuring time at the given memory capacity of the accumulator. This may also increase the dynamic range of peak heights in the simultaneously recorded spectrum.

The accumulated spectrum can now be loaded into the core memory of the computer, where it is directly accessible for further data processing.

Spectrum calculation

The main purpose of the data processing is to convert the raw data from the detector into a CAD-spectrum with a low noise level and a high dynamic range of peak intensities. The adequate operations are demonstrated in figure 3. In plot 3a we observe the raw data of a CAD-spectrum of mass 59 of isopropylamine, recorded in 17 frame scans with a delay time of 20 scan units each. A considerable amount of the signal still consists of background. Therefore a separate recording is made of this background signal, which is designated by "B". "B" is then subtracted from the raw spectrum resulting in the subtracted spectrum "S" (see fig. 3a-c). "S + B", "B" and "S" are directly accessible parts of the memory of the PDP 11/70 computer system. Next the zero line position is determined. For this purpose we use the first 25 channels of the photodiode array, which are shielded from light. The zero level is the average value of the contents of these 25 channels, after background subtraction.

The following step concerns the non-uniform spatial sensitivity of the detection system. This not only badly influences

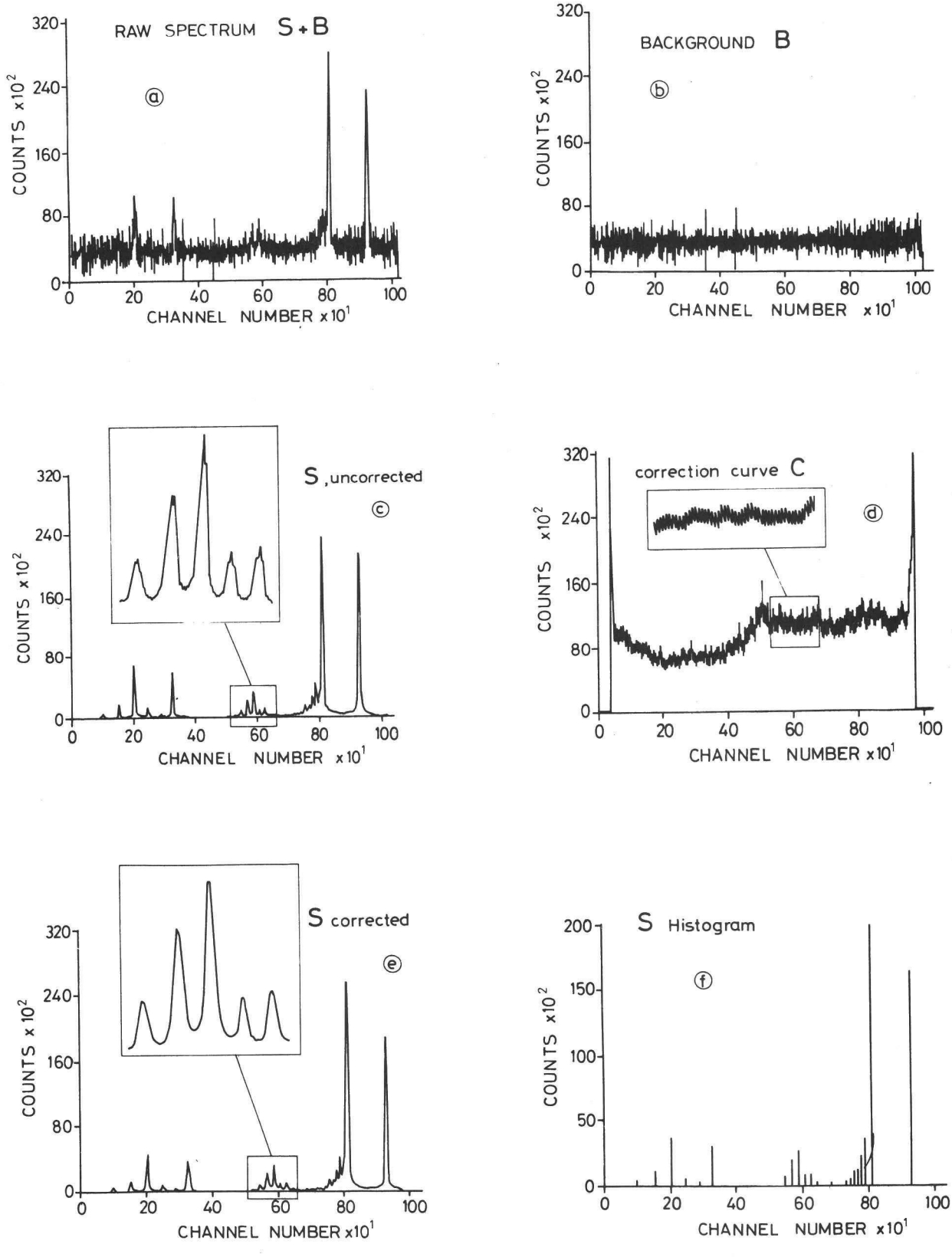

FIGURE 3

Various stages in the processing of CAD-spectra.

the relative peakintensities in spectra, but also affects the peak shape. In the inset in figure 3c this is demonstrated for the non-uniform sensitivity of the photodiode array. To correct for this effect we multiply "S" with a so-called correction curve, designated with "C". The subtracted and corrected spectrum overwrites "S" in the computer memory. Further options of the data processing program are the mass scale calculation, which should also apply when the mass dispersion is varied [10], and a spectrum compressing routine (fig. 3f). A program comprising the interpretation of CAD-spectra is still in development.

III. PERFORMANCE

Darksignal and noise

The raw data generated in the addition memory after a measuring cycle are given by

$$S_i = s_i + b_i + n_i \qquad (1)$$

where: i = the channel number,
s_i = actual spectrum component,
b_i = reproducible background component,
n_i = random noise component.

$b_i + n_i$ forms the total amount of darksignal. It is caused by the darkcurrent, generated during the integration process, combined with signals arising from the capacitive coupling of clock phases of the array into the video lines. b_i depends on the array temperature: at $-20.5^{\circ}C$ we measured

$$\bar{b} = k(0.227\ m + 204)\ \text{counts} \cdot \text{channel}^{-1} \qquad (2)$$

where $\bar{b}$ is the average of b_i over 1024 channels, k is the number of frame scans and m is the delay time in scan units. The factor 0.227 is about halved for each $7^{\circ}C$ decrease of the array temperature. The darksignal "B" is obtained simply by

performing a measurement with the ion beam switched off. Assume that "S + B" and "B" respectively, have been measured in k_{S+B} and k_B frame scans. From (2) it then follows that the dark signal should be multiplied by k_{S+B}/k_B to enable an adequate subtraction of the reproducible background. After subtraction only s small random noise component n_i remains [11]. At an array temperature of -20.5°C we measured for the effective noise in "S"

$$\bar{n} = \{(k_{S+B} + \frac{k_{S+B}^2}{k_B})(8 \times 10^{-4}\ m + 1.8)\}^{\frac{1}{2}} \text{ counts . channel}^{-1} \qquad (3)$$

Obviously the signal s_i (as well as b_i) increases proportionally to the number k of frame scans, whereas the irreproducible part only increases with $k^{\frac{1}{2}}$. The noise contribution of "B" decreases with increasing k_B, which is a result of the normalization factor k_{S+B}/k_B applied on "B".

A characteristic noise pattern is given in fig. 4. This "dark"-spectrum has been measured with $k_{S+B} = k_B = 2$ and $m = 2098$. The effective noise $\bar{n}$ in this figure is 3.6 counts . channel^{-1}.

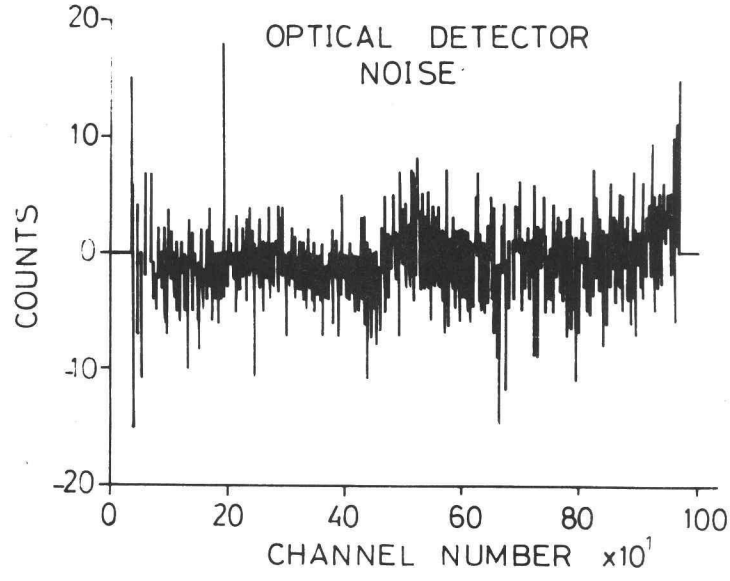

FIGURE 4

Characteristic noise pattern of the optical detection system, after background subtraction.

From (3) it follows, that the minimum noise in one frame scan is 1.4 counts . channel^{-1}. The maximum signal S_i per scan is determined by the 14 bits signal capacity of the controller unit. The dynamic range in peak heights per frame scan is therefore 1.2×10^4. Addition of 2 frame scans in the 15 bits accumulator makes a maximum dynamic range of 1.8×10^4 possible. By application of the binary divider this value can be further increased, though at the cost of sensitivity, to 3.3×10^4, corresponding with the 15 bits memory capacity.

A demonstration of the dynamic range is given in fig. 5. Here is plotted the CAD-spectrum of m/z 59 of the electron impact spectrum of acetamide ($k_{S+B} = k_B = 2$, m = 2098, measuring time 67 s). The peak height of m/z 59 is 3.1×10^4 counts, which is 95% of the memory capacity. The ratio of peak heights of m/z 59 and m/z 39 is 3×10^3. The effective noise in this spectrum is 3.6 counts . channel^{-1}.

In (3) only noise is considered, which originates from the photodiode array and the controller. However, there is also a noise component arising from the CEMA: spontaneous charge

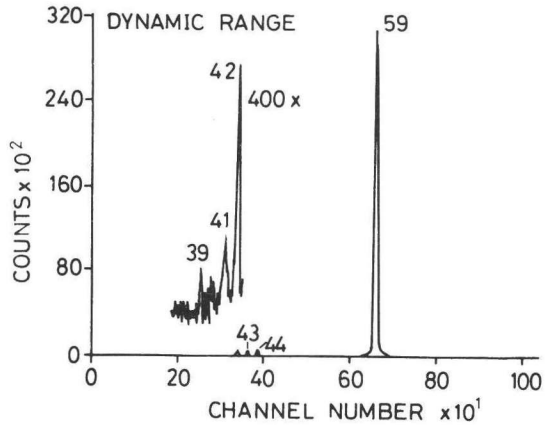

FIGURE 5

Demonstration of the dynamic range of peak heights in a simultaneously detected spectrum. The ratio of peak heights at m/z 59 and m/z 39 is 3×10^3; effective noise: 3.6 counts . channel^{-1}.

pulses are originating inside the channels of the CEMA, and result in peak-shaped responses on the detector. The count rate of these "dark ions" is smaller than 0.3 s^{-1}, at a maximum gain of the CEMA of 6.3×10^6 ($^{22}Ne^+$ beam of 4 keV). The dark ions are uniformly distributed over the full detector length with a probability density of 1.1×10^{-3} $channel^{-1}$. For a mass peak width of 13 channels, this results in an average dark ion count rate of one ion per 250 s for each mass peak. In figure 6 a characteristic picture of the dark ion shot noise is demonstrated. This plot is obtained in a measuring time of 67 s, at full lens opening of the objective and at maximum CEMA gain. The probability P(x) of the occurrence of x dark ions in a mass peak can be found by applying a binomial probability distribution for the detector region covered by a mass peak. For example at a peakwidth of 13 channels and after 250 s measuring time we calculated the probabilities $P(x = 0) = 0.37$, $P(x = 1) = 0.37$ and $P(x > 1) = 0.26$.

When used in counting mode, these values clearly indicate the lowest detection level of the system. When, however, as we are doing, the peak responses are used as a measure for the ion abundancies, the accuracy will be somewhat less.

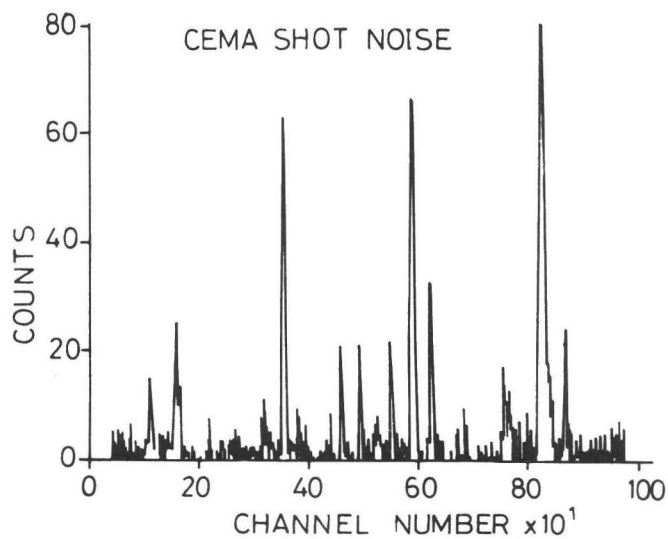

FIGURE 6

Shot noise or "dark ions", generated by the chevron CEMA at maximum gain and during a measuring time of 67 s.

This is explained by the variation of both ion and dark ion responses of the CEMA. According to manufacturer's specifications the individual responses of ions have an approximately Gaussian distribution about maximum gain [6]. The full width at half maximum (FWHM) is about 150%.

For the variation in dark ion responses we refer to figure 6, which gives a characteristic impression of the peak area distribution. The average peak area of dark ion responses is about 200 counts at full lens opening and maximum CEMA gain. Obviously, the gain of real ions is even larger than that of dark ions, resulting in even larger responses.

The highest, linearly detectable input current density, at maximum CEMA gain, is about 8.6×10^{4} times the dark ion count rate density of 3.4×10^{-15} A . cm^{-2}. The maximum input is limited by saturation of the CEMA channels. By lowering the gain of the CEMA, this maximum is increased, though, obviously, at the expense of sensitivity of the detection system as a whole.

Spatial resolution

The detection system incorporates a considerable loss of spatial resolution. This can be clearly seen in fig. 6: each peak in this plot is the response of a charge pulse originating in one channel of the first plate of the chevron CEMA. From this figure it follows, that at full lens opening the peak broadening is about 10 channels in the centre and 17 channels at the edges of the detector. At this diaphragm adjustment, the camera objective causes a resolution loss which varies from 3 channels in the centre to about 10 channels at the edges. At the expense of light transmission, the diaphragm can be closed, which increases the resolution. At f/D = 2.8 and 8.0 the peakbroadening diminishes to about 2 and 1 channels respectively over the full detector length.

The influence of the photodiode array upon the resolution is apparent from figure 7. Here is plotted the image on the photodiode array of a narrow slit, which is mounted upon the exit plane of the fibre optics. The image width is about

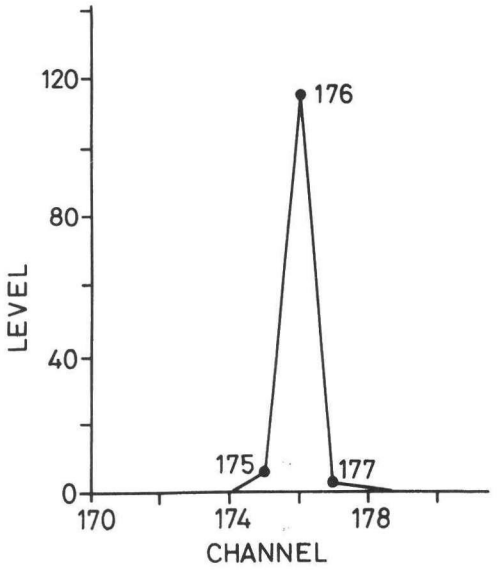

FIGURE 7

Spatial resolution of the optical detection system. A slit of 0.06 mm wide, positioned on the end of the fibre optics is imaged upon one pixel of the photodiode array.

20 μm and covers one pixel of the array. It is obvious from the figure that there is no significant signal leak to the neighbouring pixels. Each pixel acts as an isolated sampling unit.

Consequently the combination of CEMA, phosphor screen and fibre optics causes the remaining loss of 7 channels. As measured on the exit plane of the fibre optics, this corresponds to a spatial resolution of about 2 line pairs per mm (10% valley).

Sensitivity corrections

The marked non-uniformity of the spatial sensitivity is considered as a serious drawback of the EOID discussed above. It may result in mass spectra with irreproducible peak intensities. Moreover, it deteriorates the peak shape as is apparent from fig. 3c. These sensitivity variations are mainly caused by the photodiodes, which, according to the manufacturer, show a non-uniformity of

25%. They are also responsible for the bad peak shape. Another source of the irreproducibilities is the variation of CEMA gain with both position and incidence angle [12,13]. In our detection system we can greatly account for all these sensitivity variations by application of a correction curve "C", which contains a correction multiplication factor for each channel. This curve is the normalized reciprocal of the so-called sensitivity curve, which is easily obtained by scanning an ion beam of constant intensity with constant velocity along the CEMA, and next performing a background subtraction. The correction curve obtained in this way, appears to be greatly dependent on the adjustment of the CEMA gain and of the diaphragm opening of the camera objective. Moreover, the shape of "C" is slightly time dependent. Therefore, the recording of a correction curve should be a routine operation, which should be performed in regular intervals.

The accuracy of thus obtained correction curves obviously is limited, as its fine structure is affected by the loss of spatial resolution in the detection system. In our configuration the application of "C" results in a reproducibility in peak area measurements over the entire detector length, which is better than 20% and normally about 10%.
This is a significant improvement compared with the large sensitivity variations, reflected in for example the correction curve given in fig. 3d. Moreover, we have derived a noteworthy improvement of the peak shape, as is demonstrated in fig. 3d and e.

Conclusions and suggestions

In the foregoing it has been demonstrated that the detector set-up, presented in figure 1, results in a very sensitive simultaneous detection system for mass spectrometers. This high sensitivity is, however, accompanied by a considerable loss of spatial resolution. The main part of this loss, about 0.5 mm, is caused by the chevron CEMA-phosphor screen combination. For a single CEMA this loss has been discussed by Tuithof et al. [3].

It appears that the loss in resolution of a double CEMA with phosphor screen is about two times larger than a combination with a single CEMA. Therefore, a possibility to increase the spatial resolution is the application of a single channelplate with curved channels [14]. This recently developed model combines the high gain of a conventional chevron CEMA, with the resolution of a single one. Furthermore, if the dimensions of the detector permit this it is advantageous to apply a direct coupling between fibre-optics and the photodiode array [4,5]. In this case a single conventional CEMA can be used: the decrease of the CEMA gain is counter-balanced by the gain in light transmission. Moreover, also the loss in resolution caused by the camera objective can be avoided in this way.

We finally note, that the recent development of photodiode arrays with a larger aperture and a larger number of pixels will make it possible to construct electro-optical detectors with more channels per spectrum, a higher dynamic range and a larger effective detection area.

REFERENCES

[1] H.L.C. Meuzelaar, J. Haverkamp and F.D. Hileman, Curie-Point Mass Spectrometry of Biomaterials; Compendium and Atlas, Elsevier, Amsterdam, 1980.

[2] P.G. Kistemaker, M.M.J. Lens, G.J.Q. van der Peyl and A.J.H. Boerboom, in A. Quale (Ed.), Advances in Mass Spectrometry, Vol. 8A, Heyden, London, 1980, p.928.

[3] H.H. Tuithof, A.J.H. Boerboom and H.L.C. Meuzelaar, Int.J.Mass Spectrom.Ion Phys. 17 (1975) 299.

[4] C.E. Giffin, H.G. Boettger and D.D. Norris, Int.J.Mass Spectrom. Ion Phys. 15 (1974) 437.

[5] B. Hedfjäll and R. Ryhage, Anal.Chem. 51 (1979) 1687.

[6] J.L. Wiza, Nucl.Instrum.Meth. 162 (1979) 587.

[7] M.H. White, in: P.G. Jespers, F. van de Wiele and M.H. White (Eds.), Solid State Imaging, Noordhof, Leyden, 1976, p.165.

[8] G.J. Louter, A.J.H. Boerboom, P.F.M. Stalmeier, H.H. Tuithof and J. Kistemaker, Int.J.Mass Spectrom.Ion Phys. 33 (1980) 335.

[9] R.R. Buss, S.C. Tanaka and G.P. Wenckler, in: P.G. Jespers, F. van de Wiele and M.H. White (Eds.), Solid State Imaging, Noordhof, Leyden, 1976, p.561.

[10] G.J. Louter, M.M.J. Lens and T. Matsuo, Int.J.Mass Spectrom.Ion Phys., in press.

[11] R.W. Simpson, Rev.Sci.Instrum. 50 (1979) 730.

[12] J.P. Macau, J. Jamar and S. Gardier, IEEE NS, 23 (1976) 2049.

[13] W. Parkes, R. Gott and K.A. Pounds, IEEE NS, 17 (1970) 360.

[14] M. Audier, J.C. Delmotte and J.P. Boutot, Rev.Phys.Appl., 13 (1978) 188.

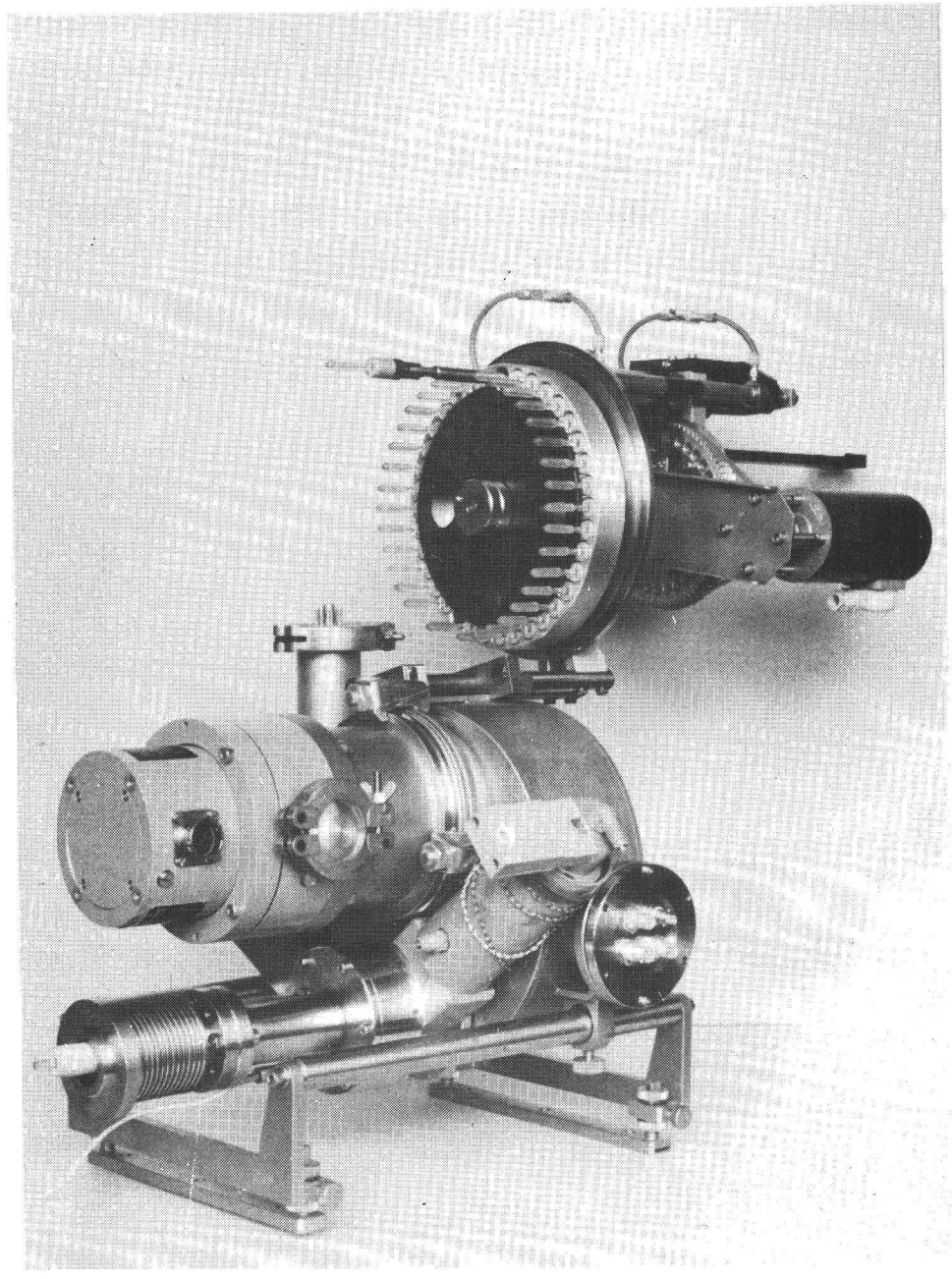

Curie-point pyrolysis inlet system with automatic sample exchange.

C H A P T E R 5

STRUCTURE ANALYSIS OF PYROLYSIS FRAGMENTS BY COLLISION ACTIVATED DISSOCIATION MASS SPECTROMETRY

INTRODUCTION

Collision Activated Dissociation Mass Spectrometry (CAD-MS) is a rapidly developing technique for structure identification of unknown ions. It is based on the fact that the fragmentation pattern of ions is generally very characteristic for their composition and structure [1]. With this technique it is even possible to identify isomeric ions, which is generally not possible in conventional MS.

The tandem MS has been especially developed to perform CAD experiments. Its featuring characteristic, compared with other instruments of CAD-MS, is that it combines a relatively high mass resolution of the fragment spectra of about 500, and a very high sensitivity. This could, firstly, be achieved by post-acceleration of the fragment ions, which considerably reduces their angular and relative kinetic energy spread, caused by Kinetic Energy Release at the fragmentation processes [2]. Furthermore, the sensitivity could be improved by application of quadrupole lenses and an electro-optical simultaneous ion detector [3,4].

Because of these properties the tandem MS is pre-eminently suitable for CAD-MS structure elucidation of compounds arising in short lasting processes as e.g. laser desorption [5], flash pyrolysis (Curie-point pyrolysis) [6] and field desorption MS [7,8]. Moreover, application of simultaneous detection enables us to obtain reproducible CAD-spectra, even when processes are involved which show a rapidly varying precursor ion current.

The following two examples will illustrate the applicability of the instrument. The first section discusses a typical biochemical application. The identification of *Mycobacterium*

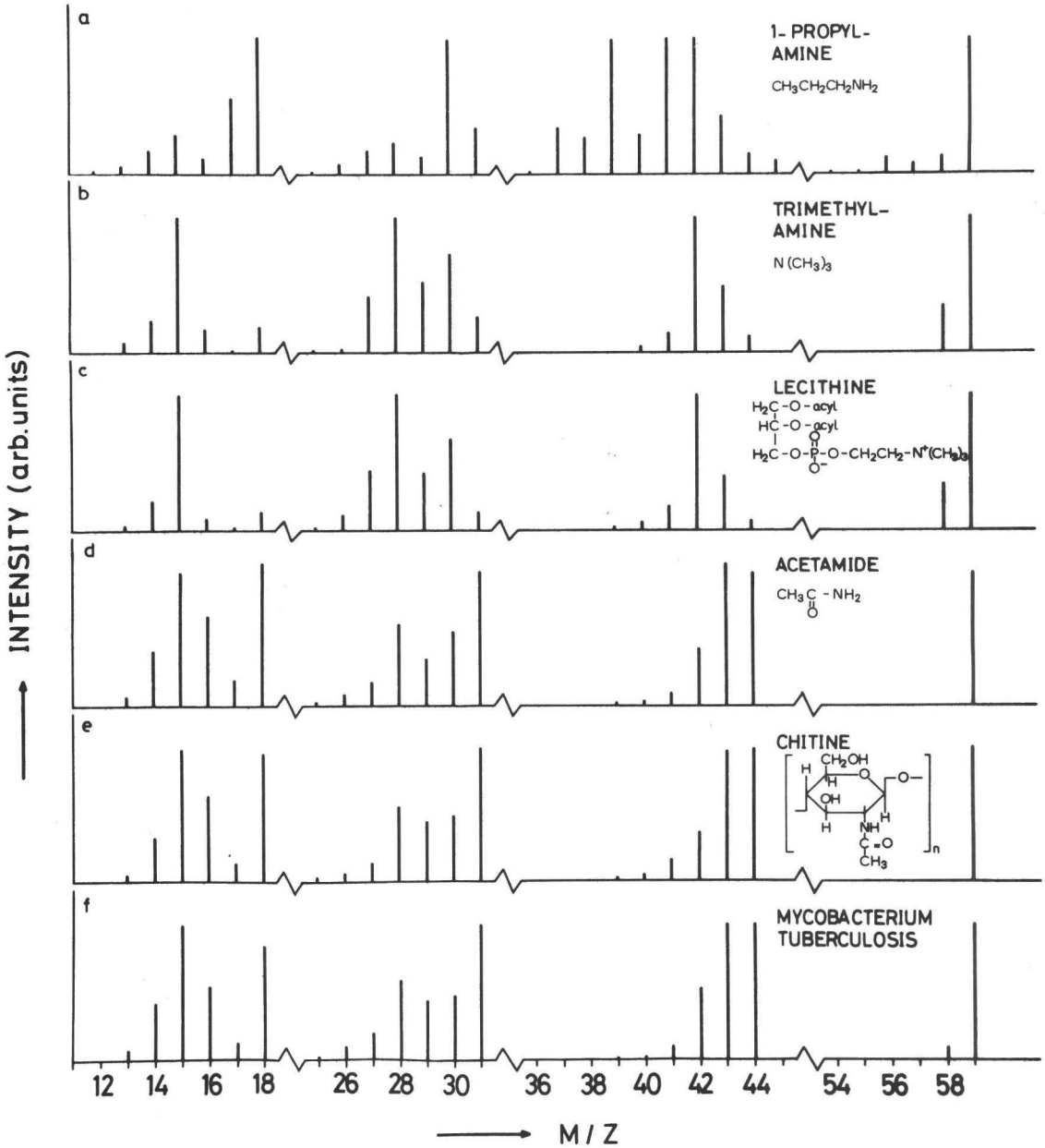

FIGURE 1

CAD spectra of the precursor ion at m/z 59 in the pyrolysis mass spectrum of lyophilized cells of *Mycobacterium tuberculosis* as compared with reference CAD spectra of the molecular ion (m/z 59) of 1-propylamine, trimethylamine and acetamide, and of the 59^+ ions in the pyrolysis mass spectra of lecithine and chitine. Instrumental conditions: energy of the ionising electrons 70 eV, energy of the precursor ions, 4 keV; collision gas, Ne; pressure inside the collision cell $\sim 10^{-1}$ torr; post-acceleration, 20 keV; pyrolysis temp. 320°C, total pyrolysis time, 2 min. No correction was made for spatial sensitivity variations of the detector. The reproducibility of the peak intensities within a mass group (see Fig. 2) therefore is typically better than 10%.

strains by pyrolysis-low voltage EI mass spectrometry is already several years subject of investigation in our group [6,9-11]. The main purpose is the identification of so-called Tuberculosis complex *Mycobacterium* strains. The species belonging to this group, viz. *M.bovis*, *M.bovis BCG* and *M.tuberculosis* can cause severe diseases (tuberculosis) in man and animal. A fast and fully automated system for recognition of such dangerous strains within series of clinical *Mycobacterium* isolates was developed by Meuzelaar et al. [6] and Wieten et al. [9-11]. A discrimination between pyrolysis mass spectra of Tuberculosis complex strains and other less pathogenic strains has been made by computer, using multivariate spectrum analysis. The procedure is based on the occurrence of significant differences in the relative intensities of a small set of characteristic "key" masses, one of them being m/z 59. In order to trace back the biochemical origin of such inter-species differences the chemical structures contributing to such a key mass have to be determined. CAD-MS is applied for this structure identification.

The second section discusses an organic-chemical application. Here the purpose of the identification of the precursor ion is the elucidation of mechanisms of thermal fragmentation of organic molecules in the gasphase. Discussed here is the identification of m/z 40 in the Curie-point pyrolysis MS of 2,3-butadienoic acid, by comparison of its CAD-spectrum with that of a set of isomeric model compounds. For this application we used an on-line Curie-point pyrolysis inlet system. Therefore, there was only a short measuring time per sample of about 5 s, accompanied by a rapidly changing precursor ion current.

STRUCTURE ELUCIDATION OF M/Z 59 IN THE PYROLYSIS EI-SPECTRUM OF COMPLETE BACTERIA

M/z 59 in the pyrolysis mass spectra of bacteria can have several origins. Two probable fragment molecules with mass 59, liberated by thermal fragmentation of such complex biological matter are acetamide and trimethylamine. Acetamide can be de-

rived mainly from N-acetylaminosugar moieties like N-acetylhexosamines [12] and N-acetylneuraminic acids [13] present as building blocks in polysaccharides and glycoconjugates, and, to a lesser extent also from proteins [12,14]. Trimethylamine is a very characteristic pyrolysis product from choline and choline conjugates (e.g. phosphatidyl choline [15]. Another compound possibly contributing to m/z 59 is 1-propylamine which could be formed as a pyrolysis product from amino-compounds like proteins, (non-protein) amino acids or polyamines.

In Fig. 1a, b and d the collision induced dissociation spectra are given of the $M^{+\bullet}$-ions of 1-propylamine, trimethylamine and acetamide, respectively. The spectra of the isomeric amines show strong differences. In the spectrum of 1-propylamine intense peaks at m/z 43, 41 and 39 probably represent the alkyl fragments $C_3H_7^+$, $C_3H_5^+$ and $C_3H_3^+$. The intense peak at m/z 42 can be assigned to the fragment $H_3C-CH=CH_2^{+\bullet}$ and the peak at m/z 30 may represent the fragment $H_2C=NH_2^+$. The formation of NH_4^+ (m/z 18) from this primary amine is evident.

The spectrum of the tertiary amine also shows intense peaks at m/z 43 and 42 which in this case may represent the fragments $[H_3C-N=CH_2]^{+\bullet}$ and $[H_2C=N=CH_2]^+$, respectively. For m/z 30, the same explanation can be given as mentioned for 1-propylamine; the peak at m/z 28 may be CH_2N^+. Both amines show the production of M - H fragments (m/z 58) in significant amount).

The CAD-spectrum of the 59^+-ion in the pyrolysis mass spectrum of the reference compound lecithin (phosphatidyl choline, Fig. 1c) shows a very close correspondence with the spectrum in Fig. 1b, indicating that the fragment with mass 59, formed on pyrolysis of this phospholipid is exclusively trimethylamine.

The CAD-spectrum of the $M^{+\bullet}$-ion of acetamide (Fig. 1d) differs from the spectra obtained for both amines, e.g. in that it shows no M - H formation, whereas high intensities are found at m/z 44, 43 and 31 (probably representing the fragments $O=C=NH_2^+$, $H_3C-C\equiv O^+$ and $H_3C-NH_2^{+\bullet}$, respectively). Again the peak at m/z 18 has to be attributed to NH_4^+. The high intensities at m/z 31, 30 and 29 as compared with 70 eV EI spectra of acetamide are remarkable.

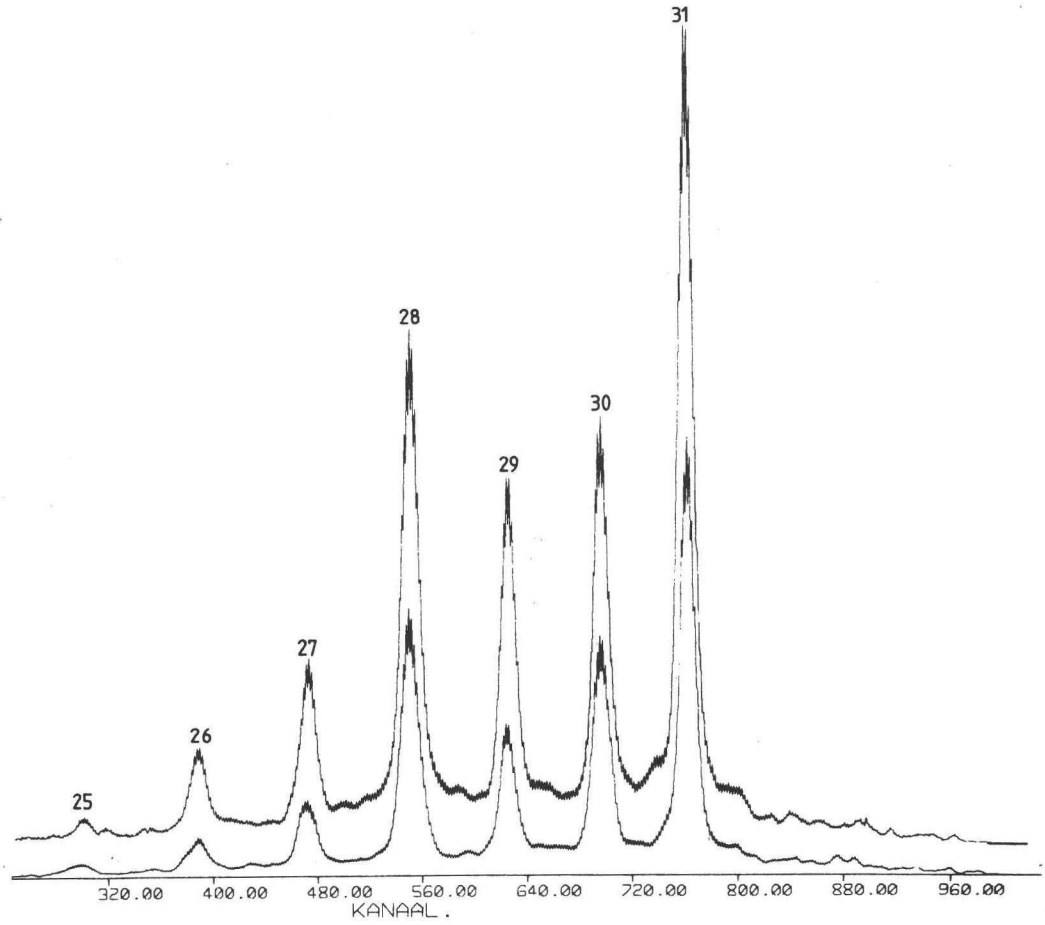

FIGURE 2

Comparison of the m/z 25 - 31 region of the CAD spectra of mass 59 of the acetamide (below) and of the pyrolysate of *Mycobacterium tuberculosis* cells (above). Instrumental conditions: see Fig. 1. The total ion current leaving the collision cell was about 4×10^{-14} Amps., the measuring time about 3.6 s.

An identical CAD spectrum was obtained from the 59^+-ion in the pyrolysis mass spectrum of the macro-molecular reference compound chitine (Fig. 1e), a linear polymer of $\beta(1 \rightarrow 4)$ linked N-acetylglucosamine residues, so that the formation of acetamide on pyrolysis of this polymer is evident.

Fig. 1f shows the CAD mass spectrum obtained from the 59^+-ion in the pyrolysis mass spectrum of complete, lyophylized cells of *Mycobacterium tuberculosis*. Comparison of this spectrum with those of the reference substances (Fig. 1a, b and d) clearly indicates that this characteristic pyrolysis fragment is almost exclusively acetamide. The small peak at m/z 58

(see Fig. 1) may point to a very small contribution of some alkylamine with mass 59. In Fig. 2 the m/z 25 - 31 part of the CAD spectrum of acetamide as produced actually by the instrument is compared with the corresponding mass range in the CAD spectrum of 59^+ in the pyrolysate of the *Mycobacterium* strain.

This finding implicates that in the identification by pyrolysis mass spectrometry of *Mycobacterium* strains of the Tuberculosis complex the relative amount of acetamide, which should be considered as derived mainly from cell wall N-acetylamino-sugar components, is an important parameter.

ELUCIDATION OF THE MECHANISM OF THERMAL CO_2-LOSS FROM 2,3-BUTADIENOIC ACID

The Curie-point pyrolysis mass spectrum of 2,3-butadienoic acid (I) shows an interesting peak at m/z 40, caused by pyrolytic CO_2-loss from the complete molecule [16]. In principle there are different mechanisms possible for this loss, which result in particles with similar gross formula C_3H_4, but with different structure (Fig. 3). Obviously this mechanism of

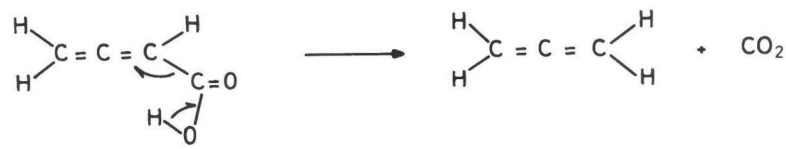

I IIa

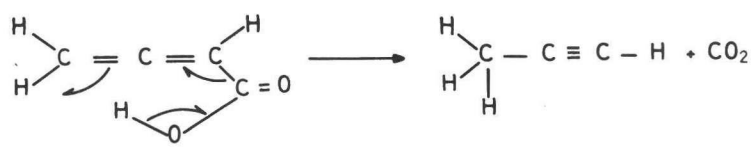

IIb

FIGURE 3

Two assumed pyrolytic decomposition pathways of 2,3-butadienoic acid into a fragment with molecular weight 40.

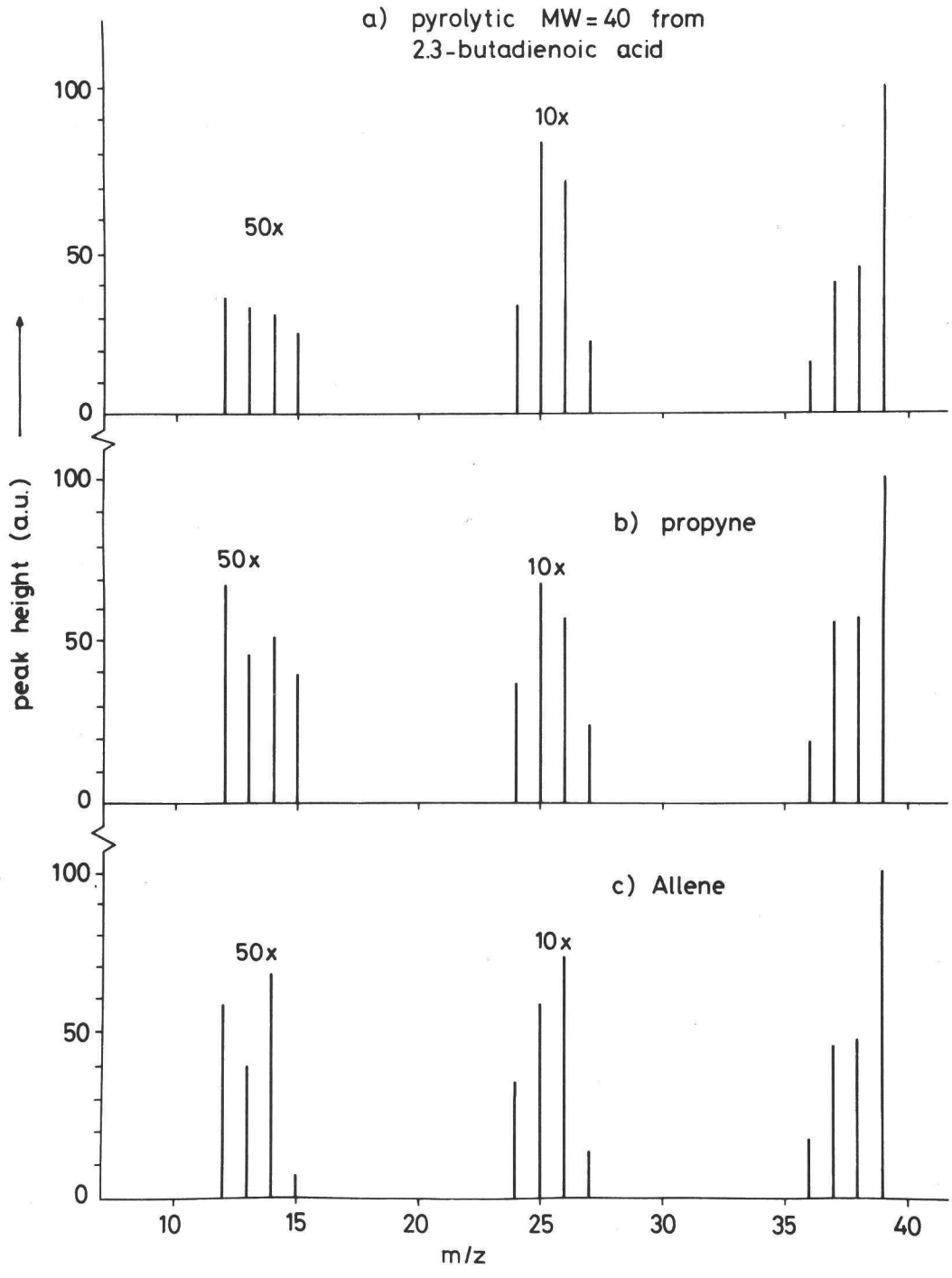

FIGURE 4

a) Py-CAD-mass spectrum of m/z 40 in the EI-spectrum of 2,3-butadienoic acid;

b and c) CAD-mass spectra of m/z 40 of propyne and allene, respectively.

thermal CO_2-loss from the acid can be determined by identifying the structure of m/z 40 in the pyrolysis mass spectrum. The identification has been performed with the tandem MS, provided with the on-line Curie-point pyrolysis inlet system.

About 5 µg of the 2,3-butadienoic acid was applied upon the pyrolysis wire, and then pyrolysed in a vacuum of about 10^{-5} Torr to a maximum temperature of 610°C. The gaseous pyrolysis products were next introduced via a capillary, into the ion source, where they were ionized by low-energy electrons (14 eV). The precursor ions were preselected on m/z 40 in the first stage of the tandem MS and fragmented by collision on helium atoms. After the collision cell the fragment ions were post-accelerated with 15 keV. The CAD-spectrum was simultaneously detected over a mass range m/z 12 - 40. This spectrum has been compared with the CAD-spectra of allene (IIa) and propyne (IIb), which both have been measured under similar experimental conditions as described above (fig. 4).

From this comparison it appears that the product with molecular weight 40, arising from pyrolysis of 2,3-butadienoic acid (I) has the propyne structure. This corresponds with the results of Bigley et al. [17].

So we may conclude that the mechanism of thermal CO_2-loss from (I) is not a 1,2 elimination of CO_2, but a 1,5-H-shift, before or during the CO_2-elimination.

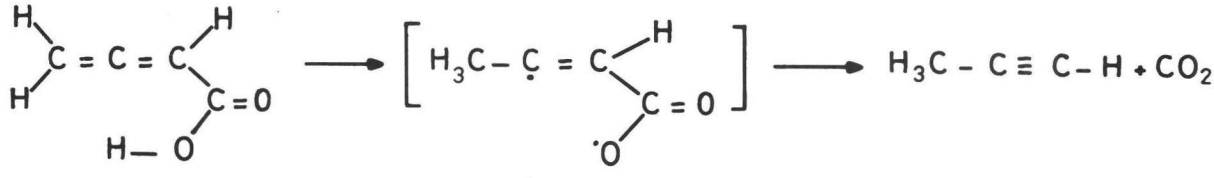

REFERENCES

[1] K. Levsen, Fundamental Aspects of Organic Mass Spectrometry, Verlag Chemie, Weinheim-New York, 1978.

[2] H.H. Tuithof, Int.J.Mass Spectrom.Ion Phys., 23 (1977) 147.

[3] G.J. Louter, A.J.H. Boerboom, P.F.M. Stalmeier, H.H. Tuithof and J. Kistemaker, Int.J.Mass Spectrom.Ion Phys., 33 (1980) 335.

[4] G.J. Louter and A.N. Buijserd, submitted for publication.

[5] M.A. Posthumus, P.G. Kistemaker, H.L.C. Meuzelaar and M.C. ten Noever de Brauw, Anal.Chem., 50 (1978) 985.

[6] H.L.C. Meuzelaar, P.G. Kistemaker, W. Eshuis and H.W.B. Engel, in H.H. Johnston and S.W.B. Newsom (eds.), Rapid Methods and Automation in Microbiology, p.225, Learned Information, Oxford, U.K., 1977.

[7] H.D. Beckey, Principles of Field Ionization and Field Desorption Mass Spectrometry, Pergamon Press, London, 1977.

[8] J. van der Greef, Thesis, Chapter 12, University of Amsterdam, 1980.

[9] G. Wieten, J. Haverkamp, H.L.C. Meuzelaar, H.W.B. Engel and J. Tarnok, G.P. Kubica, L.G. Wayne and L.S. Good (Eds.), 1954-1979: Twenty-five years of mycobacterial taxonomy, p. 176, CDC-press, Atlanta, U.S.A.

[10] G. Wieten, J. Haverkamp, H.W.B. Engel and L.G. Berwald, Rev.Infect. Dis., in press.

[11] G. Wieten, J. Haverkamp, H.L.C. Meuzelaar, H.W.B. Engel and L.G. Berwald, J.General Microbiol., 122 (1981) 109.

[12] P.G. Simmonds, Appl.Microbiol., 20 (1970) 567.

[13] J. Haverkamp, H.L.C. Meuzelaar, E.C. Beuvery, P.M. Boonekamp and R.H. Tiesjema, Anal.Biochem., 104 (1980) 407.

[14] H.R. Schulten, H.D. Beckey, H.L.C. Meuzelaar and A.J.H. Boerboom, Anal.Chem., 45 (1973) 191.

[15] A.C.M. Weijman, in C.E.R. Jones and C.G.A. Cramers (Eds.), Analytical Pyrolysis, p.225, Elsevier, Amsterdam, 1977.

[16] J.W. Dallinga, N.M.M. Nibbering, A.J.H. Boerboom and G.J. Louter, to be published

[17] D.B. Bigley and R.H. Weatherhead, J.C.S. Perkin II, (1976) 704.

PYROLYSE-DUBBELTRAPS MASSASPECTROMETER

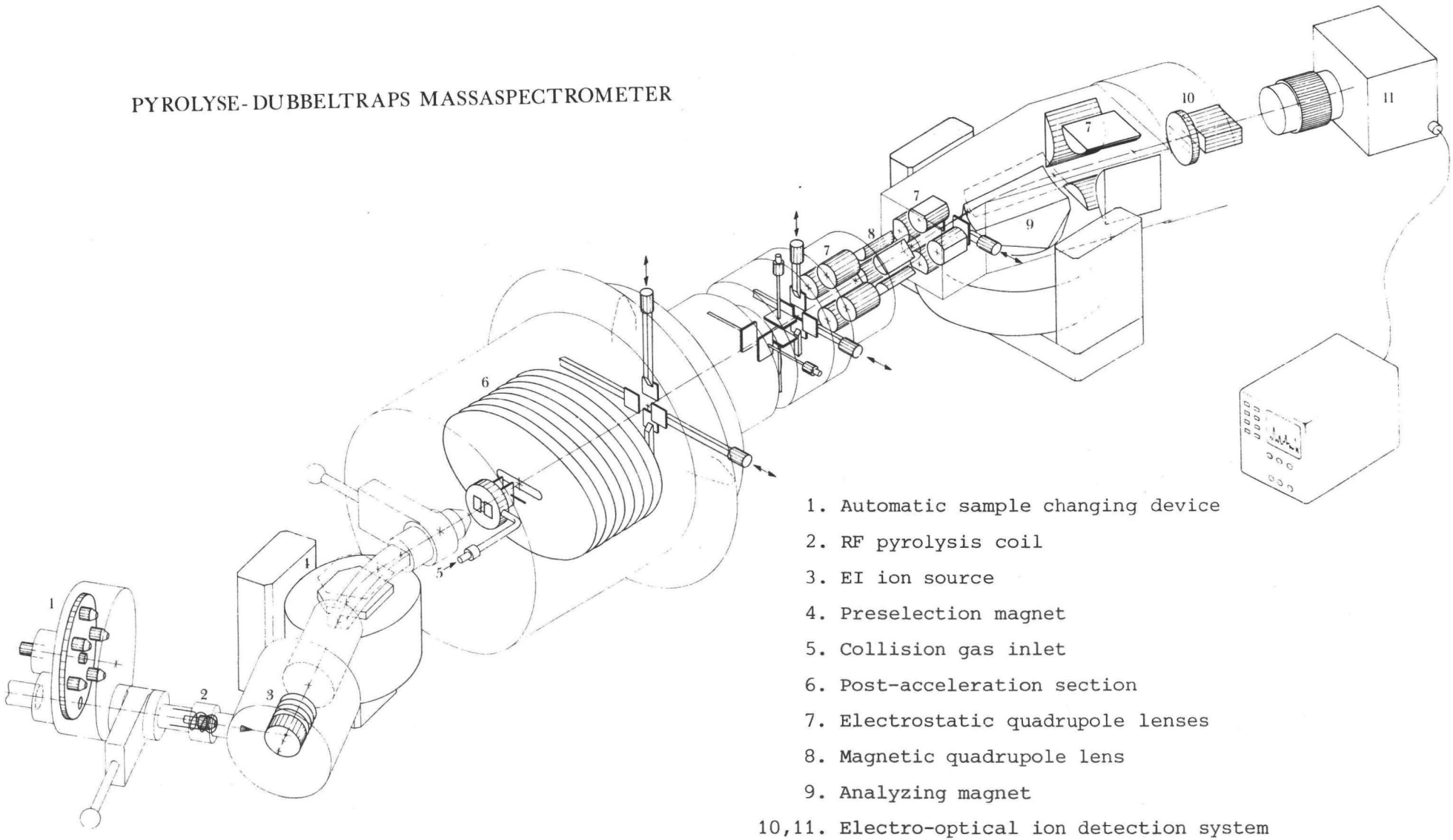

1. Automatic sample changing device
2. RF pyrolysis coil
3. EI ion source
4. Preselection magnet
5. Collision gas inlet
6. Post-acceleration section
7. Electrostatic quadrupole lenses
8. Magnetic quadrupole lens
9. Analyzing magnet

10,11. Electro-optical ion detection system

10. CEMA and phosphor screen
11. Camera lens and photodiode array

S U M M A R Y

During the last decade Collision Activated Dissociation Mass Spectrometry (CAD-MS) has developed into an important and sometimes unique technique for the structure elucidation of ions. In this technique the ions, which are to be identified, are fragmented by collisions with neutral atoms as for example He. Next the mass spectrum of the resulting fragment ions is measured. Identification of the precursor is possible, because generally the fragment ion spectrum of ions is very characteristic for their composition.

When done in conventional MS, CAD-MS results in poor mass resolution (≈ 70) and a very low sensitivity. This is mainly caused by the large angular spread as well as by the spread in relative energy of the fragment ions.

This thesis gives an extensive description of the double stage MS, which has been especially developed for CAD-MS. In our instrument a high mass resolution and a very high sensitivity are obtained by application of special techniques like post-acceleration of fragment ions, quadrupole (Q-pole) lenses and an electro-optical, simultaneous ion detection system. In chapter 1 a general view of the apparatus is given and the functioning of the ion-optics is discussed. The first stage of the tandem MS consists of a conventional sector type MS with electron-impact ion source. The mass resolution is about 600 at 10% valley criterion. A collision cell with a length of 10 mm is positioned at the site of the detector slit of the first stage. After post-acceleration, the fragment ions are mass-analyzed by a second, specially designed, sector magnet, followed by simultaneous detection of the fragment ion. The ratio of highest and lowest mass in a simultaneously recorded spectrum is usually 4 : 1. It can be varied however between 12 : 1 and 1.06 : 1 by application of an electrostatic Q-pole, situated between magnet and simultaneous detector. Three more Q-poles are used to translate and rotate the mass focal plane towards an optimum position with respect to the flat channelplate detector plane. The ion transmission from collision cell to detector is 60% for a simultaneously detected spectrum. However,

it can be increased up to 100% for each individual peak in the CAD-spectrum.

In chapter 2 the operation of the rather complex ion-optics is demonstrated by application of a computer simulation of the tandem MS. Special attention is given to the action of the four Q-pole lenses and the second sector magnet upon curvature and position of the mass focal plane. We gave also attention to the mathematical model itself, which is based on a first order approximation of the ion-optics, using a matrix representation. We compared calculated and experimental adjustments of the Q-poles. The calculated adjustments agree remarkably well with the experimental values. Calculated values can be directly used for automatic tuning of the instrument. No significant peak broadening in the CAD-spectra is to be expected.

In chapter 3 two mass calibration methods are described for the fragment spectra. The so-called polynomial-method applies a fifth-order polynomial approximation of the functional relation between position on the detector and corresponding relative momentum of fragment ions. This method can only be used with unchanged dispersion. We used a second method however, which can also be applied in case the dispersion is varied. This method uses the matrix model of the instrument, as discussed in chapter 2. With both methods a nominal mass assignment can be obtained up to m/z 1000. Moreover, attention is given to possible peakshifts in CAD-spectra, resulting from kinetic energy loss of precursor ions during the collision process. In conventional MS these shifts can cause errors in mass assignment. By application of post-acceleration and a magnetic mass analyzer, this effect is negligibly small in our tandem MS.

Chapter 4 discusses the entire detection system. The detector consists of two channelplates (CEMA), a fibre optics slab, coated with a phosphor layer, a camera objective and a 1024-channels photodiode-array. The detector is part of an extensive information system, which also provides for the necessary data processing. The data processing mainly consists of spectrum calculation routines: subtraction of background signal and correction for spatial sensitivity variations of the detection system. Background characteristics of both optical detector and CEMA have been determined experimentally. The average ion res-

ponse of the detector is about 200 counts (1 count = 1000 electrons from the optical detector). The average noise of the CEMA is approximately 1 dark ion per 250 s, per mass peak. The noise of the optical detector is porportional to the square root of the measuring time and is temperature sensitive. After subtraction of the background and at an array temperature of -20.5°C, the integrated noise during 250 s is only 46 counts per mass peak. The maximum dynamic range of peak heights in the simultaneously detected spectrum is 3.3×10^4, at a signal to noise ratio of 1. Its value is limited by the capacity of the local memory used for data accumulation. Application of a spatial sensitivity correction improves the reproducibility of peak area measurement by a factor of 4 (better than 20%).

Chapter 5 gives a bio-chemical and an organic-chemical application of the instrument. As bio-chemical application the peak m/z 59 in the pyrolysis mass spectrum of complete mycobacteria is identified. This mass is part of a group of peaks, with which we can distinguish between not-dangerous bacteria, and bacteria of the same sort, which may cause tuberculosis. The identification of m/z 59 as acetamide learns that one of the bio-chemical differences between these bacteria is determined by N-acetyl-aminosugar components in the cell-walls. As an example of organic-chemical application we investigated the fragmentation process of 2,3-butadienoic acid. The pyrolysis fragment with MW = 40 has been identified as propyne. By means of their CAD-spectra, propyne can be clearly distinguished from the isomeric alternative model compound allene.

S A M E N V A T T I N G

Gedurende de laatste tien jaren is de Botsings Geaktiveerde Dissociatie Massaspektrometrie (BGD-MS) ontwikkeld tot een belangrijke en soms unieke techniek om de samenstelling en struktuur van ionen vast te stellen. Bij deze techniek laat men de te onderzoeken ionen uiteen vallen in fragmenten, door ze te laten botsen met bijvoorbeeld heliumatomen. Van deze fragmenten wordt het massaspektrum bepaald. Identifikatie is nu mogelijk, omdat een fragmentenspektrum in het algemeen karakteristiek is voor het bijbehorende prekursorion.

Indien BGD-MS gedaan wordt in een konventionele massaspektrometer heeft men te kampen met zowel een lage massaresolutie (≈ 70) als een zeer geringe gevoeligheid. Voor een belangrijk gedeelte vinden deze problemen hun oorzaak in een grote hoekspreiding en een grote spreiding in relatieve energie van de fragmentionen van eenzelfde massa.

Dit proefschrift geeft een uitgebreide beschrijving van de dubbeltrapsmassaspektrometer, die speciaal ontwikkeld is voor het verrichten van BGD-experimenten. Door toepassing van o.a. naversnelling van de fragmentionen, quadrupoollenzen en een elektro-optisch, simultaan detektiesysteem zijn een hoge massaresolutie en een zeer grote gevoeligheid in dit instrument gekombineerd. In hoofdstuk 1 wordt een algemene beschrijving van het instrument gegeven, en wordt ingegaan op de werking van de ionenoptiek. De eerste trap van de dubbeltraps MS bestaat uit een konventionele electron-impact ionenbron en een sektormagneet. De massaresolutie bedraagt ongeveer 600. Op de plaats van de detektiespleet bevindt zich een 10 mm lange botskamer. Na naversneld te zijn worden de fragmentionen op massa gescheiden met behulp van een speciaal ontworpen tweede sektormagneet. Ze worden vervolgens simultaan gedetekteerd over een gebied waarvan de verhouding tussen hoogste en laagste massa 4 : 1 bedraagt. Dit massagebied kan met een elektrostatische quadrupool na de magneet gevarieerd worden tussen 12 : 1 en 1,06 : 1. De drie overige quadrupoollenzen verzorgen de translatie en rotatie van het beeldvlak naar een optimale positie ten opzichte van de vlakke detektor. De ionentransmissie van

botskamer tot detektor bedraagt 60% voor een simultaan gemeten spektrum. Deze waarde kan verhoogd worden tot 100% voor een afzonderlijke piek in het spektrum.

In hoofdstuk 2 wordt de werking gedemonstreerd van de tamelijk komplexe ionenoptiek, door gebruik te maken van een komputermodel van de dubbeltraps MS. Met name wordt hier aandacht besteed aan de invloed van de vier quadrupolen op de kromming van het beeldvlak, en de positionering ervan ten opzichte van de vlakke CEMA detektor. Aandacht wordt ook besteed aan het mathematische model zelf, dat bestaat uit een eerste orde benadering van de ionenoptiek gebruikmakend van een matrix-representatie. Een vergelijking wordt gemaakt tussen berekende en experimentele quadrupoolinstellingen. Beide instellingen komen opmerkelijk goed met elkaar overeen. De berekende instellingen zouden direkt gebruikt kunnen worden voor een automatische afregeling van de tweede trap van het instrument, zonder een significante piekverbreding in de BGD-spektra te veroorzaken.

In hoofdstuk 3 worden twee methoden beschreven voor het berekenen van massaschalen voor de fragmentenspektra. Bij de zgn. "polynoom methode" geeft een 5^{e}-graads polynoom het funktionele verband tussen de positie van een massapiek op de detektor en de relatieve impuls van de betreffende fragmentionen. Deze methode kan alleen gebruikt worden bij onveranderde dispersie. De andere massakalibratiemethode kan ook gebruikt worden bij veranderde dispersie. Deze methode gebruikt de matrix beschrijving van de ionenoptiek van de dubbeltraps MS, die beschreven is in hoofdstuk 2. Met beide methoden kan een nominale massatoewijzing verkregen worden tot m/z 1000. In dit hoofdstuk wordt verder nog aandacht besteed aan piekverschuivingen in BGD-spektra, als gevolg van de vermindering van de translatie energie van het prekursorion bij het botsingsproces.

In konventionele instrumenten voor BGD-MS kan daardoor een foutieve massatoewijzing van een piek optreden. Door toepassing van naversnelling en een magneet als analysator van de fragmenten is dit effekt bij de dubbeltraps verwaarloosbaar klein.

Hoofdstuk 4 behandelt het komplete simultane, elektro-optische ionen-detektiesysteem. Dit bestaat uit twee chevron kanaalplaten (CEMA), een fiberoptiekplaat waarop een fosforlaag is

aangebracht, een kamera objektief en een 1024-kanaals fotodiode array. Voor de verwerking van de meetresultaten is een uitgebreid informatiesysteem aan de detektor gekoppeld. De belangrijkste bewerkingen op de spektra zijn: aftrekken van de door de detektor gegenereerde achtergrond en korrigeren voor spatiële gevoeligheidsvariaties van de detektor.

Achtergrondsignaal van CEMA en fotodiode array zijn experimenteel bepaald. De gemiddelde detektor respons op een ion is ongeveer 200 counts (1 count = 1000 elektronen uit de optische detektor). De CEMA-ruis is gemiddeld ca 1 "donkerion" per massapiek en per 250 s. De ruis van de optische detektor is evenredig met de wortel uit de meettijd en wordt tevens bepaald door de arraytemperatuur. Nadat de achtergrond afgetrokken is en bij een arraytemperatuur van $-20,5^{o}C$ is de geïntegreerde ruis van het optische gedeelte slechts 46 counts per massapiek, na 250 s meettijd. De maximale dynamiek in piekhoogten van een simultaan gemeten spektrum is $3,3 \times 10^{4}$ bij een signaal-ruisverhouding van 1, en wordt momenteel beperkt door de kapaciteit van het lokale accumulatiegeheugen. Door het toepassen van een gevoeligheidskorrektie kan de reproduceerbaarheid bij het meten van piekoppervlakken met een faktor 4 verbeterd worden tot waarden beter dan 20%.

Hoofdstuk 5 wordt gewijd aan een biochemische en aan een organisch-chemische toepassing van het instrument. Als biochemische toepassing wordt massa 59 uit het pyrolyse massaspektrum van gehele myco-bakteriën geïdentificeerd. Deze massa 59 behoort tot een groep van pieken, op grond waarvan men de voor de mens gevaarlijke tuberculose bakteriën kan onderscheiden van ongevaarlijke soortgenoten. Door m/z 59 te identificeren als acetamide, is nu ook bekend dat één van de verschillen tussen deze bakteriesoorten bepaald wordt door N-acetylaminosuikerkomponenten, die in de celwand voorkomen. Bij de organisch-chemische toepassing wordt het pyrolysefragmentatieproces van alleencarbonzuur onderzocht. Massa 40 uit het pyrolyse-massaspektrum van deze stof wordt geïdentificeerd als propyn, waarbij het duidelijk onderscheiden kan worden van de alternatieve isomere modelstof alleen, op grond van de BGD-spektra.

S T E L L I N G E N

bij het proefschrift

An ultra-sensitive instrument for collision activated dissociation mass spectrometry with high mass resolution

door

G.J. Louter

Amsterdam, 23 februari 1982

I

In de dubbeltrapsmassaspektrometer kan, met behoud van dezelfde massaresolutie, een grotere detektie-efficiency bereikt worden door toepassing van een twee-dimensionaal optisch detektiesysteem.

II

De afleiding door P.J. Todd van de waarschijnlijkheid van meervoudige botsingen is onjuist.

P.J. Todd and F.W. McLafferty, Int.J.Mass Spectrom. Ion Phys. 38 (1981) 371
P.J. Todd, Thesis, Cornell University, Ithaca, N.Y., 1980, pg. 111-115

III

Voor massaspektrometrische struktuuranalyse van niet gederivatiseerde oligosacchariden kan beter gebruik gemaakt worden van Fast Atom Bombardment (FAB) dan van Field Desorption (FD).

IV

Een hogere energie van het prekursorion hoeft niet noodzakelijkerwijs een vermindering van de relatieve energiespreiding, en daardoor een toename van de massaresolutie van het fragmentionenspektrum tot gevolg te hebben.

F.W. McLafferty, P.J. Todd, D.C. McGilvery, M.A. Baldwin, F.M. Bockhoff, G.J. Wendel, M.R. Wixom and T.E. Niemi, in A. Quale (Ed.), Advances in Mass Spectrometry, Vol. 8, Elsevier, Amsterdam, 1979, pg. 1592, regel 19 v.o.

V

In zijn berekeningen aan het elektrische veld in een toroïdale elektrostatische analysator maakt H. Moestue ten onrechte gebruik van een symmetrie van het elektrische veld.

H. Moestue, Rev.Sci.Instrum. 44 (1973) 1709

VI

Het gebruik van gestandaardiseerde faktorscores in diskriminant-analyse verdient de voorkeur boven het gebruik van de originele variabelen.

M.M. Tatsuoka, Multivariate Analysis, Wiley, N.Y., 1971, pg. 157-164

VII

In konventionele gescande massaspektrometers kan de donker-ionenstroom per massapiek principieel verkleind worden door toepassing van een detektiesysteem dat gebaseerd is op een channelplate.

VIII

De milieureguleringen in de ontwikkelde landen hebben geleid tot een verplaatsing van milieuvervuilende aktiviteiten naar ontwikkelingslanden.

IX

Door meer deeltijdwerk in alle soorten funkties te kreëren, zouden overheid en bedrijfsleven kunnen voldoen aan de behoefte van vele jonge en toekomstige ouders om naast verantwoording voor hun baan beiden ook zorg en verantwoording te dragen voor de opvoeding van hun kinderen en voor de huishoudelijke arbeid.